LINKING LAST GLACIAL MAXIMUM OXYGEN AND PREFORMED PHOSPHATE TO ATMOSPHERIC CO_2 DRAWDOWN AND OCEAN CIRCULATION

A Dissertation
Presented to
The Academic Faculty

by

Tyler Vollmer

In Partial Fulfillment
of the Requirements for the Degree
Doctor of Philosophy in
Ocean Science and Engineering

Georgia Institute of Technology
December 2023

LINKING LAST GLACIAL MAXIMUM OXYGEN AND PREFORMED PHOSPHATE TO ATMOSPHERIC CO_2 DRAWDOWN AND OCEAN CIRCULATION

Approved by:

Dr. Jean Lynch-Stieglitz, Advisor
School of Earth and Atmospheric Sciences
Georgia Institute of Technology

Dr. Takamitsu Ito
School of Earth and Atmospheric Sciences
Georgia Institute of Technology

Dr. Kevin Haas
School of Civil and Environmental Engineering
Georgia Institute of Technology

Dr. Joseph Montoya
School of Biological Sciences
Georgia Institute of Technology

Dr. Christopher Reinhard
School of Earth and Atmospheric Sciences
Georgia Institute of Technology

Date Approved: November 9th, 2023

ACKNOWLEDGEMENTS

I want to first thank my advisor, Jean Lynch-Stieglitz, for all her invaluable support and guidance throughout my doctoral journey. Her expertise, unwavering commitment, and insightful feedback have been instrumental in shaping the trajectory of not only my research but also me as an academic and scientist. I could not have asked for a better advisor that has supported me through all my endeavors, whether that be my academic or personal goals. I would also like to thank my committee members: Takamitsu Ito, Christopher Reinhard, Joseph Montoya, and Kevin Haas for being so supportive through this process and for helping to see the bigger picture. I'd also like to express my heartfelt gratitude to our old lab manager Tammy Chang. Her unwavering support and genuine care made this doctoral journey possible.

I also want to thank all my friends I have made through this journey. Thank you to Team Paleo, past and new: Karim Lakhani, Grace Kim, Shannon Valley, Minda Monteaguedo, Hussein Sayani, Shelby Ellis, Annika Jersild, Amanda Timmerman, Bora Buyurgan, Gillian Patterson, Isaac Sipp-Alpers, Will Stevens, Candice Chen, Autumn Toms, and Emelia Deino. I'd also like to thank all the coaches and ice skaters at the Ice Forum who have been extremely supportive of both my academic and skating career.

Lastly, I am deeply grateful to express my heartfelt thanks to my parents for their unwavering support and encouragement throughout my Ph.D. journey. Their love and support have been the bedrock of my success, and I owe much of my academic achievements to their selfless dedication and belief in my potential.

TABLE OF CONTENTS

ACKNOWLEDGEMENTS **iii**

TABLE OF CONTENTS **iv**

LIST OF TABLES **vi**

LIST OF FIGURES **viii**

LIST OF SYMBOLS AND ABBREVIATIONS **xii**

SUMMARY **xv**

CHAPTER 1. Proxy-based preformed phosphate estimates point to increased biological pump efficiency as primary cause of last glacial maximum CO_2 drawdown **1**
1.1 Introduction **1**
1.2 Methods **8**
1.2.1 Reconstruction of Preformed Phosphate 8
1.2.2 Reconstruction of Preformed $\delta^{13}C$ 15
1.2.3 Numerical Sensitivity Experiments 15
1.3 Results and Discussions **20**
1.3.1 Glacial-Interglacial Changes in O_2 20
1.3.2 Glacial-Interglacial Changes in Preformed PO_4 22
1.3.3 Glacial-Interglacial Changes in Preformed $\delta^{13}C$ 27
1.3.4 Mechanisms for Changes in Oxygen and Preformed PO_4 29
1.3.5 Using $P_{pre,AOU}$ versus P_{pre} to determine Atmopsheric pCO_2 drawdown 37
1.3.6 Quantifying LGM CO_2 drawdown from $P_{pre,AOU}$ and $\delta^{13}C_{pre,AOU}$ 42
1.4 Conclusions **47**

CHAPTER 2. Decrease of Deep ocean oxygen and phosphate in the South Pacific during the last Glacial Maximum **48**
2.1 Introduction **48**
2.1.1 Oceanographic Setting and Core Locations 54
2.2 Methods **57**
2.2.1 Updated $\Delta\delta^{13}C$ – Paleo oxygen Calibration 57
2.2.2 Reconstruction of Bottom Water Oxygen 59
2.2.3 Reconstruction of Bottom Water Phosphate 60
2.2.4 Reconstruction of Bottom Water Preformed Phosphate 60
2.3 Results and Discussion **61**
2.3.1 Updated $\Delta\delta^{13}C$ – Paleo oxygen Calibration 61
2.3.2 Glacial-Interglacial Changes in Oxygenation 64
2.3.3 Glacial-Interglacial Changes in Preformed Phosphate and Implications to Atmospheric CO_2 drawdown 68
2.3.4 Implications for South Pacific Circulation and Productivity during the LGM 69
2.3.5 Implications for Global Deep Ocean Circulation during the LGM 73
2.4 Conclusions **76**

CHAPTER 3. Changes in the southeast atlantic oxygen minimum zone during the Last Glacial Maximum **77**
3.1 Introduction **77**
3.2 Material and Methods **80**
3.2.1 Foraminiferal Carbon Isotope Data 80
3.2.2 Reconstruction of Bottom-Water Oxygen 81
3.3 Results and Discussion **81**
3.3.1 Glacial-Interglacial Changes in the Southeast Atlantic 82
3.3.2 Potential Mechanisms for the Shift in the OMZ 88
3.4 Conclusions **89**

CHAPTER 4. Suggestion on future work **91**

APPENDIX A. Supplementary Information to "Proxy-based preformed phosphate estimates point to increased biological pump efficiency as primary cause of last glacial maximum CO_2 drawdown **94**
A.1 Introduction **94**
A.2 Core Data Summary **94**
A.3 Calculation of $P_{pre,AOU}$, Preformed $\delta 13Cpre$, AOU Error, and pCO_2 Drawdown Error **99**

APPENDIX B. Supplementary information to "Decreased of deep ocean oxygen and phosphate in the South Pacific during the Last Glacial Maximum" **101**

APPENDIX C. Supplementary information to "Last Glacial Maximum Changes in the southeast atlantic oxygen minimum zone" **111**

REFERENCES **117**

LIST OF TABLES

Table 1 - Modern, Holocene, and LGM Bottom-Water O2 and $P_{pre,AOU}$. 1-σ errors are shown. 10

Table 2 - The expected drawdown of CO2 for several processes during the LGM... 43

Table 3 - Carbon reservoir changes for a variety of perturbations of the MITgcm: (1) control, (2) increased biological activity, (3) decreased wind stress, (4) increased stratification, (5) combining 2, 3, and 4, and (6) 5.6 degree northward increase of of Southern Ocean sea-ice extent. Following the methodology in (Ferreira et al., 2018) and (Ito & Follows, 2013), we determined the individual effects of on the carbon reservoir due to changes in solubility (temperature and salinity dependence), biological pump (organic), carbonate pump, and the residual disequilibrium term.. 46

Table 4 - Summary of oxygen reconstructions for the LGM and late Holocene for V29-140, V19-258, and V19-259....... 86

Table 5 - Summary of *Globobulimina spp.* data used for the updated $\Delta\delta^{13}C$ – O_2 paleo-oxygen proxy. 101

Table 6 - Summary of *C. wuellerstorfi* or P. ariminensis data used for the updated Δδ13C – O_2 paleo-oxygen proxy ... 102

Table 7 - Summary of data for the updated $\Delta\delta^{13}C$ – O_2 paleo-oxygen proxy. $\Delta\delta^{13}C$ is the difference in $\delta^{13}C$ between *Globobulimina spp.* (Table 5) and *C. wuellerstorfi/P. ariminensis* (Table 6).. 105

Table 8 - Summary of oxygen reconstruction in the South Indo-Pacific. "H" represent late Holocene. "LGM" represents the Last Glacial Maximum. "n" represents the number of specimens for a given Holocene or LGM estimate. "delta_d13C" represents $\Delta\delta 13C$. Modern O_2 estimates are from WOA13. 106

Table 9 - Summary of LGM preformed phosphate reconstructions in EEP and South Indo-Pacific. "O2_recon" are the LGM oxygen reconstructions. "Temp" is temperature estimates from WOA13 subtracted by 2.5 deg C to address a plausible decrease in temperature for the LGM (Bereiter et al., 2018). "Sal" is salinity estimates from WOA13 added by 1 g/kg to address plausible increase in salinity for the LGM (Adkins, 2002). "O2,sat" is the oxygen saturation determined from the temperature and salinity estimates. "Cd_sw" is the Cadmium of seawater estimates from their respective sources. "P" is the phosphate estimate from the "Cd_sw". "P_pre_AOU" is the preformed phosphate estimate. "err" represents the variables respective 1-sigma error. 108

Table 10 - Summary of oxygen reconstruction for V29-140. 111

Table 11 - Summary of oxygen reconstruction for V19-258.. 113

Table 12 -Summary of oxygen reconstruction for V19-259. 115

LIST OF FIGURES

Figure 1 - Seawater Cd reconstructed from foraminifera using a depth-dependent (blue) and depth- independent H. elegans (red) empirical distribution coefficient versus bottom water phosphorous. Data are from Boyle, 1988, 1992; Boyle et al., 1995. The fit follows the Rayleigh model in Elderfield and Rickaby, 2000 (equation 2).............. 8

Figure 2 - Modern oceanographic climatology from World Ocean Atlas 2013 (WOA13) of surface ocean $P_{pre,AOU,}$ with the eight pink stars representing the locations of $P_{pre,AOU}$ reconstructions... 12

Figure 3 - Bottom-water O_2 versus $\Delta\delta^{13}C$ calibration using data from Hoogakker et al., 2015. $\Delta\delta^{13}C$ is the difference between epifaunal *C. wuellerstorfi* or modern bottom-water $\delta^{13}C$ and infaunal *G. affinis*. Core sites using pore-water data were excluded. The linear fit for $O_2 < 235$ µmol/kg is shown in equation 3. The RMSE of this fit is 14.2 µmol/kg.. 14

Figure 4 - Local bottom water $P_{pre,AOU}$ versus the global mean $P_{pre,AOU}$ for a variety of perturbations of the MITgcm at the 2730 meter Eastern Equatorial Pacific and 1803 m Arabian Sea core sites.. 19

Figure 5 - (top) Bottom water oxygen and (bottom) preformed phosphate reconstructions at eight locations. The modern oceanographic climatology (current) is from World Ocean Atlas 2013 (WOA13). Late Holocene is defined as 0 – 6 ka. LGM is defined as 19 – 23 ka. 1-σ errors are shown. 21

Figure 6 - Observed O_2 (µmol/kg) based on World Ocean Atlas (WOA13) for the zonally averaged transects of the Atlantic Ocean (a) and Pacific and Indian Ocean (b). Simulated O_2 from the control run for the Atlantic Ocean (c) and Pacific and Indian Ocean (d). Determined $P_{pre,AOU}$ (µmol/kg) based on World Ocean Atlas (WOA13) for the zonally averaged transects of the Atlantic Ocean (e) and Pacific and Indian Ocean (f). Simulated $P_{pre,AOU}$ for the Atlantic Ocean (g) and Pacific and Indian Ocean (h). 23

Figure 7 - Preformed $\delta^{13}C_{pre.AOU}$ reconstructions for 8 core locations for the Late Holocene and LGM........................... 28

Figure 8 - $P_{pre,AOU}$ versus $\delta^{13}C_{pre,AOU}$ plot at each of the eight core-sites. A linear fit is performed through six of the seven core-sites. The RMSE of this fit is 0.17, with an R2 correlation of 0.78. Core site ODP-1242 and GeoB3606-1 is relatively shallow and would be influenced from other intermediate waters.. 29

Figure 9 - Simulated oxygen (µmol/kg) anomalies with respect to the control run for (a,b) increased stratification, (c,d) increased biological productivity, and (e,f) weakened Southern Ocean for the Atlantic Ocean (a, c, e, f) and Pacific

and Indian Ocean (b, d, f, g). The circle's location and color indicate reconstructed bottom water O_2 from 19 – 23 ka. 32

Figure 10 - Simulated $P_{pre,AOU}$ (μmol/kg) anomalies with respect to the control run for (a,b) increased stratification, (c,d) increased biological productivity, and (e,f) weakened Southern Ocean for the Atlantic Ocean (a, c, e, f) and Pacific and Indian Ocean (b, d, f, g). The circle's location and color indicate reconstructed $P_{pre,AOU}$ from 19 – 23 ka......... 33

Figure 11 - Bottom water (top-left) oxygen and (top-right) preformed phosphate at each core location for the LGM proxy and numerical sensitivity experiments: increase stratification, increase biological activity, and decrease surface wind stress. Changes in bottom-water oxygen (bottom-left) and preformed phosphate (bottom-right) for the experiments (Perturbation – Control) and data (LGM – Modern) at each core location. 1-σ errors are shown. 34

Figure 12 - Global Meridional Overturning Circulation (MOC) stream function measured in Sverdrups (Sv) for the control run (top), the decreased surface wind stress simulation-control difference (middle), the increased stratification simulation-control difference (bottom). 35

Figure 13 - The solid black line is the theoretical relationship between changes in true preformed phosphate and atmospheric pCO_2 (121 ppm/μM). Squares are the changes in atmospheric CO_2 due to changes in the biological pump efficiency with respect to the respective model's change in globally average true P_{pre} (perturbation-control), excluding the ice simulations. The diamonds represent the increase Southern Ocean sea-ice extent simulations. 39

Figure 14 - Changes in the globally-averaged $P_{pre,AOU}$ and globally-averaged true P_{pre} for each of the 5 ice simulations plus control run. The control run is represented as a 0 deg increase in Southern Ocean sea-ice extent. There are 5 ice simulations: 2.8 degree increase, 5.6 degree increase, 8.4 degree increase, 11.2 degree increase, and 14 degree increase in Southern Ocean sea-ice latitudinal extent with respect to modern. 40

Figure 15 - Location of the 31 cores for the updated $\Delta\delta^{13}C$ – O2 calibration. 17 cores shown in pink are from this study. 14 cores shown in green are from previously published results. See Table 5 for more information. 55

Figure 16 - Relationship between $\Delta\delta^{13}C$ (the difference in $\delta^{13}C$ between *C. wuellerstorfi/P. ariminensis* and *Globobulimina spp.*) and bottom-water oxygen estimated from WOA13 (Boyer et al., 2013). The study includes previously published data, shown in green, Hoogakker et al., 2015, 2018; Jacobel et al., 2020; Lu et al., 2023;

Mackensen & Licari, 2003; McKay et al., 2016; Schmiedl & Mackensen, 2006; Umling et al., 2018. New data from this study is shown in green. Results are summarized in Table 5. 61

Figure 17 - Phosphate (left), oxygen (middle), and preformed phosphate (right) reconstructions for the south Indo-Pacific (top) and Eastern Equatorial Pacific (bottom) (cores summarized in Table 6, Table 7, and Table 8). The preformed phosphate estimates for the eastern equatorial pacific cores use an interpolation of the oxygen reconstructions at that depth. The LGM reconstructions are shown in blue. The late Holocene reconstructions are shown in red. The modern climatology from WOA13 is shown in black (Boyer et al., 2013). 64

Figure 18 - Relationship between Apparent Oxygen Utilization (AOU) and Phosphate (P) for the deep south Indo-Pacific, the deep Arabian Sea, and the Deep Eastern Equatorial Pacific (EEP). AOU and P reconstructions for the deep south Indo-Pacific and deep EEP are from an average of cores >2000 meters from this study. AOU and P reconstructions (cores > 2000 meters) for the deep Arabian Sea are from Boyle, 1992; Lu et al., 2023. Error bars are the 1-sigma calibration error for both AOU and P. LGM reconstructions are shown in blue. Modern estimates from WOA13 are shown in red (Boyer et al., 2013). The Redfield ratio between Oxygen and Phosphate of 170:1 is shown in gray. 71

Figure 19 - Relationship between Apparent Oxygen Utilization (AOU) and Phosphate (P). AOU and P reconstructions for the deep south Indo-Pacific and deep EEP are from an average of cores >2000 meters from this study. AOU and P reconstructions for the deep Arabian Sea, deep S. Atlantic, deep N. Atlantic, and shallow N. Atlantic are from Boyle, 1992; Boyle et al., 1995; Gottschalk et al., 2016; Gottschalk et al., 2016; Hoogakker et al., 2015, 2018; Lu et al., 2023; Marchitto & Broecker, 2006; Martin et al., 2005; McKay et al., 2016; Mojtahid et al., 2017; Roberts et al., 2016; Rosenthal et al., 1997; Schmiedl & Mackensen, 2006; Skinner et al., 2003; Umling et al., 2018. AOU and P error bars are the 1-sigma calibration error for both AOU and P. LGM reconstructions are shown in blue. Modern estimates from WOA13 are shown in red (Boyer et al., 2013). The Redfield ratio between Oxygen and Phosphate of 170:1 is shown in gray. Dash lines represent the phosphate levels if AOU was reduced to 0 and followed the Redfield ratio from the deep south Indo-Pacific core. 75

Figure 20 - Location of core-sites. V29-140 is labeled as 1. V19-258 is labeled as 2. V19-258 is labeled as 3. 83

Figure 21 - (left) $\delta^{13}C$ record of *C. wuellerstorfi* and *Globobulimina spp*. for each core. (right) Oxygen reconstruction for each core using the updated calibration from equation 7. Red represents late Holocene time slice. Blue

represents LGM time slice. The yellow star represents modern oxygenation based on World Ocean Atlas 2013 (Boyer et al. 2013). 84

Figure 22 - Late Holocene and LGM oxygen reconstructions for V29-140, V19-258, V19-259. The LGM oxygen reconstructions for each core-site are shown at a depth 120 meters less than the modern depth due to lower sea level during the LGM (Clark & Mix, 2002). The errors shown are the RMSE from the calibration. 86

LIST OF SYMBOLS AND ABBREVIATIONS

LGM	Last Glacial Maximum
ka	thousand calendar years ago
AOU	Apparent Oxygen Utilization
$P_{pre,AOU}$	preformed phosphate estimate based on AOU
$\delta^{13}C_{pre,AOU}$	preformed $\delta^{13}C$ estimate based on AOU
$\delta^{13}C$	Ratio of carbon-13 to carbon-12 relative to a standard
$\Delta\delta^{13}C$	Difference between $\delta^{13}C$ of epifaunal benthic foraminifera *C. wuellerstorfi/P. ariminensis* and infaunal benthic foraminfiera *Globobulimina spp.*
OMZ	Oxygen Minimum Zone
ppm	parts per million
DIC	Dissolved inorganic Carbon
$PO_{4,pre}/P_{pre}$	preformed phosphate
P_{reg}	Regenerated phosphate
P	Total phosphate
$O_{2,sat}$	Oxygen Saturation
$\delta^{15}N$	Ratio of nitrogen-15 to nitrogen 14 relative to a standard
Cd	Cadmium
Ca	Calcium
Mg	Magnesium
H. elegans	*Hoeglundina Elegans*
$P_{reg,AOU}$	Regnerated phosphate estimates using AOU
T	Temperature
S	Salinity
WOA13	World Ocean Atlas 2013

Cd_w or Cd_{sw}	Cadmium of seawater
Cd_t	total cadmium
O_2^{bot}	bottom-water oxygen
RMSE	Root mean squared error
$\delta^{13}C_{reg}$	regenerated $\delta^{13}C$
$\delta^{13}C_{pre}$	preformed $\delta^{13}C$
$\delta^{13}C_{pre,AOU}$	preformed $\delta^{13}C$ determined using AOU
$\delta^{13}C_{reg,AOU}$	regenerated $\delta^{13}C$ determined using AOU
MITgcm	Massachusetts Institute of Technology general circulation model
$O_{2,pre}$	preformed oxygen
PSU	Practical Salinity Unit
S	Salinity
C. wuellerstorfi	*Cibicoides wuellerstorfi*
G. affinis	*Globobulimina affinis*
C. kullenbergi	*Cibicoides kullenbergi*
AAIW	Antartic Intermediate Water
GNAIW	Glacial North Atlantic Intermediate Water
SAZ	Subantarctic Zone
NADW	North Atlantic Deep Water
pCO_2	partial pressure of CO_2
I/Ca	Ratio between Iodine and Calcium in foraminifera
BWO	Bottom water oxygen
aU	Authigenic Uranium

SAMW	Subantartic Mode Waters
CDW	Circumpolar Deep Waters
EEP	Eastern Equatorial Pacific
Cd/Ca	Ratio between Cadmium and Calcium in foraminifera
$^{231}Pa/^{230}Th$	Ratio between Protactinium mass 231 and Thorium mass 230
S.O.	Southern Ocean
AABW	Antartic Bottom Water
OMZ	Oxygen Minimum Zone
PDB	Pee Dee Belemite

SUMMARY

The ocean's biological pump plays a notable role in regulating CO_2 levels and climate. During the Last Glacial Maximum (LGM), a period 23 ka – 19 ka, atmospheric CO_2 was significantly lower than the pre-industrial, potentially due to an increase in the biological pump efficiency. Oxygen and preformed phosphate reconstructions can provide insight to changes in the biological pump efficiency.

In Chapter 1, I quantified preformed phosphate ($P_{pre,AOU}$) and preformed $\delta^{13}C$ ($\delta^{13}C_{pre,AOU}$) of LGM bottom waters using a compilation of published paleo-temperature, nutrient, and oxygen estimates from benthic foraminifera. Our results show that preformed phosphate of the Pacific and Indian deep oceans was significantly reduced and suggest that much of the Glacial-Interglacial CO_2 drawdown resulted from changes in the ocean's biological pump efficiency. Preformed $\delta^{13}C$ show similar results. The reconstructed LGM $P_{pre,AOU}$ and oxygen are qualitatively consistent with the changes produced by a suite of numerical sensitivity experiments that roughly simulate three proposed mechanisms for an increase in LGM biological pump efficiency: an increase in biological activity, a decrease in wind-driven upwelling, and an increase in stratification in the Southern Ocean.

In Chapter 2, I present a combination of paleo-oxygen estimates derived from the difference in $\delta^{13}C$ of two species of benthic foraminifera, along with previously published paleo-nutrient estimates obtained through Cd/Ca measurements of benthic foraminifera in both the South Indo-Pacific and Eastern Equatorial Pacific regions. Our results show a parallel reduction in deep ocean oxygen and phosphate levels at both sites, indicating an increase of respired carbon in the deep Pacific and a decrease in preformed phosphate.

However, the oxygen and phosphate gradient between these two sites remained unchanged during the LGM compared to modern, suggesting no significant alterations in deep ocean circulation or productivity in the South Pacific. This insight supports the notion that the Southern Ocean played a central role in Atmospheric CO_2 drawdown through increase nutrient utilization, leading to the observed decrease in oxygen and phosphate in the deep South Indo-Pacific and Eastern Equatorial Pacific. Additionally, we expanded the $\Delta\delta^{13}C$ paleo-oxygen proxy calibration to 31 cores.

In Chapter 3, I reconstructed oxygen at three depths within or near the Benguela Upwelling System in the southeast Atlantic using the updated $\Delta\delta^{13}C$ paleo-oxygen proxy calibration from chapter 2. Our results provide evidence of a deepening of the Oxygen Minimum Zone (OMZ) during the LGM. This is marked by a significant increase in oxygen levels at the shallowest core site, juxtaposed with a significant reduction oxygenation level noted at the deeper site. The notable rise in oxygen levels at the shallowest site cannot be solely attributed to higher oxygen saturation or increased productivity, indicating a shift in ocean circulation and/or the OMZ structure is required.

In Chapter 4, I conclude with a discussion on what questions remain on reconstructing oxygen, preformed phosphate, and preformed $\delta^{13}C$.

CHAPTER 1. PROXY-BASED PREFORMED PHOSPHATE ESTIMATES POINT TO INCREASED BIOLOGICAL PUMP EFFICIENCY AS PRIMARY CAUSE OF LAST GLACIAL MAXIMUM CO_2 DRAWDOWN

(Previously published as: Vollmer, T.D., Ito, T., and Lynch-Stieglitz, J. (2022) Proxy-Based Preformed Phosphate Estimates Point to Increased Biological Pump Efficiency as Primary Cause of Last Glacial Maximum CO_2 Drawdown. Paleoceanography and Paleoclimatology, 37, 11, DOI: https://doi.org/10.1029/2021PA004339)

1.1 Introduction

In the last 2.5 million years, the Earth's climate has been characterized by the quasi-periodic growth and decay of continental ice sheets. These glacial-interglacial cycles are driven by changes in the distribution of solar insolation, modulated at several dominant frequencies associated with the oscillations of the Earth's orbital parameters. Mechanisms linking the orbital parameters to the glacial climate must involve a nonlinear response and positive feedbacks that amplified the orbital forcing. One of the major mechanisms that amplified the orbital forcing is the CO_2 feedback. Polar ice core records have revealed a coupling between the late Pleistocene glaciation and atmospheric carbon dioxide changes of O(100) ppm (EPICA community members, 2004; Petit et al., 1999). This paper aims to better quantify and understand the causes of the lower atmospheric CO_2.

There have been a variety of mechanisms put forth that may contribute to the glacial drawdown of atmospheric carbon dioxide, including changes in: the ocean's solubility pump, the ocean's biological pump, the terrestrial carbon inventory, the ocean's air-sea disequilibrium, and the carbonate compensation mechanism (Khatiwala et al., 2019; Sigman et al., 2010). Previous studies show that changes in the ocean's temperature, salinity, and the terrestrial carbon inventory contribute a minor opposing role in the glacial drawdown of CO_2 (Sigman et al., 2010; Sigman & Boyle, 2000). The expected cooler ocean temperatures during the LGM led to higher concentrations of dissolved CO_2 in the glacial ocean, contributing to a drawdown of atmospheric CO_2. Counteracting this, more saline waters led to lower concentrations of dissolved CO_2 in the glacial ocean, contributing to a release of CO_2 to the atmosphere. However, these combined effects are minor compared to the overall drawdown we see from ice core records. Additionally, previous studies suggest lower forest coverage during glacial periods, corresponding to a release of CO_2 to the atmosphere. However, estimates on how much of a release are highly uncertain (Ciais et al., 2012; Peterson et al., 2014; Sigman & Boyle, 2000). Overall, this suggests that changes in the ocean's biological pump efficiency and the attendant changes in air-sea exchange of carbon in deep water formation regions (hereafter jointly referred to as "biological pump efficiency"), along with the carbonate compensation mechanism, are potential leading causes for the drawdown of atmospheric CO_2 during the LGM.

The biological pump is the process by which production of organic matter in the surface ocean and remineralization of sinking organic matter at depth sequesters carbon in the deep ocean. The efficiency of the biological pump depends not only on the downward flux of organic carbon but also on the retention of remineralized carbon in the deep ocean. Volk & Hoffert (1985) first defined the metric for the biological pump as the vertical gradient of Dissolved Inorganic Carbon (DIC) as it measures the storage of biologically sequestered carbon in the deep water. Early box model studies also identified the polar surface nutrient concentrations as a key metric for the efficiency of the biological pump (Knox and McElroy 1984, Sarmiento and Toggweiler 1984, Siegenthaler and Wenk 1984) where the equilibrium atmospheric pCO_2 is linearly proportional to the polar surface nutrient concentrations. Polar surface phosphate concentrations are closely related to the preformed phosphate of deep waters, defined as the phosphate concentration when the water was last in contact with the atmosphere. The biological carbon storage and the preformed phosphate inventory are stoichiometrically related. Ito & Follows (2005) and Marinov et al. (2008) showed that the equilibrium atmospheric pCO_2 is proportional to the global preformed phosphate with a predictable relationship as ΔpCO_2^{atm} [ppm] ~ 136 $\Delta PO_{4,pre}$ [µM] where $PO_{4,pre}$ is the change in global mean preformed phosphate. These studies did not include any additional changes due to $CaCO_3$ compensation. Biological carbon storage is also stoichiometrically related to the regenerated phosphate (P_{reg}) and oxygen utilization. However, if it can be determined accurately, preformed phosphate has the advantage of being conservative in the subsurface ocean. This means that if we know the volumetric contributions of deep-water masses, we only need to determine P_{pre} at a limited number of locations.

Phosphate concentration in the subsurface waters can be considered as the sum of the preformed phosphate, (P_{pre}) and the phosphate added by the respiration of organic matter (P_{reg}), $P = P_{pre} + P_{reg}$. In this paper, the efficiency of the biological pump is measured by the global mean preformed phosphate, which can be modulated by a suite of physical and biogeochemical processes. Depletion of polar surface nutrients can lead to a decrease in preformed nutrient and a higher efficiency of the biological pump, which can be driven by increased productivity, increased stratification and/or weakened upwelling of deep waters (Francois et al., 1997; Martínez-García et al., 2014; Robinson et al., 2005; Wang et al., 2017). A change in the relative volume of water masses with different preformed phosphate values can also alter the global mean preformed phosphate, thus changing global biological pump efficiency (Toggweiler et al., 2003).

The regenerated phosphate, P_{reg}, can be estimated from Apparent Oxygen Utilization (AOU) through their stoichiometric relationship. AOU is defined as the difference between the oxygen saturation ($O_{2,sat}$) and the in-situ oxygen where the oxygen saturation is calculated from the local temperature and salinity (Boyer et al., 2013). This approximation, $P_{reg} = R_{P:O_2}AOU$, assumes that the air-sea equilibration of oxygen is relatively rapid and that P_{reg} and AOU are zero at the surface. However, surface water O_2 is typically undersaturated at the time of water mass formation due to heat loss, sea-ice cover, and entrainment of subsurface water. At present, polar oceans are typically undersaturated on the order of 5 – 15% during winter months (Ito et al., 2004). However, the magnitude of oxygen undersaturation due to air-sea disequilibrium is still debated. Using AOU has the potential to overestimate changes in respired carbon by 50% (Khatiwala et al., 2019).

Because we will be reconstructing preformed phosphate using AOU, which may overestimate the magnitude of true oxygen utilization, we call these estimates of preformed phosphate $P_{pre,AOU}$ in order to distinguish this calculation from true preformed phosphate. Consequently, the reconstruction of $P_{pre,AOU}$ incorporates a combination of biological pump contributions and oxygen air-sea disequilibrium. Thus, changes in global preformed phosphate include: (1) changes in the distribution of deep ocean water masses, (2) changes to the surface nutrient content at deep water formation regions, or (3) changes in air-sea disequilibrium in these regions. Consequently, observed changes in $P_{pre,AOU}$ will reflect the contributions of these factors, while the true preformed phosphate (P_{pre}) reflects only (1) and (2). The implication of this difference is discussed in section 1.3.6. If the changes in $P_{pre,AOU}$ are insufficient to fully explain the CO_2 drawdown, that would indicate that other mechanisms must contribute, including changes in whole ocean alkalinity, salinity, or temperature.

Qualitative paleo-oxygen proxies for the ocean, including but not limited to redox-sensitive trace-metals, laminations, foraminiferal assemblages, and $\delta^{15}N$ indicate a decline in oxygen and an increase in oxygen utilization for core sites deeper than 1,500 meters during the LGM (Jaccard et al., 2016; Jaccard & Galbraith, 2012). More recent semi-quantitative proxies, including trace metal I/Ca, the preservation of lipid biomarkers, and pore-analysis on benthic foraminifera also indicate relatively low oxygen during the LGM (Anderson et al., 2019; Lu et al., 2020; Rathburn et al., 2018). I/Ca measurements on foraminifera do not show a correlation with oxygen through all oxygenation levels but do decrease rapidly under poorly oxygenated conditions (< 50 µmol/kg) (Lu, Rickaby, et al., 2020). Increased preservations of lipid biomarkers, such as alkenones, also indicate low oxygenated conditions (20 – 50 µmol/kg) (Anderson et al., 2019). Pore-analysis on benthic foraminifera seems to be another promising indicator of oxygen but has yet been applied to down-core records (Rathburn et al., 2018). Jacobel et al. (2020) identified a reduction of oxygenation in the deep equatorial Pacific during the LGM using a multi-proxy approach incorporating some of these newer semi-quantitative proxies. Here we will take advantage of the fact that quantitative oxygen estimates can be made from carbon isotopes in benthic foraminifera, an approach that was first proposed by McCorkle & Emerson (1988). In this method, the difference in $\delta^{13}C$ between the epifaunal *C. wuellerstorfi* and infaunal *Globobulimina affinis* is used to reconstruct oxygen (Hoogakker et al., 2015).

Here we present the first quantitative reconstruction of $P_{pre,AOU}$ of LGM bottom waters using previously published datasets of sea-floor sediment cores, estimating the contribution of changes in the biological pump efficiency to the lowering of atmospheric CO_2. This requires quantitative estimates of phosphate concentrations, deep-sea temperature, and oxygen. We use the quantitative estimates of oxygen from benthic foraminiferal $\delta^{13}C$. These estimates have only become available recently and exist at a limited number of locations. Deep water Cd strongly covaries with PO_4 , and past PO_4 can be reconstructed from Cd/Ca ratios in foraminifera (Figure 1, Boyle, 1988, 1992; Boyle et al., 1995) . The incorporation of Mg into the calcite shells is temperature dependent and paleotemperature of deep waters can be reconstructed from Mg/Ca in benthic foraminifera (Martin et al., 2005; Roberts et al., 2016; Skinner et al., 2003). The $P_{pre,AOU}$ estimates presented here combine the oxygen reconstructions with PO_4 and temperature estimated from either the same sediment cores or nearby cores (see section 1.2.1). Additionally, we reconstructed preformed $\delta^{13}C$, combining $\delta^{13}C$ with temperature estimated from either the same or nearby cores (see section 1.2.2). It is important to note that the preformed $\delta^{13}C$ estimates do not rely on PO_4, potentially reducing the error in the estimate relative to $P_{pre,AOU}$. But our calculation of preformed $\delta^{13}C$, like that for preformed phosphate, uses AOU to estimate oxygen utilization. Thus, all future references will be called $\delta^{13}C_{pre,AOU}$. Lastly, we performed three-dimensional numerical model experiments to help guide our interpretation of this limited data and to explore mechanistic linkages between the hypothesized perturbations to the biological pump and preformed nutrients.

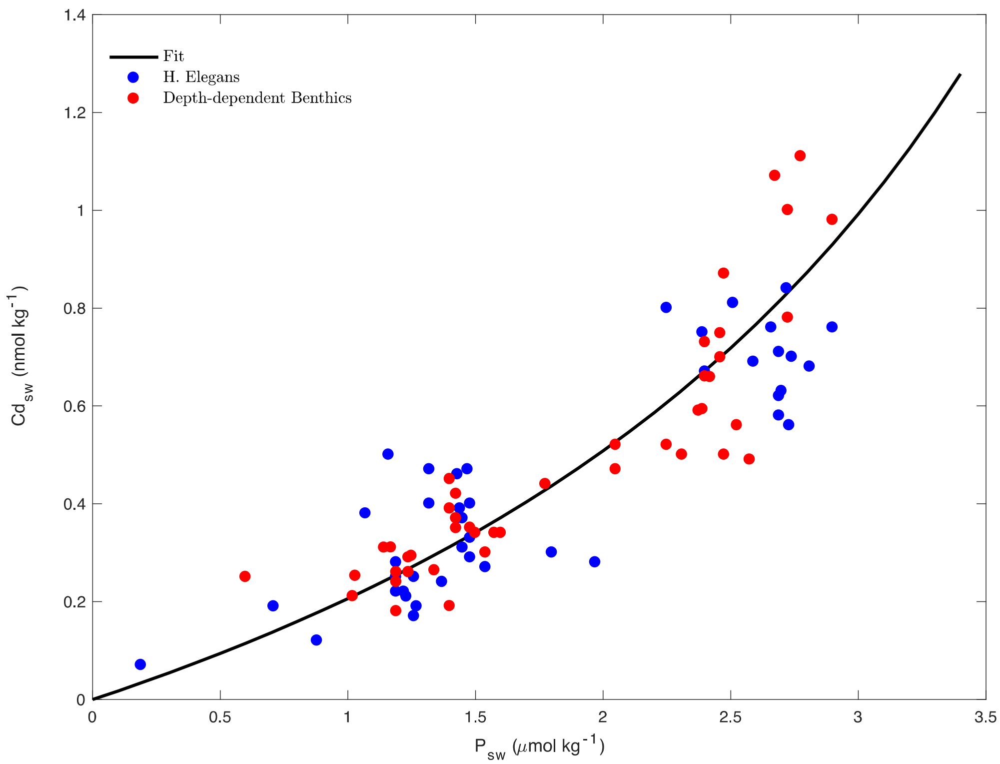

Figure 1 - Seawater Cd reconstructed from foraminifera using a depth-dependent (blue) and depth- independent H. elegans (red) empirical distribution coefficient versus bottom water phosphorous. Data are from Boyle, 1988, 1992; Boyle et al., 1995. The fit follows the Rayleigh model in Elderfield and Rickaby, 2000 (equation 2).

1.2 Methods

1.2.1 Reconstruction of Preformed Phosphate

Observational estimates of preformed phosphate rely on the oxygen deficit relative to saturation, termed as AOU as stated in the previous section. Because surface water O_2 is typically undersaturated at the time of water mass formation due to heat loss, sea-ice cover, and entrainment of subsurfa~~ce~~ waters (Ito et al., 2004), this causes a potential overestimation of respiratory oxygen loss. Since changes in the air-sea disequilibrium on glacial-interglacial timescales are unknown, we defined the notation, $P_{reg,AOU}$, indicating the AOU-based estimate of preformed phosphate and distinguish it from the true P_{reg}. Here we assume a O_2:P stoichiometric ratio of 170±10:1 (Anderson & Sarmiento, 1994). Then it is possible to estimate $P_{pre,AOU}$ as a function of phosphate (P), temperature (T), and oxygen (O_2), all of which can be estimated with existing paleooceangraphic proxies.

$$\mathrm{P_{pre,AOU}} = \mathrm{P} - \frac{1}{170}\left\{\mathrm{O_{2,sat}(S,T)} - \mathrm{O_2}\right\} \qquad (1)$$

Oxygen saturation weakly depends on salinity. Here, we approximate salinity change using the global mean salinity increase of 1 g/kg during the LGM (Adkins, 2002). An increase salinity of 1 g/kg causes a decrease of $O_{2,sat}$ of 2-3 μmol/kg.

Reconstructions of bottom-water $P_{pre,AOU}$ and $\delta^{13}C_{pre,AOU}$ are performed at eight core sites found in the North Atlantic, South Atlantic, the Arabian Sea, and the Eastern Pacific (Figure 2 and Table 1). The number of cores is limited by lack of availability of previously published *Globobulimina spp.* $\delta^{13}C$ required for the O_2 – $\Delta\delta^{13}C$ proxy.

Table 1 - Modern, Holocene, and LGM Bottom-Water O2 and $P_{pre,AOU}$. 1-σ errors are shown.

Core	Location	Lat.	Long.	Depth	Mod. $P_{pre,AOU}$	Hol. $P_{pre,AOU}$	LGM $P_{pre,AOU}$	Hol. $\delta^{13}C_{pre,AOU}$	LGM $\delta^{13}C_{pre,AOU}$	References
		deg N	deg E	meters	µmol/kg	µmol/kg	µmol/kg	‰	‰	
MD99-2328	North Atlantic	48.1	-9.5	942	0.56		0.26 ± 0.36		1.85 ± 0.19	Mojtahid et al. 2017; Marchitto and Broecker 2006
ODP-1242	Eastern Pacific	7.9	-83.6	1364	1.36	1.28 ± 0.34	1.06 ± 0.37	1.87 ± 0.17	1.76 ± 0.23	Hoogakker et al. 2018; Boyle 1992
GeoB3606-1	South Atlantic	-25.5	13.1	1785	0.96	0.55 ± 0.34	0.05 ± 0.38	1.55 ± 0.17	1.85 ± 0.23	Mckay et al. 2016, Marchitto and Broecker 2006
GeoB3004-1	Arabian Sea	14.6	52.9	1803	1.36	1.30 ± 0.34	0.75 ± 0.37	1.65 ± 0.18	1.57 ± 0.22	Schmiedl and Mackensen 2006; Boyle 1995

Table 1 – Continued.

TR163-25T	Eastern Eq. Pacific	-1.7	-88.5	2650	1.43	1.35 ± 0.34	0.88 ± 0.34	1.34 ± 0.18	1.48± 0.18	Umling et al. 2018; Hoogakker et al. 2018; Boyle 1992; Martin et al. 2005
TR163-23	Eastern Eq. Pacific	0.7	-91.9	2730	1.41	1.96 ± 0.34	0.98 ± 0.34	1.16 ± 0.21	1.09 ± 0.17	Umling et al. 2018; Martin et al. 2005
MD95-2042	North Atlantic	33.8	-10.2	3146	0.89		0.82 ± 0.34		1.24 ± 0.19	Hoogakker et al. 2015; Marchitto and Broecker 2006; Skinner et al. 2003; Marchitto et al. 2002

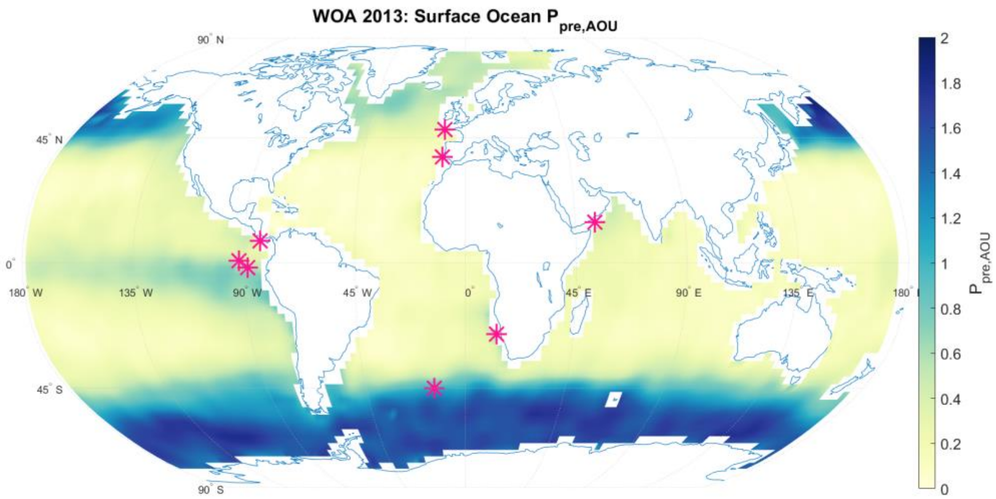

Figure 2 - Modern oceanographic climatology from World Ocean Atlas 2013 (WOA13) of surface ocean $P_{pre,AOU}$, with the eight pink stars representing the locations of $P_{pre,AOU}$ reconstructions.

Here, we briefly summarize how the three variables (P , T and O_2) necessary to calculate $P_{pre,AOU}$ are determined at each location. We reconstruct phosphate concentration (P) using previously published estimates of seawater Cd (Cd_w) based on the Cd/Ca analysis on benthic foraminifera, including but not limited to: *Hoeglundina elegans*, *Uvigerina* spp., *Cibicidoides wuellerstorfi*, *Cibicidoides kullenbergi*, and *Nuttallides umbonifera* (Boyle, 1988; Boyle et al., 1995; Boyle & Keigwin, 1987). We use Cd_w reconstructions either from the core-site itself, from an average of nearby core-sites, or from a simple linear interpolation of the Cd_w data compiled in Marchitto & Broecker (2006), when there were not sufficient nearby core-sites. We calculate P using a nonlinear relationship between Cd_w reconstructed from core top foraminifera and phosphate in the overlying seawater (Figure 1) (Elderfield & Rickaby, 2000). This relationship between Cd and P uses the same functional form as Elderfield & Rickaby (2000), but the coefficients and errors in the regression analysis are determined using core-top Cd_w rather than water column Cd data (Boyle, 1988, 1992; Boyle et al., 1995),

$$P = \frac{P_T}{\left(\frac{Cd_T}{Cd_{sw}} - 1\right)\alpha^{-1} + 1} \quad (2)$$

Cd_T and P_T are constants and are set to 1.2nM and 3.3μM as defined in Elderfield & Rickaby (2000). The fraction factor, $\alpha = 2.2$, is determined based on the best fit to the core top data compilation in Figure 1(Boyle, 1988, 1992; Boyle et al., 1995) .

The bottom water O_2 is reconstructed from the carbon isotope gradient in the sediment column estimated from the difference of $\delta^{13}C$ of foraminifera: epifaunal *C. wuellerstorfi* and infaunal *Globobulimina affinis* (Hoogakker et al., 2015). Sulfate reduction and carbonate dissolution could introduce potential uncertainties in this $\delta^{13}C$ gradient. However, for sites with $[O_2] < 235$ μM, there is a linear relationship between bottom water O_2 and $\Delta\delta^{13}C$. This calibration is based on a limited number of surface sediment samples. We use a linear regression based on the calibration data from Hoogakker et al. (2015), excluding the pore-water data (Figure 3):

$$O_2^{bot}[\mu M] = 124.63 \times \Delta\delta^{13}C + 45.25 \quad (3)$$

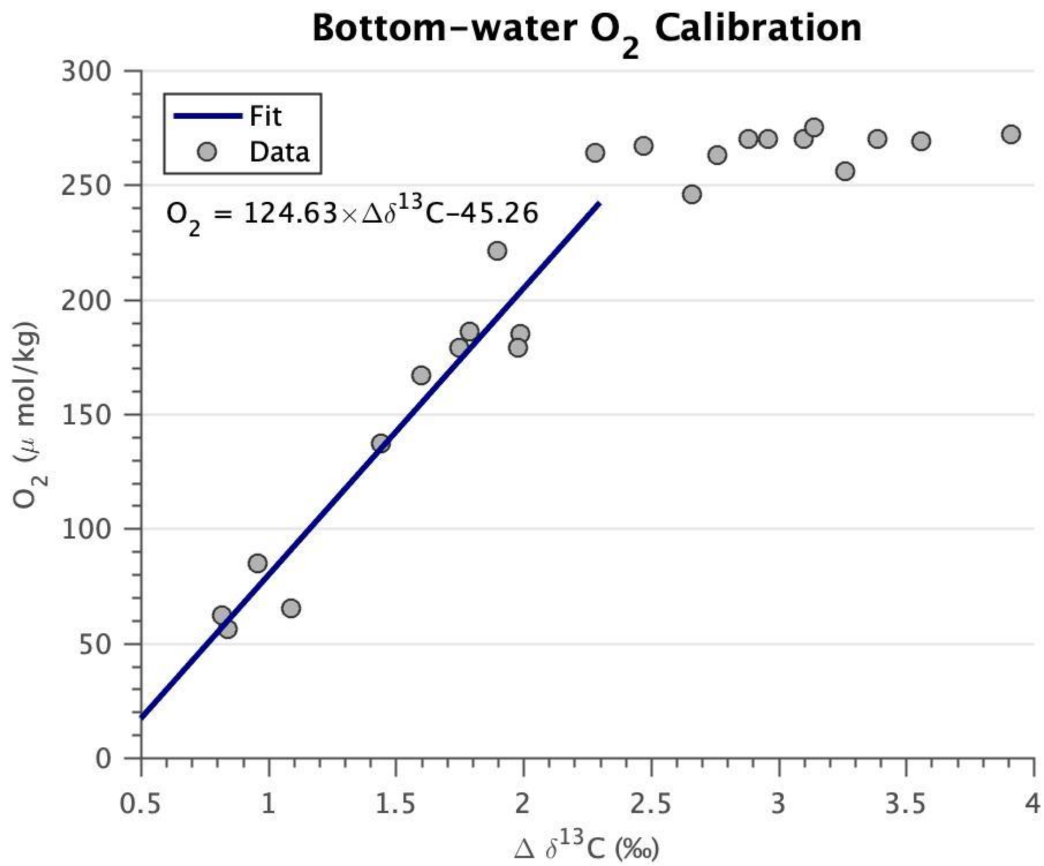

Figure 3 - Bottom-water O_2 versus $\Delta\delta^{13}C$ calibration using data from Hoogakker et al., 2015. $\Delta\delta^{13}C$ is the difference between epifaunal *C. wuellerstorfi* or modern bottom-water $\delta^{13}C$ and infaunal *G. affinis*. Core sites using pore-water data were excluded. The linear fit for O_2 < 235 µmol/kg is shown in equation 3. The RMSE of this fit is 14.2 µmol/kg.

We used the published temperature estimates that were based on Mg/Ca trace metal analyses of benthic foraminifera (i.e. *Uvigerina spp., G. affinis, C. wuellerstorfi*) (Martin et al., 2005; Roberts et al., 2016; Skinner et al., 2003) in the same location as for the O_2 reconstructions and from nearby cores where available. In some cases, there were no nearby temperature reconstructions, and we assign a range of plausible values for the calculations and error estimates.

1.2.2 Reconstruction of Preformed $\delta^{13}C$

Like phosphate, subsurface $\delta^{13}C$ is the surface value at the time of water mass formation (preformed $\delta^{13}C$, $\delta^{13}C_{pre}$) and the change in $\delta^{13}C$ from the original value due to the respiration of organic matter (regenerated $\delta^{13}C$, $\delta^{13}C_{reg}$), $\delta^{13}C = \delta^{13}C_{pre} + \delta^{13}C_{reg}$. The $\delta^{13}C$: P stoichiometric ratio of -1.1 ± 0.06 [μM^{-1}] and the O_2:P stoichiometric ratio of 170 ±10:1 is assumed (Anderson & Sarmiento, 1994; Broecker & Maier-Reimer, 1992). Since $\delta^{13}C_{reg}$ is determined using AOU, we will define this as $\delta^{13}C_{reg,AOU}$:

$$\delta^{13}C_{reg,AOU} = -\frac{1.1}{170}AOU \tag{4}$$

Following the same steps as determining $P_{pre,AOU}$.

$$\delta^{13}C_{pre,AOU} = \delta^{13}C_{C.\ wuellerstorfi} + \frac{1.1}{170}AOU \tag{5}$$

1.2.3 Numerical Sensitivity Experiments

A suite of sensitivity experiments is performed with an ocean circulation and biogeochemistry model. The model is based on the Massachusetts Institute of Technology general circulation model (MITgcm) (Marshall, Adcroft, et al., 1997; Marshall, Hill, et al., 1997) configured for the global domain with $2.8^{\circ}\times 2.8^{\circ}$ resolution on longitude-latitude grid with 23 vertical z-levels following Ito & Follows (2013). The model includes the explicit representation of phosphate, dissolved organic matter, alkalinity, dissolved inorganic carbon, dissolved iron, and dissolved oxygen. The air-sea exchange of CO_2 is parameterized following Wanninkhof (1992). Biological parameterization is adopted from Dutkiewicz et al. (2006) where productivity is limited by the availability of light and nutrients as parameterized by the Monod function. 30% of primary production is instantaneously exported to depth as particulate matter, as opposed to being recycled within the photic zone. This particulate matter is remineralized according to the power function with depth with the exponent of -0.9 (Martin et al., 1987). The model includes two additional tracers, true preformed phosphate (P_{pre}) and preformed oxygen ($O_{2,pre}$) for comparison with the model's determination of $P_{pre,AOU}$. The values of these tracers are set equal to the phosphate and oxygen in the surface grid cell, and they are transported as conservative tracers in the subsurface grid cells.

The model is first spun up with the modern climatological forcing for O(5,000 years) to reach a statistical steady state. The control run is then performed for an additional 2,000 years using the same forcing as the spin up. This run remains close to the steady state, and the time-mean fields from the last 10 years are compared to modern climatology for validation (see results). We performed the sensitivity experiments, initialized from the last time step of the 5,000-year spin-up and integrated for 2,000 years. The model dynamically shifts to a new steady state according to the perturbations and captures large-scale patterns of ocean carbon and nutrient tracers. Integration of 2,000 years can bring the model very close to a new steady state and is considered adequate for the purpose of this study. The last 10 years of each sensitivity experiment are analyzed as the steady state response of the model. We investigate three Southern Ocean scenarios that have been proposed for LGM CO_2 drawdown: increased salinity stratification, increased biological growth rate, and weakened wind stress. The goals of these sensitivity experiments are to evaluate the effects of the Southern Ocean perturbations on the global bottom water oxygen and on preformed phosphate. In the first scenario, increased salinity stratification over the Southern Ocean is achieved by applying a restoring boundary condition for the surface salinity with a Gaussian perturbation of -0.5 PSU centered at 63°S. In the second scenario, increased biological productivity is imposed through a 10× increase in growth rate over the Southern Ocean south of 40°S. This does not consider the dipole nature of the change in export production in the Southern Ocean during the LGM found in Francois et al., 1997; Kohfeld et al., 2005; Kumar et al., 1995; Mortlock et al., 1991. In the third scenario, wind stress is weakened by up to 50% over the Southern Ocean with smoothing at the 30°S transition to avoid abrupt shifts. We also include a fourth sensitivity experiment which incorporates all three scenarios described above: increased stratification, increased biological productivity, and decreased wind stress. The purpose of these idealized experiments is to generate perturbations with plausible physical mechanisms, and they are not meant to reproduce accurately the magnitude of perturbation during the LGM.

We also performed six additional simulations to better characterize the relationship between local and global $P_{pre,AOU}$ under a larger range of circulation and productivity scenarios (Figure 4). These additional scenarios were designed to assess the effect of increased iron deposition and the increased salinity of the polar Southern Ocean due to increased sea ice production for a different study. These experiments include: increased atmospheric dust deposition by 2×, 4× and 8× the modern aeolian iron input, and increased polar surface salinity through the restoring boundary condition with 0.4, 0.6 and 0.8 PSU. Five additional simulations with increased sea ice cover were performed. The sea ice cover is shifted equatorward in five steps by 1, 2, 3, 4 and 5 grid cells which translates to 2.8° to 14° in latitude. The latter change is probably unrealistically large, but the purpose of these perturbation runs is to explore the range of change in the carbon cycle from moderate to extreme changes. These sea-ice experiments are only affecting gas exchange and light availability and do not include circulation changes, or changes in salinity and temperature. Whole ocean changes in salinity and temperature would not influence changes in P_{pre} or $P_{pre,AOU}$.

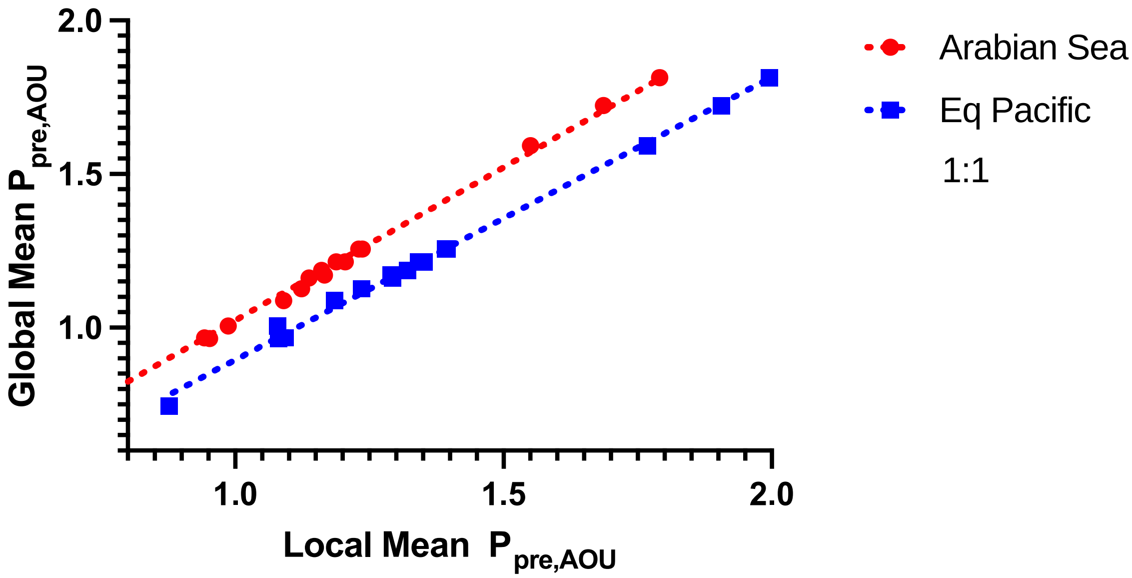

Figure 4 - Local bottom water $P_{pre,AOU}$ versus the global mean $P_{pre,AOU}$ for a variety of perturbations of the MITgcm at the 2730 meter Eastern Equatorial Pacific and 1803 m Arabian Sea core sites.

$P_{pre,AOU}$ can be diagnosed from the model output using AOU determined by subtracting the dissolved oxygen concentration (O_2) from the oxygen solubility; AOU = $O_{2,sat}(S, \theta){-}O_2$. The AOU includes the effect of air-sea disequilibria. Polar oceans are typically undersaturated on the order of 5-15% (Ito et al., 2004), leading to an overestimation of the effect of the biological pump efficiency on carbon drawdown when calculating $P_{pre,AOU}$ instead of true preformed phosphate. The model includes the true preformed phosphate and preformed oxygen. These tracers can be used to accurately determine the disequilibrium component and its impact on the AOU-based estimates of preformed phosphate.

1.3 Results and Discussions

1.3.1 Glacial-Interglacial Changes in O_2

Table 1 and Figure 5 summarize the reconstruction of bottom-water O_2 for the late Holocene and the Last Glacial Maximum. The late Holocene reconstructions of bottom-water oxygen at the Arabian Sea site, the 2,650-meter Eastern Equatorial Pacific, and the 1,364-meter Eastern Pacific site agree with World Ocean Atlas 2013 (WOA13). However, the 2,730-meter Eastern Equatorial Pacific overestimates modern oxygen at that site, while the 1,785-meter South Atlantic site underestimates modern oxygen, according to WOA13 climatology. Two or fewer measurements went into the averages for the late Holocene $\delta^{13}C$ for *C. wuellerstorfi* and *Globobulimina spp*. for the 2,730-meter Eastern Equatorial Pacific site and the 1,785-meter South Atlantic site. Since most cores show significant scatter in $\delta^{13}C$ in contiguous Holocene-aged samples, this low number of measurements could potentially add to the uncertainty in the reconstruction beyond the error indicated in the calibration data set. Additionally, the $O_2 – \Delta\delta^{13}C$ calibration is only based on twelve sites and may either underestimate the error or be biased based on these locations. An expansion of this calibration is needed to fully understand the relationship between $\Delta\delta^{13}C$ and bottom water O_2. Bottom water O_2 was not reconstructed for the late Holocene at the two North Atlantic sites and the 3770-meter South Atlantic site due to the lack of late Holocene *G. affinis* $\delta^{13}C$ data. For all sites, bottom O_2 values from modern climatology (WOA13) are displayed (Table 1 and Figure 5).

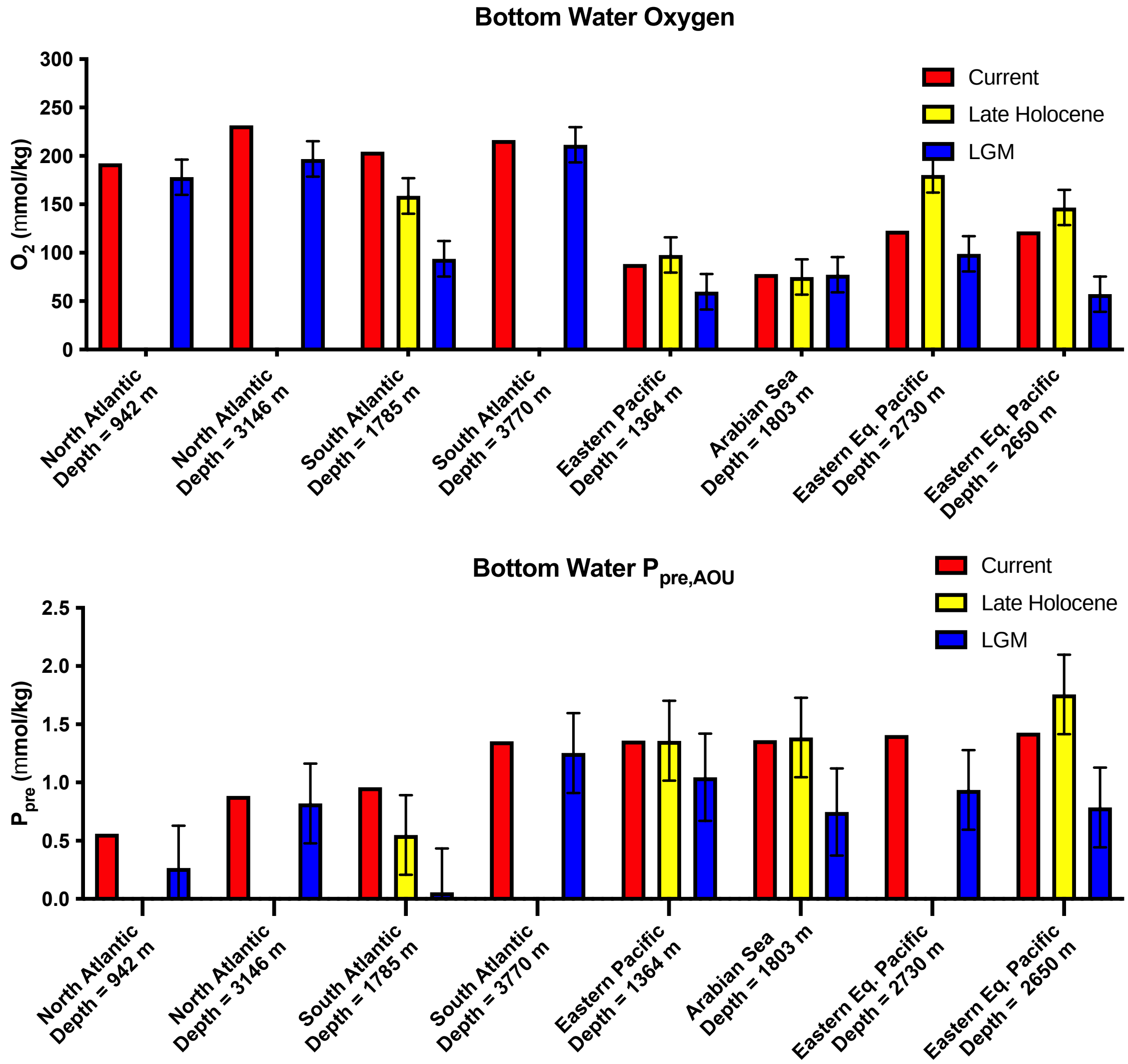

Figure 5 - (top) Bottom water oxygen and (bottom) preformed phosphate reconstructions at eight locations. The modern oceanographic climatology (current) is from World Ocean Atlas 2013 (WOA13). Late Holocene is defined as 0 – 6 ka. LGM is defined as 19 – 23 ka. 1-σ errors are shown.

Reconstruction of the LGM bottom water O_2 shows a decline relative to late Holocene and/or modern values at all sites with most significant declines in deep Eastern

Equatorial Pacific sites, the deep North Atlantic site, and the 1785-meter South Atlantic site (Table 1 and Figure 5). In this study, oxygen change is relatively minor in the 3,770-meter South Atlantic core in contrast to the findings based on this data set in Gottschalk et al. (2016). The difference comes from the type of benthic foraminifera used to estimate the bottom water $\delta^{13}C$. While Gottschalk et al (2016) used *C. kullenbergi* for their epifaunal $\delta^{13}C$, this study uses *C. wuellerstorfi* because *C. wuellerstorfi* most likely better represents $\delta^{13}C$ in the region. Gottschalk et al. (2016) found a significant carbon isotope offset between C. *wuellerstorfi* and C. *kullenbergi* at this South Atlantic core, with C. *wuellerstorf*i isotopically heavier. There is potential that C. *kullenbergi* lives slightly deeper within the sediment compared to C. *wuellestorfi*, making the C. *kullenbergi* signature isotopically lighter than the true bottom-water $\delta^{13}C$ (Jorissen et al., 1998). Additionally, the $O_2 - \Delta\delta^{13}C$ calibration used in this paper is based on *C. wuellerstorfi* $\delta^{13}C$ following Hoogakker et al. (2015).

1.3.2 Glacial-Interglacial Changes in Preformed PO4

Where sufficient foraminifera-based proxy data were available to reconstruct late Holocene preformed phosphate, the values from these sites are in agreement with the values calculated using modern ocean climatological values within 2σ (Boyer et al., 2013) (Table 1, Figure 5, Figure 6). This is despite the lack of agreement between reconstructed and observed O_2 in the 2,730-meter Eastern Equatorial site and 1,785-meter South Atlantic site. This stems from the fact that a large portion of the error in $P_{pre,AOU}$ reconstructions comes from the conversion of Cd/Ca to phosphate, making the uncertainty in oxygen a relatively small contribution.

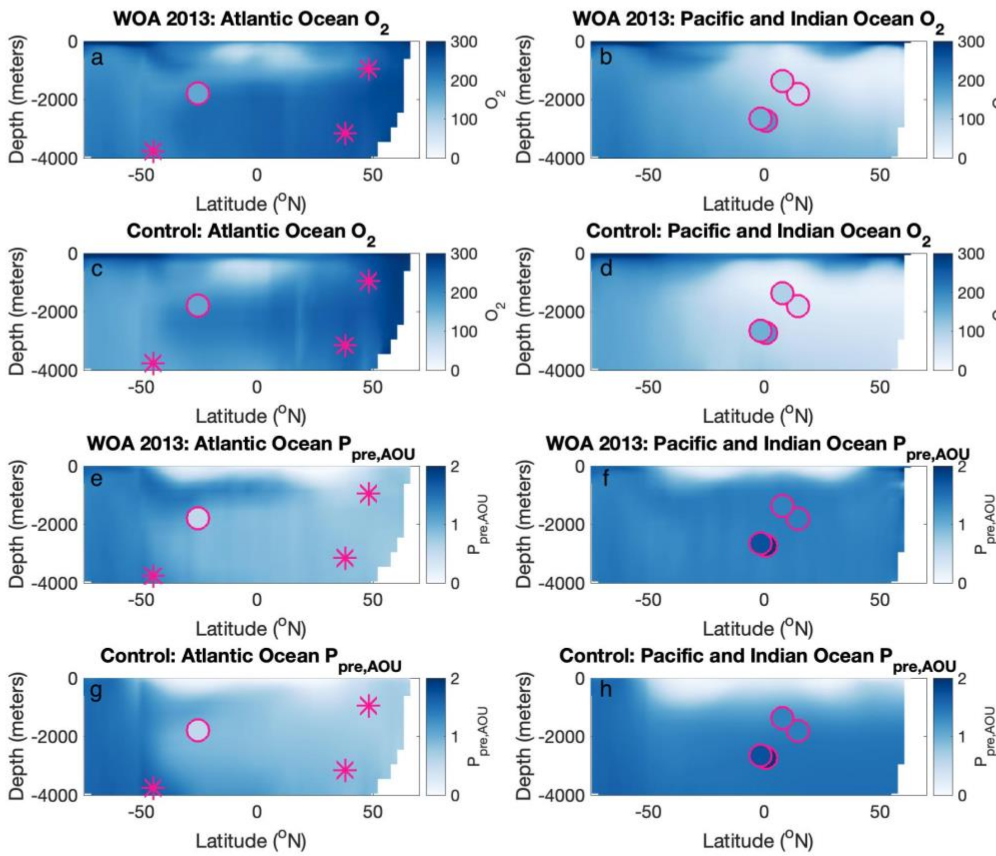

Figure 6 - Observed O_2 (µmol/kg) based on World Ocean Atlas (WOA13) for the zonally averaged transects of the Atlantic Ocean (a) and Pacific and Indian Ocean (b). Simulated O_2 from the control run for the Atlantic Ocean (c) and Pacific and Indian Ocean (d). Determined $P_{pre,AOU}$ (µmol/kg) based on World Ocean Atlas (WOA13) for the zonally averaged transects of the Atlantic Ocean (e) and Pacific and Indian Ocean (f). Simulated $P_{pre,AOU}$ for the Atlantic Ocean (g) and Pacific and Indian Ocean (h).

The LGM $P_{pre,AOU}$ was reduced from the modern value at all sites, with the most significant reductions in the deep Pacific and Indian Oceans and smaller reductions in the deep Atlantic. The 1,785-meter South Atlantic site shows the most significant decrease in preformed phosphate, but due to its relatively shallow depth, it could be influenced by Antarctic Intermediate Water (AAIW) or Glacial North Atlantic Intermediate Water (GNAIW). An increase in iron fertilization in the Subantarctic Zone (SAZ) would lower the preformed phosphate signature of AAIW (Hain et al., 2010; Keir, 1988; Ridgwell & Watson, 2002). While the average change in $P_{pre,AOU}$ (LGM-Modern) at the core sites is -0.42 ± 0.20 μM (2σ), based on the conservative property of preformed nutrients, we expect that the global mean $P_{pre,AOU}$ is most likely represented by the values in Pacific Deep Water and Indian Deep Waters. These water masses are most voluminous and have dominant influences on the global inventory. Because there is no deepwater formation in the Pacific and Indian basins today, these deep waters reflect the mixing product of source waters from the northern North Atlantic and the polar Southern Ocean. Our model simulations demonstrate the overall validity of this approach, showing that the changes of global mean preformed phosphate are closely correlated with the changes of bottom water $P_{pre,AOU}$ at the deep Indian site and deep Equatorial Pacific site (Figure 4). This relationship holds through a variety of biological and physical perturbations, but the slope of about 0.96 suggests that determinations of global mean $P_{pre,AOU}$ from the deep Indian and Pacific sites alone will very slightly overestimate the global mean P_{pre} changes by about 4%. This overestimate is due to neglect of the upper ocean $P_{pre,AOU}$, which is lower than in the deep ocean because of more complete utilization of surface nutrients where these less dense waters outcrop at the surface. This relationship should hold going back in time if the deep ocean is filled by waters from only the Southern Ocean and the North Atlantic. If there were other sources of deep-water formation during the LGM, such as the North Pacific (Matsumoto et al., 2002; Rae et al., 2014) , this relationship will not be upheld. Our best estimate of mean ocean decrease in $P_{pre,AOU}$ (LGM – Modern) is -0.53 ± 0.13 µM ($2\sigma, see\ supplement$), based on the average decrease at the sites in the deep (>1500 meters) Indian and Pacific core sites.

Disregarding air-sea disequilibrium effects, there are two possible explanations for the decrease of glacial preformed phosphate: (1) changes in volumetric contributions of different deep-water masses and (2) changes in end-member concentrations in these water masses. During the LGM, many studies have suggested that there was a shoaling of North Atlantic Deep Waters (NADW) to a depth of less than 2000 meters, often referred to as Glacial North Atlantic Intermediate Waters (Gebbie, 2014; Lynch-Stieglitz et al., 2007; Oppo & Lehman, 1993). This would suggest the 942-meter North Atlantic site, MD99-2328, bathes in GNAIW during the LGM. Given that modern NADW has a $P_{pre,AOU}$ of 0.8 µM (Sarmiento & Gruber, 2006) and LGM P_{pre} is 0.3 µM at this 942-meter site, this implies a ~ 0.5µM lower northern P_{pre} end-member during the LGM. Modern southern sourced waters have a $P_{pre,AOU}$ of 1.8 µM (Figure 2) (Sarmiento & Gruber, 2006). Assuming that the deep South Atlantic site, MD07-3076Q, is predominately sourced by southern sourced waters, the LGM $P_{pre,AOU}$ at this site of 1.3µM also indicates a ~ 0.5µM lower southern

$P_{pre,AOU}$ end-member during the LGM. The deep North Atlantic site, MD95-2042, has a similar LGM $P_{pre,AOU}$ to the deep South Atlantic site, corroborating the idea of a more intrusive southern sourced water mass during the LGM. This implies that the decrease in glacial preformed phosphate cannot only be due to changes in water mass distribution since both the southern and northern end members are decreasing.

Oppo et al. (2018) also infer lower P_{pre} of GNAIW based on an inversion of deep-water carbon isotope and seawater Cd reconstructions, but in contrast to this study, find little change in preformed PO_4 in the southern sourced waters in the deep LGM Atlantic. Consequently, they reconstruct higher preformed PO_4 in the deep Atlantic where northern sourced waters are replaced by southern sourced waters. While both approaches share the LGM deep-water Cd data set, ours separates the preformed vs. regenerated components based on AOU, whereas theirs infers regeneration based on the amount of remineralization required to match the spatial patterns in the Cd and $\delta^{13}C$ data as water masses are traced from their origin into the deep sea. The relative fraction of preformed vs. regenerated nutrients in their inversion is sensitive to constraints on surface water $\delta^{13}C$ in the Southern Ocean. It will require more deep-water oxygen data as well as better reconstructions of nutrients and $\delta^{13}C$ near the water mass formation regions to better understand the changes to the preformed phosphate endmembers for LGM deep waters.

Yu et al., 2019, based on a multi-proxy approach using carbonate ion and nutrient concentrations to estimate air-sea CO_2 exchange signals, found an increase in the efficiency of the North Atlantic carbon pump. Our finding of a decrease in $P_{pre,AOU}$ in the North Atlantic is in agreement with their reconstruction, indicating an increase in the biological pump efficiency in the North Atlantic. Reconstructions of the Southern Ocean surface nitrate consumption from foraminifera-bound, deep sea coral bound, and diatom-bound nitrogen isotopes indicate more complete nitrate consumption during the Last Glacial (Ai et al., 2020; Kemeny et al., 2018; Martínez-García et al., 2014; Studer et al., 2015; Wang et al., 2017). More surface nitrate consumption in the Southern Ocean indicates an increase in the biological pump efficiency and a decrease in $P_{pre,AOU}$ for southern sourced waters. Our findings of a decrease in $P_{pre,AOU}$ in the deep equatorial Pacific is in agreement with these reconstructions.

1.3.3 Glacial-Interglacial Changes in Preformed $\delta^{13}C$

Preformed $\delta^{13}C$ provides a semi-independent proxy for biological pump efficiency (See Section 1.3.6). It is important to note that both $\delta^{13}C_{pre,AOU}$ and $P_{pre,AOU}$ are determined using AOU. From the 5 existing cores with Holocene *Globobulimina spp.* data, we see an average change of $\delta^{13}C_{pre,AOU}$ of $0.03 \pm 0.16‰$ (2σ) (Table 1, Figure 7). Similar to $P_{pre,AOU}$, we expect the global change in $\delta^{13}C_{pre,AOU}$ to be represented by the changes in the deep Equatorial Pacific and Arabian Sea. Assuming a one-to-one relationship between the deep Indo-Pacific changes in $\delta^{13}C_{pre,AOU}$ and changes in global mean $\delta^{13}C_{pre,AOU}$, our best estimate for mean ocean changes of $\delta^{13}C_{pre,AOU}$, derived from the average changes at the deep Indian and Pacific sites, is $0.00 \pm 0.14‰$ (2σ). Unlike for preformed phosphate, the whole ocean changes in $\delta^{13}C$ must be accounted for in order to determine changes in biological pump efficiency.

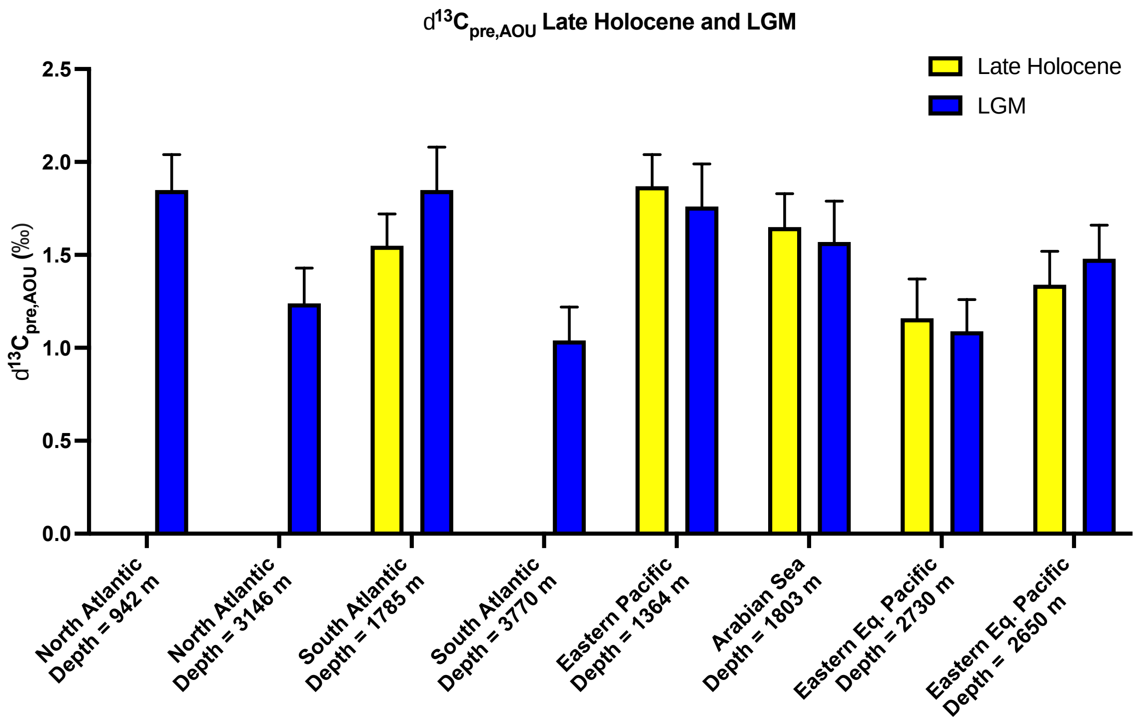

Figure 7 - Preformed $\delta^{13}C_{pre.AOU}$ reconstructions for 8 core locations for the Late Holocene and LGM.

The linear relationship between calculated LGM $\delta^{13}C_{pre,AOU}$ and $P_{pre,AOU}$, excluding the intermediate Eastern Pacific core site and the shallower South Atlantic site, does not conflict with a two end-member oceanic system, with a North Atlantic source and a southern source of deep waters. (Figure 8). Due to their relatively shallow depth, intermediate water masses would contribute to the waters at the 1364-meter Eastern Pacific core site, as well as the shallower South Atlantic site.

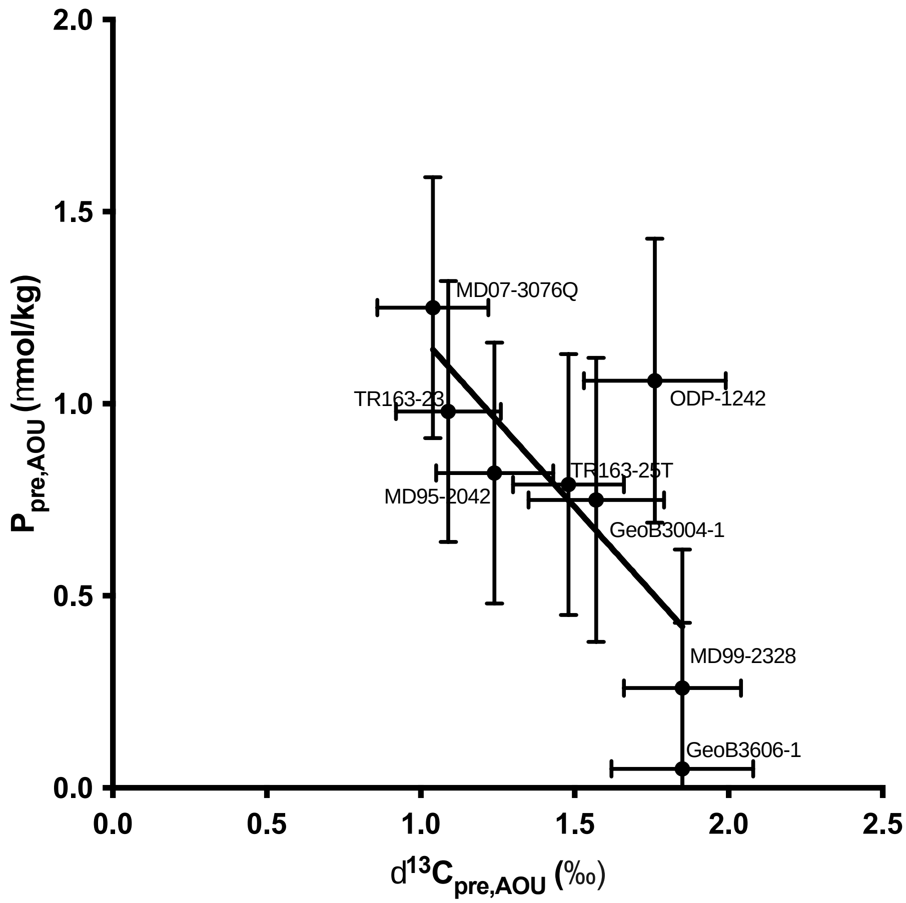

Figure 8 - $P_{pre,AOU}$ versus $\delta^{13}C_{pre,AOU}$ plot at each of the eight core-sites. A linear fit is performed through six of the seven core-sites. The RMSE of this fit is 0.17, with an R2 correlation of 0.78. Core site ODP-1242 and GeoB3606-1 is relatively shallow and would be influenced from other intermediate waters.

1.3.4 Mechanisms for Changes in Oxygen and Preformed PO_4

Despite its simplicity, the model's control run reproduces the large-scale structure of observed bottom water O_2 and preformed phosphate (Figure 6). Newly formed North Atlantic Deep Water is enriched in O_2, and it is transported southward by the deep western boundary current. The model underestimates the bottom water O_2 in the Southern Hemisphere on the order of $O(-100\mu M)$ likely due to the relatively weak bottom water ventilation. Relatively low bottom water O_2 is a common issue with coarse-resolution global ocean models with incomplete representation of bottom water formation such as shelf convection and coastal polynyas. While this is not desirable, it does not preclude us from using the model because the model still represents relevant physical and bio-geochemical processes, including wind-driven upwelling, stratification, and the biological pump. The coarse resolution of this model enables multiple millennial integrations that are required for the equilibration of the deep water. The model represents the large-scale distribution of preformed phosphate reasonably well. The northern deep water contains relatively low preformed phosphate (~ 0.8 μM), and it makes a sharp contrast with the relatively high preformed nutrient of the southern deep water (~ 1.8 μM) (Figure 6). The boundary exists around $\sim 45^{\circ}$S where the two deep water masses interface with one another.

Here, we highlight results from three experiments, (1) increased Antarctic stratification, (2) increased biological activity and (3) weakened Southern Ocean winds (Figure 9, Figure 10, Figure 11). Changes in storm track activity during the LGM can cause regional changes in the precipitation rate over the Southern Ocean. The atmospheric model simulations and paleoceanographic proxy data do not form a consensus, but this is a possible response to the westerly wind shift (Chavaillaz et al., 2013; Kohfeld et al., 2013). Increased Antarctic stratification or weakened Southern Ocean winds causes a reduced vertical supply of nutrients and increases surface residence time, which can lead to the depletion of surface nutrients by phytoplankton. These three perturbations examine mechanisms based in the Southern Ocean that have been proposed to increase the biological pump efficiency, and thus decrease deep water O_2 and increase the storage of biologically sequestered carbon. The model simulations with weaker winds, increased stratification, and/or increased biological activity reproduce the decline in the bottom water O_2 that is reconstructed for the LGM at the South Atlantic site, Arabian Sea site, and the two deep Eastern Equatorial Pacific sites. The increased stratification and decreased wind stress experiments show an increase of bottom water O_2 at the 3,146 meter North Atlantic site, in disagreement with the LGM reconstruction, most likely due to a decrease in the model's deep-water formation in the Southern Ocean (Figure 12).

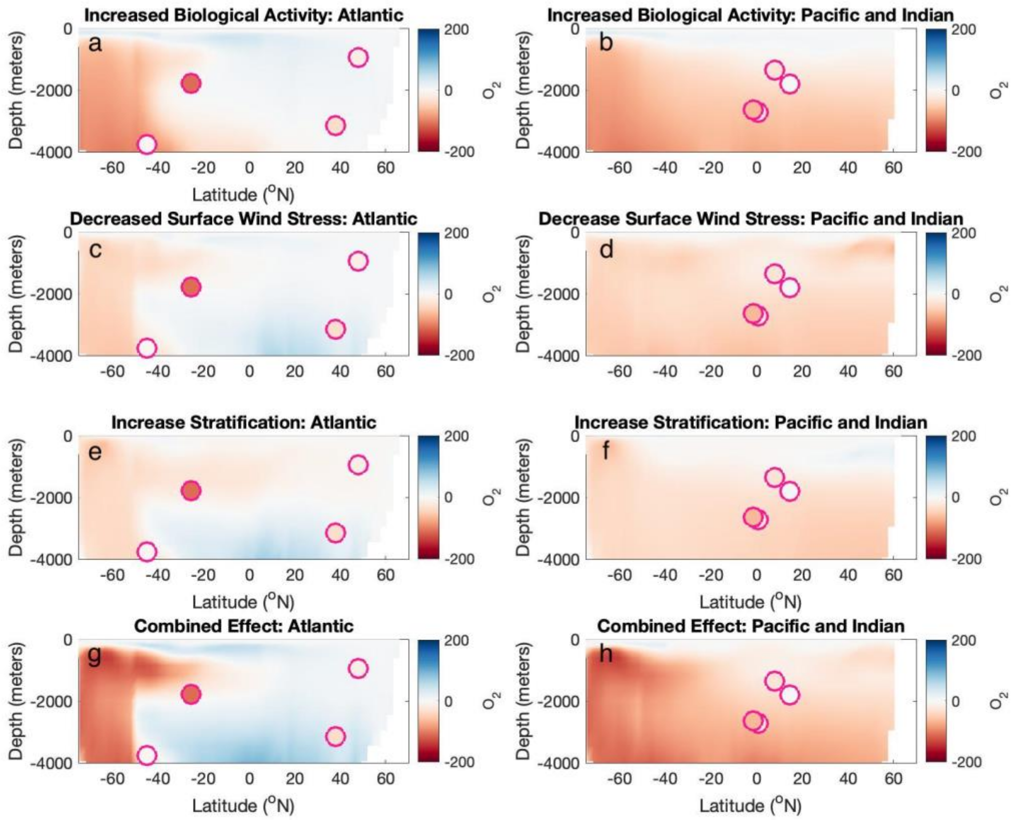

Figure 9 - Simulated oxygen (µmol/kg) anomalies with respect to the control run for (a,b) increased stratification, (c,d) increased biological productivity, and (e,f) weakened Southern Ocean for the Atlantic Ocean (a, c, e, f) and Pacific and Indian Ocean (b, d, f, g). The circle's location and color indicate reconstructed bottom water O_2 from 19 – 23 ka.

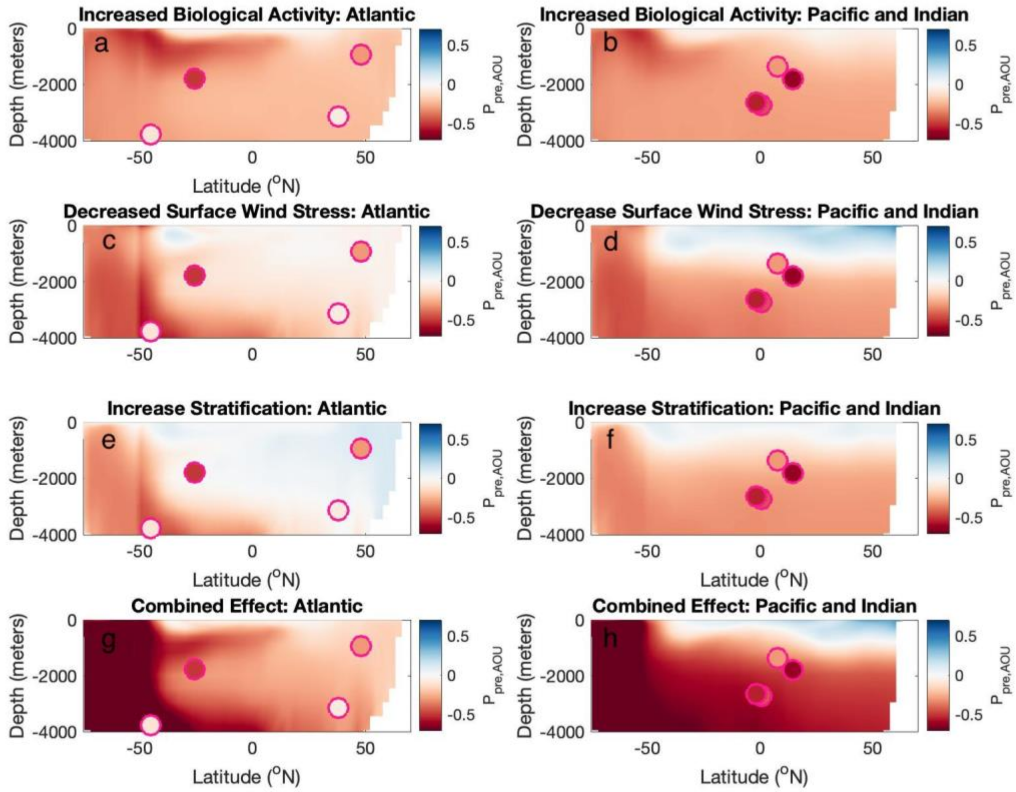

Figure 10 - Simulated $P_{pre,AOU}$ (µmol/kg) anomalies with respect to the control run for (a,b) increased stratification, (c,d) increased biological productivity, and (e,f) weakened Southern Ocean for the Atlantic Ocean (a, c, e, f) and Pacific and Indian Ocean (b, d, f, g). The circle's location and color indicate reconstructed $P_{pre,AOU}$ from 19 – 23 ka.

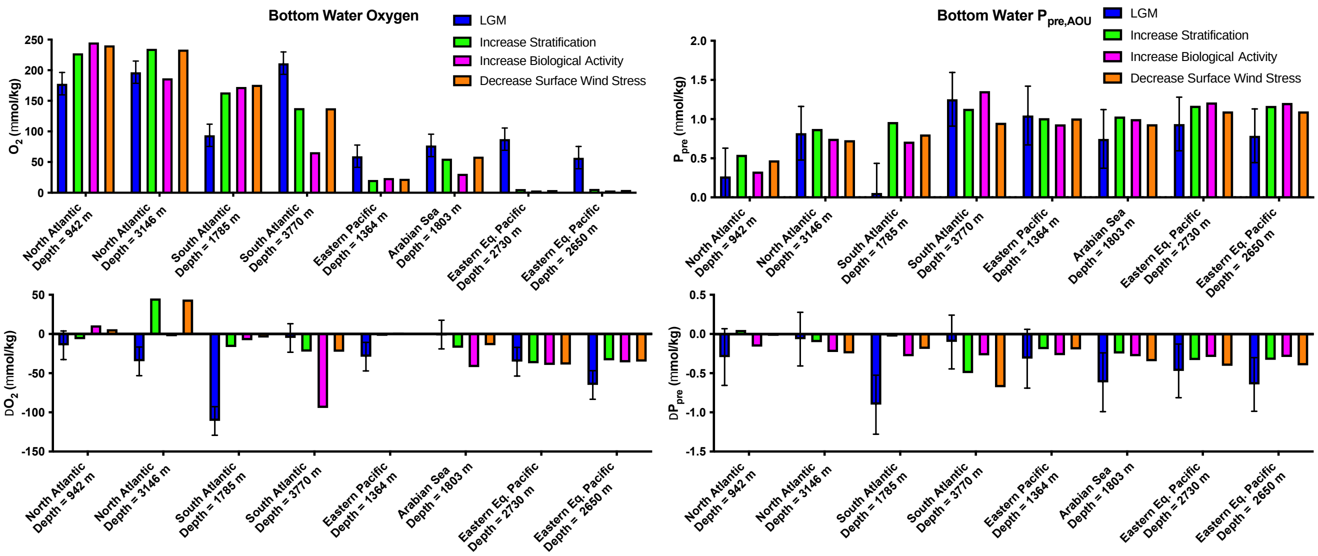

Figure 11 - Bottom water (top-left) oxygen and (top-right) preformed phosphate at each core location for the LGM proxy and numerical sensitivity experiments: increase stratification, increase biological activity, and decrease surface wind stress. Changes in bottom-water oxygen (bottom-left) and preformed phosphate (bottom-right) for the experiments (Perturbation – Control) and data (LGM – Modern) at each core location. 1-σ errors are shown.

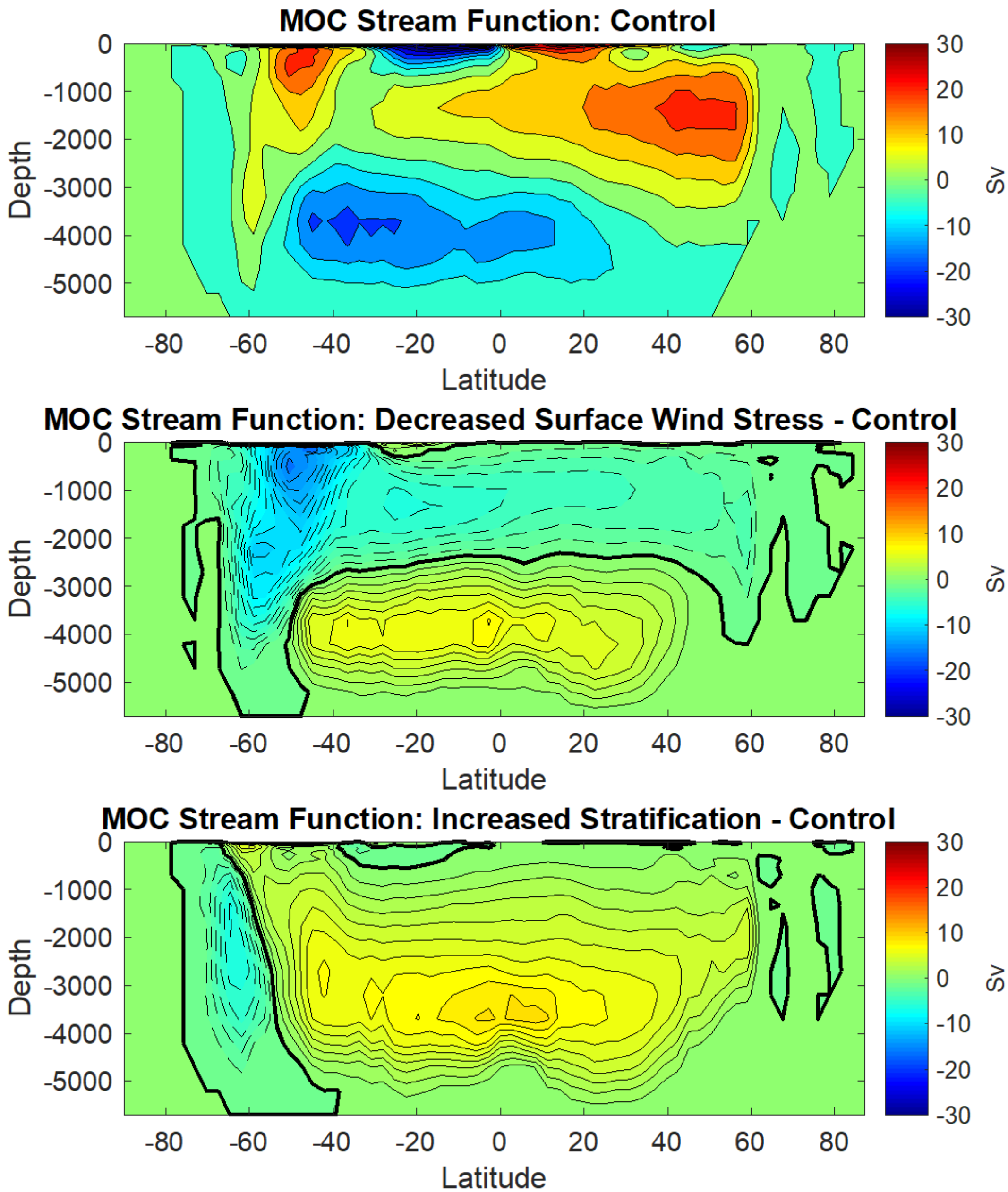

Figure 12 - Global Meridional Overturning Circulation (MOC) stream function measured in Sverdrups (Sv) for the control run (top), the decreased surface wind stress simulation-control difference (middle), the increased stratification simulation-control difference (bottom).

All three sensitivity studies reproduce the sign of the LGM-Modern change of P_{pre} and $P_{pre,AOU}$ seen in the reconstructions at all core sites (Figure 11) and an overall decrease of the global mean preformed nutrients, although no mechanism, by itself, can fully match the reconstructed LGM-Holocene change. The increased stratification, stronger biological activity, and weakened wind stress simulations decreased global preformed phosphate by 0.2μM , 0.3 μM, and 0.3μM , respectively. Combining these mechanisms, a stronger decrease of preformed phosphate of 0.5μM is observed, closer to the LGM-Holocene reconstruction from the foraminifera data.

Comparing the spatial patterns in Figure 9, the increased biological activity causes the most intense and widespread O_2 decline, especially in the Southern Ocean, but lacks significant imprint in the North Atlantic. In contrast, the weakened Southern Ocean wind results in the strongest decline of bottom water P_{pre} not only in the Southern Ocean but also in the northern basins due to changes in the overturning circulation (Figure 10). In this particular simulation, the weaker westerly winds slowed down both upper and lower cell MOC of the Southern Ocean (Figure 12). These results indicate that biological activity changes can leave a strong imprint in the bottom water O_2 locally in the Southern Ocean, and the circulation change induced by altered wind stress can spread the perturbation far afield to the northern basins. Overall, the patterns of change observed in the sensitivity experiments with decreased surface wind stress and increased stratification over the Southern Ocean best match the LGM reconstructions (Figure 9, Figure 10, Figure 11).

1.3.5 Using $P_{pre,AOU}$ versus P_{pre} to determine Atmopsheric pCO_2 drawdown

Air-sea disequilibrium has the potential to alter our reconstruction of preformed phosphate. Since AOU is determined from oxygen saturation and surface oxygen is not fully saturated in the surface ocean, especially at polar regions, our $P_{pre,AOU}$ reconstructions include the effect of oxygen disequilibrium. Previous studies, such as (Cliff et al., 2021; Khatiwala et al., 2019), found that using changes in AOU can overestimate carbon drawdown due to changes in the biological pump efficiency due to oxygen disequilibrium (undersaturation). We investigate these concerns by comparing P_{pre} and $P_{pre,AOU}$ in our suite of sensitivity experiments. Figure 13 shows changes in globally averaged $P_{pre,AOU}$ and P_{pre} versus atmospheric pCO_2 drawdown for all sensitivity experiments. Due to the model bias with the low O_2 concentration of the deep North Pacific, there is widespread anoxia in some of the sensitivity runs. When this happens, organic matter continues to be respired, but oxygen cannot be set lower than zero, thus decoupling AOU and the respiration of organic matter in the model. This leads to an overestimation of $P_{pre,AOU}$ when determining $P_{pre,AOU}$ using equation 1 in some of the sensitivity experiments. Since there is no indication of widespread anoxia in the real ocean over the last glacial cycle, we chose to sidestep this inconsistency rather than try to change the model to properly model the chemistry of anoxic ocean. To remove this inconsistency, $P_{pre,AOU}$ in the model can be re-calculated using equation 6.

$$P_{pre,AOU} = P_{pre} - \frac{1}{170}\left(O_{2,sat} - O_{2,pre}\right) \qquad (6)$$

As expected, the global $P_{pre,AOU}$ in the control run slightly underestimated the control run's true global preformed phosphate inventory by 0.1 µM, due to the oxygen undersaturation. For an increase in biological drawdown and/or more sluggish overturning circulation, changes in $P_{pre,AOU}$ slightly underestimate the changes in true preformed phosphate and, consequently, underestimate the LGM CO_2 drawdown due to the soft tissue pump (Figure 13). This is because the enhancement of biological production and/or the reduction of surface-subsurface exchange will reduce O_2 undersaturation. This in turn will allow $P_{pre,AOU}$ will approach true P_{pre}. The maximum underestimation is the combination run with $P_{pre,AOU}$ underestimating the true change in preformed phosphate by about 0.08 µM. This corresponds to an underestimation of CO_2 drawdown by about 10 ppm.

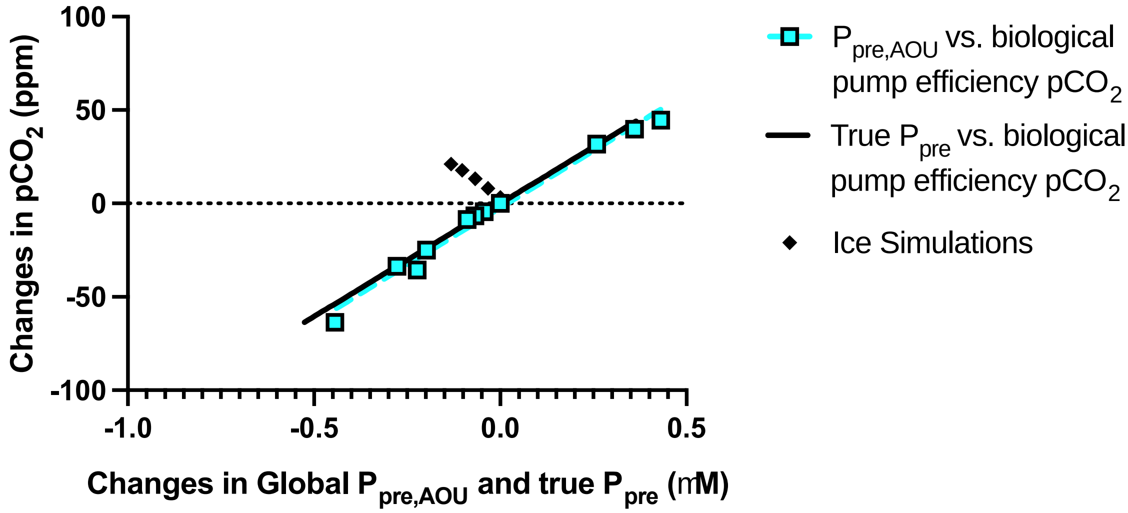

Figure 13 - The solid black line is the theoretical relationship between changes in true preformed phosphate and atmospheric pCO_2 (121 ppm/µM). Squares are the changes in atmospheric CO_2 due to changes in the biological pump efficiency with respect to the respective model's change in globally average true P_{pre} (perturbation-control), excluding the ice simulations. The diamonds represent the increase Southern Ocean sea-ice extent simulations.

Previous studies raised the possibility that the lower CO_2 during the LGM was due to greater sea-ice cover, which prevents the outgassing of the carbon-enriched waters from the Antarctic ventilation regions (Ferreira et al., 2018; Marzocchi & Jansen, 2019; Stephens & Keeling, 2000). In these studies, this lowering of CO_2 is due to an increase in air-sea disequilibrium of CO_2. Since reconstructions of $P_{pre,AOU}$ are influenced by air-sea disequilibrium of O_2, our sea-ice expansion runs can show insight on how much $P_{pre,AOU}$ diverges from true P_{pre} due to an increase in sea-ice extent. In these scenarios, sea-ice extent can influence both biological nutrient uptake as well as air-sea disequilibrium of O_2, both of which can lead to changes in $P_{pre,AOU}$. Our sea-ice expansion runs show slight decreases in $P_{pre,AOU}$ and slight increases in true P_{pre} with expanding Southern Ocean sea-ice extent (Figure 14). The slight decrease in $P_{pre,AOU}$ is due to an increase in the Southern Ocean air-sea disequilibrium (undersaturation) of O_2. The slight increase in true P_{pre} is due to a decrease in Southern Ocean biological pump due to an increase in sea-ice cover. Overall, changes in $P_{pre,AOU}$ will be more negative than changes in true P_{pre} under expanding sea-ice conditions.

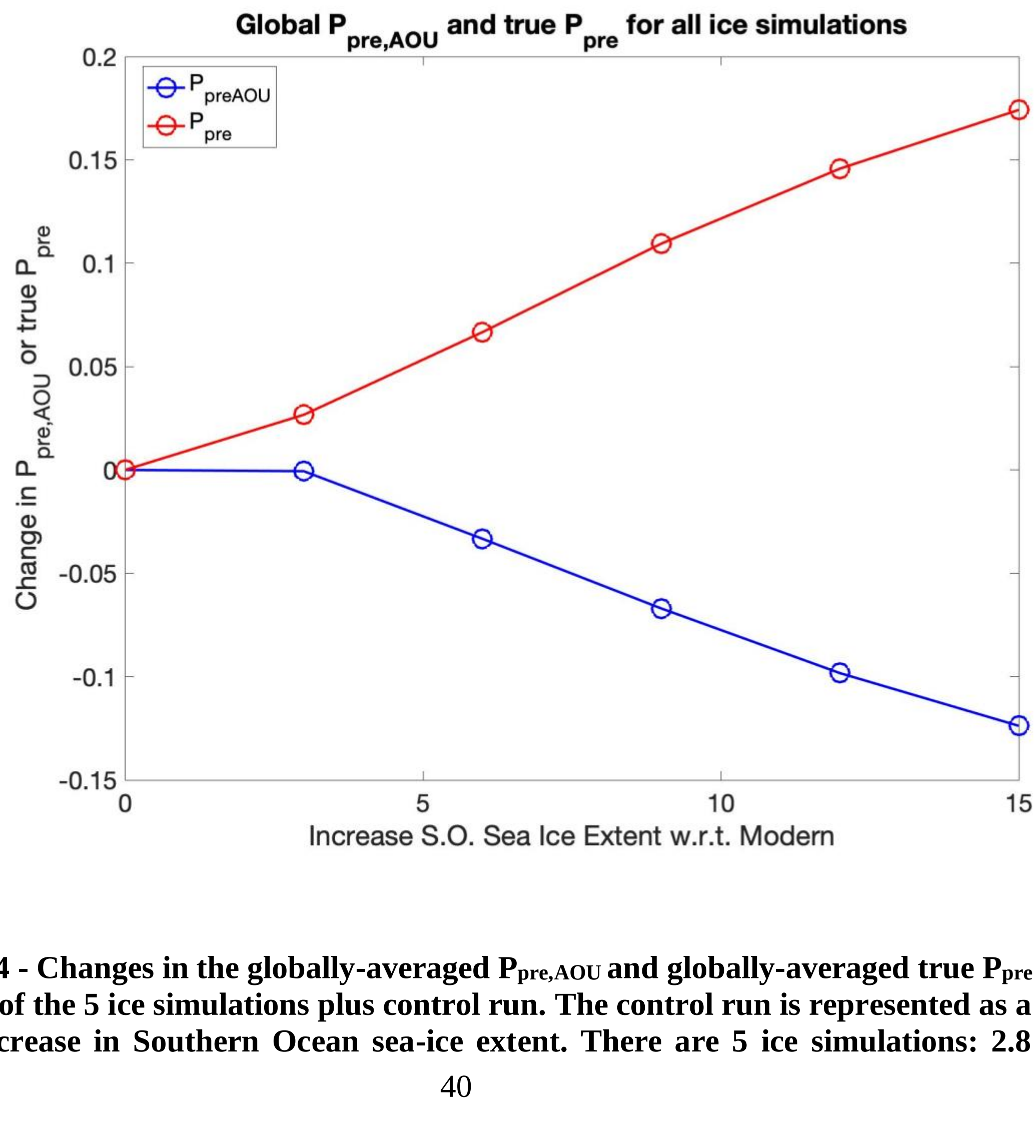

Figure 14 - Changes in the globally-averaged $P_{pre,AOU}$ and globally-averaged true P_{pre} for each of the 5 ice simulations plus control run. The control run is represented as a 0 deg increase in Southern Ocean sea-ice extent. There are 5 ice simulations: 2.8

degree increase, 5.6 degree increase, 8.4 degree increase, 11.2 degree increase, and 14 degree increase in Southern Ocean sea-ice latitudinal extent with respect to modern.

Reconstructions of LGM Southern Ocean sea-ice extent can help provide an estimate on how much P_{pre} diverges from $P_{pre,AOU}$ under increasing sea-ice extent. LGM Southern Ocean sea-ice extent has been reconstructed through lithology of seafloor sediments, diatom abundances, and, more recently, oxygen isotopes in foraminifera (C. S. Allen et al., 2011; Burckle et al., 1982; CLIMAP PROJECT MEMBERS, 1976; Crosta et al., 1998; Gersonde et al., 2003; Hays et al., 1976; Lund et al., 2021). The lithological data shows an increase of sea-ice extent by 5 degrees of latitude (CLIMAP PROJECT MEMBERS, 1976). Similarly, the three estimates using diatom assemblages show similar 5 – 6 degree of latitude increase of sea-ice extent (C. S. Allen et al., 2011; Crosta et al., 1998; Gersonde et al., 2003). Assuming a Southern Ocea n sea-ice expansion of no more than 6 degrees North, this corresponds to only a 0.1 µM overestimation, leading to an overestimation of CO_2 drawdown due to changes in the biological pump efficiency of 12 ppm, suggesting that the air-sea disequilibrium effect from sea-ice plays a minor yet significant role in our reconstruction of preformed phosphate.

Excluding the sea-ice simulations, the model shows a very similar slope of 122 ppm/µM for the relationship between changes in $P_{pre,AOU}$ and atmospheric CO_2 drawdown due to the biological pump efficiency in comparison to using true P_{pre} (slope = 121 ppm/µM) (Figure 13). Due to the uncertainty behind changes in air-sea disequilibrium during the LGM, we will use the theoretical 121 ppm/µM relationship when determining atmospheric pCO_2 drawdown due to changes in $P_{pre,AOU}$, acknowledging that this is most likely a slight underestimation.

1.3.6 Quantifying LGM CO_2 drawdown from $P_{pre,AOU}$ and $\delta^{13}C_{pre,AOU}$

We confirm that the theoretically derived relationship that was found earlier between mean ocean preformed PO_4 and atmospheric pCO_2 is also seen in the model scenarios (Figure 13). Using the mean ocean $P_{pre,AOU}$ estimate of -0.53 ± 0.13 µM which was inferred from the average change in deep Pacific and Indian ocean cores (>1500 meters), we estimate -64 ± 28 ppm drawdown of atmospheric CO_2 due to the increase of the biological pump efficiency, which explains a significant fraction of the glacial-interglacial change. Unlike true preformed PO_4, our $P_{pre,AOU}$ reconstructions incorporate a minor influence from the oxygen disequilibrium. Because of this, the estimated drawdown of atmospheric CO_2 using the mean ocean $P_{pre,AOU}$ includes an additional 12 ppm of error that could be caused from an overestimation due to an increase in Southern Ocean sea-ice extent during the LGM. Additionally, temperature effects on carbon solubility combined with opposing salinity effects and terrestrial carbon changes, represent a pCO_2 drawdown of 6.5 ± 16.5 ppm (Table 2) (Ciais et al., 2012; Fairbanks, 1989; Headly & Severinghaus, 2007; Sigman & Boyle, 2000). Accounting for carbonate compensation gives an enhancement of 16 – 32.5%, giving a total change of 87 ± 40 ppm (Table 2) (Hain et al., 2010).

Table 2 - The expected drawdown of CO2 for several processes during the LGM.

Causes for the LGM drawdown of CO2	**ΔCO2 (ppm)**	**References**
Terrestrial Carbon Decrease (330±550 Pg C)	10±16.5	Ciais et al. 2012, Sigman et al. 2000
Temperature (2.6±0.2 ˚C)	-23±2	Bereiter et al. 2018
Salinity (~3.3±0.1%)	6.5±0.5	Fairbanks et al. 1989, Sigman et al. 2000
Biological Pump Efficiency	-64±28	This study
Net before carbonate compensation mechanism	-70±32	
Net after carbonate compensation mechanism (16-32.5%)	**-87±40**	Hain et al. 2010
Observed interglacial-glacial change	**-90**	Petit et al. 1999, EPICA community members 2004.

Similarly to $P_{pre,AOU}$, we can determine atmospheric pCO_2 drawdown due to an increase of the biological pump efficiency using $\delta^{13}C_{pre,AOU}$. Unlike phosphate on interglacial-glacial timescales, the global average $\delta^{13}C$ of DIC in the ocean is not constant.

Consequently, globally averaged preformed $\delta^{13}C$ is not linearly correlated with atmospheric pCO_2. However, there are many studies that estimated the change of $\delta^{13}C$ of ocean DIC between the pre-Industrial and the LGM ($\Delta\delta^{13}C$) (e.g. Ciais et al., 2012; Gebbie et al., 2015; Peterson et al., 2014; Tagliabue et al., 2009). Gebbie et al. (2015) estimated that the globally averaged LGM $\delta^{13}C$ was $0.32 \pm 0.20‰$ more depleted in comparison to the pre-industrial. From our $\delta^{13}C_{pre,AOU}$ reconstructions, the mean ocean change from LGM to Late Holocene $\delta^{13}C_{pre,AOU}$ is $0.00 \pm 0.14‰$, based on the average change in the deep Indian and Pacific sites (>1500 meters). Mean ocean change in $\delta^{13}C_{reg,AOU}$ can be derived from mean ocean change in performed $\delta^{13}C$ changes and total mean ocean change in $\delta^{13}C$.

$$\Delta\delta^{13}C_{reg,AOU} = \Delta\delta^{13}C - \Delta\delta^{13}C_{pre,AOU} \qquad (6)$$

This equation yields LGM mean ocean $\delta^{13}C_{reg,AOU}$ that is $0.32 \pm 0.24‰$ lower than the Late Holocene, indicating more regenerated carbon in the deep ocean. There is a relationship between regenerated phosphate and regenerated $\delta^{13}C$ of -1.1 ±0.06 [μM^{-1}] (Broecker & Maier-Reimer, 1992). Thus, the $\delta^{13}C_{reg,AOU}$ can be used to determine that the LGM mean ocean $P_{reg,AOU}$ is 0.35 ± 0.31 μM greater than the Late Holocene. Since $\Delta P_{pre,AOU}$ = -$\Delta P_{reg,AOU}$, an estimate of LGM mean ocean $P_{pre,AOU}$ based on mean ocean $\delta^{13}C_{reg,AOU}$ is 0.35 ± 0.31 μM lower than the Holocene, similar to the lowering of 0.53 ± 0.13 μM estimated using Cd_w, but with a larger uncertainty. The estimate of the global change of $\Delta P_{pre,AOU}$ derived from the global change of $\Delta\delta^{13}C_{pre,AOU}$ corresponds to a drawdown of pCO_2 of -42 ± 50 ppm due to an increase in the biological pump efficiency, again agreeing within error with the pCO_2 drawdown estimate derived from the Cd based preformed phosphate estimate.

Consistent with the results from $P_{pre,AOU}$, the model sensitivity studies from section 1.3.4 show that no single mechanism that was explored can produce the required change in the biological pump to fully explain the Holocene-LGM CO_2 drawdown (Table 3). The biological pump efficiency component of the combined scenario can account for a change in atmospheric CO_2 of 63 ppm, similar to the reconstructed drawdown, but we caution that these sensitivity studies used a modern base state, and the scenarios were all pushed to extremes rather than being based on realistic LGM conditions. However, the patterns in $P_{pre,AOU}$ and O_2 produced by these mechanisms suggest that they remain viable candidates to explain glacial-interglacial CO_2 change.

Table 3 - Carbon reservoir changes for a variety of perturbations of the MITgcm: (1) control, (2) increased biological activity, (3) decreased wind stress, (4) increased stratification, (5) combining 2, 3, and 4, and (6) 5.6 degree northward increase of of Southern Ocean sea-ice extent. Following the methodology in (Ferreira et al., 2018) and (Ito & Follows, 2013), we determined the individual effects of on the carbon reservoir due to changes in solubility (temperature and salinity dependence), biological pump (organic), carbonate pump, and the residual disequilibrium term.

Sensitivity Runs	**$pCO_{2,atm}$ (ppm)**	**$\Delta pCO_{2,atm}$ (ppm)**				
		Net	Solubility	Organic	Carbonate	Disequilibrium
Control	279.2	0	0	0	0	0
Increased Biological Activity	241.7	-37.5	0	-33.5	-3	-1
Decreased Wind Stress	249.8	-29.4	-0.1	-35.3	1.2	4.8
Increased Stratification	279.3	-10.4	10.5	-24.5	1.3	12.8
Combined	233.4	-45.8	8.1	-63.4	-0.8	10.2
Increased S.O. Sea-Ice Extent: 5.6 Deg N	279.7	0	0	1.7	0.1	-1.3

1.4 Conclusions

While initial attempts using box models (Knox & McElroy, 1984; Sarmiento & Toggweiler, 1984; Siegenthaler & Wenk, 1984) were able to produce the observed CO_2 drawdown in LGM simulations using polar nutrient drawdown, biological pump scenarios in more complex ocean models have been unable to account for the full observed magnitude of the Glacial-Interglacial CO_2 change (Archer et al., 2000a; Archer et al., 2000b). Fully interactive Earth System model simulations of glacial ocean circulation, climate, and carbon dioxide remain poorly constrained (Ganopolski & Brovkin, 2017). While estimates of global change in P_{pre} will continue to be refined as new data become available, the observation-based estimates of $P_{pre,AOU}$ presented here are fully consistent with the observed magnitude of Glacial-Interglacial CO_2 change. Further understanding on air-sea disequilibrium of carbon and oxygen on these interglacial-glacial time-scales, as well as the mechanisms driving these glacial changes, is necessary to fully account for the processes important in the estimates of $P_{pre,AOU}$, $\delta^{13}C_{pre,AOU}$, and pCO_2. Nonetheless, our preliminary observation-based estimates of $P_{pre,AOU}$ and $\delta^{13}C_{pre,AOU}$ indicate that an increase of the biological pump efficiency in regions of deep water formation explains the lower glacial CO_2.

CHAPTER 2. DECREASE OF DEEP OCEAN OXYGEN AND PHOSPHATE IN THE SOUTH PACIFIC DURING THE LAST GLACIAL MAXIMUM

2.1 Introduction

During the Pleistocene, Earth's climate shifted quasi-periodically between intervals of extensive Northern Hemisphere continental ice sheet coverage and warmer periods of reduced glaciation. Atmospheric CO_2 variations have aligned with glacial cycles—recorded CO_2 is much lower during glacial periods than during interglacial periods (EPICA community members, 2004). The last glacial maximum (LGM), the most recent time during the previous glacial when ice sheets were at their greatest extent, occurred around 18,000 to 22,000 years ago. During the LGM, atmospheric pCO_2 was about 80 to 100 p.p.m.v. lower than pre-industrial levels (EPICA community members, 2004). There have been several mechanisms that have been proposed that could be responsible for the glacial reduction of atmospheric carbon dioxide; however, most agree that an increased concentration of carbon in the deep-ocean is required (Khatiwala et al., 2019; Sigman et al., 2010).

To understand changes in deep ocean carbon storage during the LGM, a crucial factor lies in comprehending the mechanisms of deep ocean circulation. Deep ocean circulation, coupled with biological processes, governs the dispersion of CO_2, O_2, and nutrients across the ocean interior. The circulation of the Southern Ocean interlinks various ocean basins and bridges the upper and deep layers of the ocean. Consequently, this region exerts a significant impact on the global oceanic circulation and nutrient pattern within the deep ocean.

Carbon is sequestered in the deep ocean through the biological pump. The biological pump is the process where organic matter is produced in the surface layer of the ocean and sinks, where it is later remineralized at depth. The efficiency of the biological pump relies on two factors: the amount of organic carbon sinking to the deep ocean (surface nutrient utilization) and the ability to keep the recycle carbon stored there. The efficiency of the biological pump depends on both the downward flux of organic carbon but also on the retention of remineralized carbon in the deep ocean. The levels of oxygenation and phosphate in the deep ocean can provide context to how efficient the biological pump was in the past. Lower oxygenation and/or higher phosphate levels is potentially indicative of more deep-ocean carbon storage.

Most oxygen proxies, such as laminations, foraminifera assemblages, trace metals, and $\delta^{15}N$ of shell-bound organic matter of planktonic foraminifera have been qualitative in nature (Jaccard & Galbraith, 2012). In the upper 1.5 km of the ocean, most oxygen proxies, record higher oxygenation during the LGM than during the early Holocene (Jaccard & Galbraith, 2012). Lower temperatures during the LGM raises the oxygen solubility and corresponds to this higher oxygenation in shallow and intermediate waters. Contrastingly, in the deep ocean (>2 km), proxies record lower oxygen concentrations (Jaccard & Galbraith, 2012). The deep ocean also experienced cooling during the LGM. However, deep ocean oxygen consumption overcompensates the increase oxygen solubility due to cooler temperatures, corresponding to a decrease in oxygenation.

There have been a variety of semi-quantitative and quantitative oxygen proxies that has been introduced: foraminiferal assemblages, I/Ca in benthic foraminifera, pore area of epifaunal foraminifera, organic matter preservation, and the carbon isotope offset between benthic foraminifera *Cibicoides wuellerstorfi* and *Globobululimina spp*. (known as $\Delta\delta^{13}C$).

Benthic foraminiferal species abundances and size are sensitive to dissolved oxygen concentrations due to gas-exchange morphological adaptations (Corliss, 1985). Foraminiferal species assemblages can therefore be used to infer the ambient dissolved oxygen levels. Kaiho, 1994 related benthic foraminiferal taxa and size to BWO via a benthic foraminiferal dissolved-oxygen index, though this index was not supported well by calibration with living foraminifera (Jorissen et al., 2007). Further region-specific and global calibrations of benthic assemblages (Erdem et al., 2020; Ohkushi et al., 2013; Tetard et al., 2017, 2021) and abundances of *Eubuliminella tenuata* (Tetard et al., 2021) have been published as quantitative BWO proxies sensitive to concentrations below ~100 μmol/kg. From the LGM to the EH, assemblages record lower oxygen conditions in shallow to intermediate waters and higher oxygenation in deep waters globally (Jaccard & Galbraith, 2012).

Lower foraminiferal I/Ca indicates oxygen-depleted conditions (Lu, Rickaby, et al., 2020). Low BWO concentrations are well correlated with I/Ca in living benthic foraminifera (Glock et al., 2014). Lu et al., 2020 posit that low I/Ca (e.g., <3µmol/mol) alongside other (semi-)quantitative proxy indications of low BWO (e.g., pore density>15%) may indicate BWO<~50µmol/kg. The I/Ca records in five cores in the Atlantic and Pacific suggest lower oxygenation of glacial bottom waters (Lu, Rickaby, et al., 2020).

(Rathburn et al., 2018) reported a strong negative logarithmic relationship between BWO concentrations and pore surface area of the epifaunal benthic species *Cibicidoides wuellerstorfi*, demonstrating that pore area can be used as a quantitative reconstruction of past ocean oxygen. Because epifaunal species reflect ambient bottom water conditions, this proxy is spared complications from pore-water conditions that influence proxies that use infaunal species. Additionally, this proxy has the highest resolution in oxygen-poor conditions (Rathburn et al., 2018). Foraminiferal surface porosity has been applied to a downcore record in the Atlantic (Lu et al., 2021). In that record, surface porosity agrees reasonably well with the I/Ca proxy. Lu et al., 2022 reported good agreement among foraminiferal surface porosity, aU, and I/Ca proxies in the Arabian sea for the past ~30 kyr.

Organic matter preservation in marine sediments increases substantively in low BWO environments. If production, dilution, and depth effects remain consistent, order-of-magnitude increases in preserved organic matter can indicate BWO concentrations in the 20-50 μmol/kg range (Anderson et al., 2019). This proxy was applied to two cores in the central equatorial Pacific. There, lower preserved organic matter fluxes suggested low oxygenation during the LGM compared to the Holocene.

Organic matter remineralization releases isotopically light $\delta^{13}C$ into surrounding pore waters, generating a $\delta^{13}C$ gradient between pore water at the anoxic boundary ($O_2 = 0$) and the overlying bottom water. Greater remineralization, associated with higher BWO concentrations, enhances the $\delta^{13}C$ gradient. This difference between bottom water and anoxic boundary $\delta^{13}C$, "$\Delta\ \delta^{13}C$," is mainly a function of BWO concentration, as it closely follows the stoichiometrically modeled relationship between carbon isotope composition and oxygen concentration (McCorkle & Emerson, 1988) .This relationship can be leveraged to reconstruct past BWO by using the $\delta^{13}C$ difference between epifaunal and deep infaunal species—foraminifera that each record the $\delta^{13}C$ of bottom water and anoxic pore water (McCorkle et al., 1990) .The $\delta^{13}C$ of deep infaunal *Globobulimina* reflect the $\delta^{13}C$ of low-oxygen pore waters well (McCorkle et al., 1990). The epifaunal *Cibicidoides wuellerstorfi* is often used to proxy bottom water $\delta^{13}C$ (Mackensen 2008). Therefore, the $\delta^{13}C$ gradient between *Globobulimina spp*. and *C. wuellerstorfi* represents $\Delta\delta^{13}C$. Hoogakker et al., 2015 combined existing data from Mackensen & Licari, 2003; Schmiedl & Mackensen, 2006 with new reconstructions and determined that the $\Delta\delta^{13}C$ values of epifaunal *C. wuellerstorfi* and deep infaunal *Globobulimina spp.* species from six locations in the Atlantic, Indian, and Pacific Oceans. They demonstrated a linear correlation between $\Delta\delta^{13}C$ values of *C. wuellerstorfi* and *Globobulimina spp*. with bottom water oxygen concentrations within the range of 50 to 235 μmol/kg (equation 3) with an R^2 of 0.92. Because of the $\Delta\delta^{13}C$ proxies' ability to reconstruct oxygen over a large range of values, this proxy is used to reconstructed oxygen and preformed phosphate in the past.

Similarly, to oxygen, reconstruction of phosphate in the past can help bring insight on the changes to ocean circulation and/or surface productivity. Since the distribution of Cd in seawater follows that of phosphate, it has been show that we can reconstruct phosphate in the past by using the Cd/Ca measurements on benthic foraminifera (Boyle, 1988, p. 19888; Boyle et al., 1995; Boyle & Keigwin, 1987).

Because oxygen and phosphate are non-conservative in nature, preformed phosphate can help us better understand the changes in the biological pump efficiency for each different water mass. There is a relationship between atmospheric pCO_2 and the global preformed phosphate, with a predictable relationship of as ΔpCO_2^{atm} (ppm) ~ 121 $\Delta PO_{4,pre}$ (μM) (Ito et al., 2004). $\Delta PO_{4,pre}$ is the global change in preformed phosphate. Preformed phosphate is the phosphate that is present in surface of the ocean before subduction. Preformed phosphate can be reconstructed using the reconstruction of phosphate, oxygen, and temperature in the past (Vollmer et al. 2022).

Here, we first present an updated calibration to the $\Delta\delta^{13}C$ paleo-oxygen proxy. Using this updated calibration, we evaluate the oxygen gradient between the deep South Indo-Pacific and Eastern Equatorial Pacific through oxygen reconstruction at 10 cores sites in the Eastern Equatorial Pacific and 8 cores sites in the South Indo-Pacific. Additionally, we combined the reconstructed oxygen gradient with phosphate reconstructions from previously published Cd_{sw} records derived from Cd/Ca in benthic foraminifera to determine changes in ocean circulation and ocean productivity in the past. Lastly, we re-evaluated the global change in preformed phosphate reconstructions to determine the amount of pCO_2 drawdown due to an increase in deep ocean carbon storage through an increase in the biological pump efficiency.

2.1.1 Oceanographic Setting and Core Locations

We present new oxygen and preformed phosphate reconstructions from 8 core-sites in the South Indo-Pacific off the southern coast of Australia from water depths 506 meters and 2525 meters during the Last Glacial Maximum and late Holocene (Figure 15). All cores either sample the Subantarctic Mode Waters (SAMW), the Antarctic Intermediate Waters (AAIW), or the Circumpolar Deep Waters (CDW).

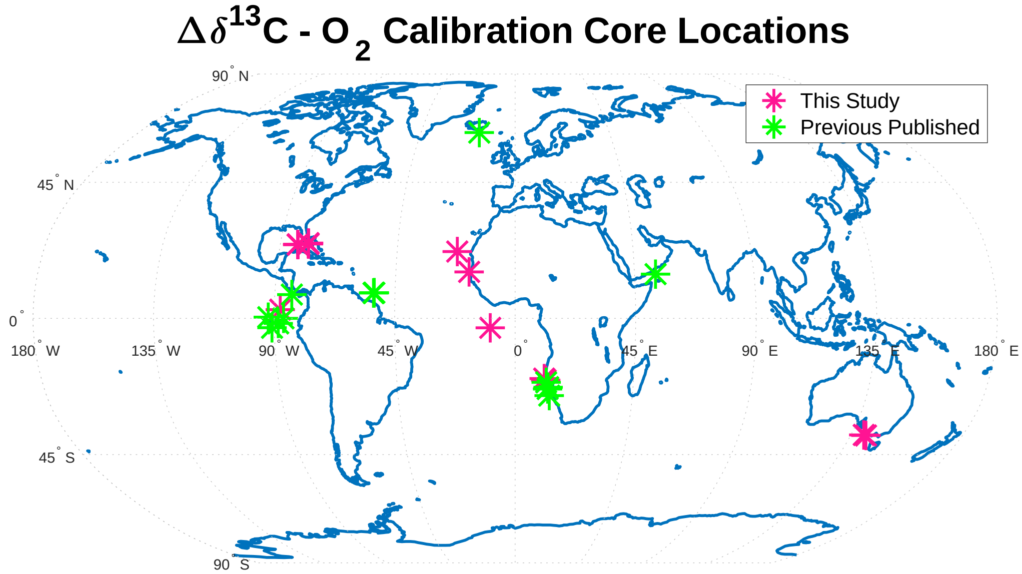

Figure 15 - Location of the 31 cores for the updated $\Delta\delta^{13}C$ – O2 calibration. 17 cores shown in pink are from this study. 14 cores shown in green are from previously published results. See Table 5 more information.

Two cores, RS67-GC27 (depth = 506 meters) and RS78-GC18 (depth = 814 meters), are bathed by SAMW. Subantarctic mode water (SAMW) forms in the Subantarctic Zone of the Southern Ocean via wintertime mixing, which is located between approximately 40 deg S and the Subantarctic Front. As waters flow northward form the Subantarctic front, these low-salinity waters cool and form a sublayer of colder and denser water. Due to cooler temperatures and relatively higher surface nutrient utilization, SAMW are characterized of having high levels of oxygen (200 – 300 μmol/kg) and relatively low levels of preformed phosphate (~0.7 μmol/kg).

Two cores are bathed by AAIW: SO36-7 (depth = 1225 meters) and RS67-GC5 (depth = 1145 meters). Antarctic Intermediate Water (AAIW) is a water mass that is formed within the Antarctic Polar Front zone, located between approximately 50 deg S and 60 deg S. AAIW is formed through Ekman Transport, which pushes surfaces waters northward away from Antarctica, leading to the upwelling of nutrient-rich deep waters. These newly upwelled waters are transported northward, where they decrease in salinity due to input from meltwater and precipitation and down well when it reaches the relatively warmer subantarctic waters. AAIW is generally well-oxygenated, with relatively high dissolved oxygen concentrations compared to the deeper water masses, but slightly lower oxygenation than subantarctic mode waters. Additionally, AAIW is known to be relatively nutrient-rich water mass due to its' high preformed nutrient signature (~1.2 μmol/kg). The relatively large, preformed phosphate is due to the iron and light limited of the Antarctic surface waters (De Baar et al., 2005; Martin, 1990; Martin et al., 1990).

Four cores are represented by CDW: RS67-GC3 (1476 meters), RS67-G16 (1650 meters), V18-222 (1900 meters), and RS67-GC13 (2525 meters). Circumpolar deep water is represented by the mixing of several water masses, including Antarctic Bottom Water (AABW), AAIW, North Atlantic Deep Water (NADW), and recirculated CDW. It is characterized as being relatively warm, salty, and nutrient-rich water mass. Circumpolar deep water is found at depths beneath the AAIW (~1200 meters). Circumpolar deep water is characterized as relatively low oxygenation (~175 μmol/kg) and high preformed phosphate (~1.4 μmol/kg). Similarly, to the AAIW, the large, preformed phosphate is due to the iron and light limited of the Antarctic surface waters which fuels the Antarctic Bottom Waters, which has a preformed phosphate signature of 2.0 μmol/kg and prevents the drawdown of surface nutrients (De Baar et al., 2005; Martin, 1990; Martin et al., 1990).

Additionally, we present new oxygen and preformed phosphate reconstructions from 7 core-sites in the Eastern Equatorial Pacific (EEP) from water depths 617 meters and 2867 meters during the Last Glacial Maximum and late Holocene (Figure 15). As SAMW, AAIW, and CDW move through the ocean interior, upon reaching the EEP, oxygen levels decrease, and phosphate levels increase due to organic matter remineralization. This corresponds to a general increase in phosphate at all depths and a decrease in oxygen at all depths for the EEP. However, the preformed phosphate depth profile looks similar for both the South Indo-Pacific depth profile and the EEP depth profile due to the water being sourced from the same region. By the time these water masses reach the EEP, mixing between the water masses has occurred. The cores from the EEP <1500 meters, represent a mixture between SAMW, AAIW, and North Pacific Intermediate Waters. The cores from the EEP greater than 1500 meters represent CDW.

2.2 Methods

2.2.1 Updated $\Delta\delta^{13}C$ – Paleo oxygen Calibration

We expanded the relatively new paleo-oxygen proxy, $\Delta\delta^{13}C$, from 6 core-sites to 31 core-sites, ranging from depths = 366 – 3202 meters and found in the Atlantic, Pacific, and Indian ocean (Figure 15).

This expansion includes 6 cores from the Hoogakker et al., 2015 calibration, 8 recently published oxygen $\Delta\delta^{13}C\text{-}O_2$ reconstructions from Hoogakker et al., 2018; Jacobel et al., 2020; Lu et al., 2023; Umling et al., 2018, and 17 new late Holocene $\Delta\delta^{13}C\text{-}O_2$ reconstructions from this study, corresponding to depths 192 to 3202 meters and found in the Atlantic, Pacific, and Indian oceans. For the new $\Delta\delta^{13}C\text{-}O_2$ reconstructions, carbon and oxygen isotopes were performed on the benthic foraminifera *Globobulimina spp.*, *Cibicoides wuellerstorfi*, and *Planulina ariminensis* for the Late Holocene (6 ka – 0 ka). Similarly, to *C. wuellerstorfi*, $\delta^{13}C$ *P. ariminensis* also represent bottom-water $\delta^{13}C$ values. $\delta^{18}O$ and $\delta^{13}C$ measurements were performed using a Thermo MAT253 Stable Isotope Mass Spectrometer coupled to a Kiel IV Carbonate Device at the Georgia Institute of Technology. *Globobulimina spp., P. ariminensis, and C. wuellerstorfi* were picked from the >250 μM size fraction and measured individually. $\delta^{18}O$ and $\delta^{13}C$ measurements were converted to PDB using an in-house standard, NBS-18, and NBS-19. The in-house standard demonstrated a reproducibility of less than 0.1‰ for $\delta^{18}O$ and less than 0.05‰ for $\delta^{13}C$ (1-sigma). When *P. ariminensis, and C. wuellerstorfi* were not found, previously published values were used (Lynch-Stieglitz et al., 1994, 2006).

2.2.2 *Reconstruction of Bottom Water Oxygen*

Late Holocene and LGM oxygen reconstructions were performed using the updated $\Delta\delta^{13}C$-O_2 (equation 7) for 18 cores in the South Indo-Pacific and Eastern Equatorial Pacific ranging from depths 506 meters to 2867 meters (Figure 15 - Location of the 31 cores for the updated $\Delta\delta^{13}C$ – O2 calibration. 17 cores shown in pink are from this study. 14 cores shown in green are from previously published results. See Table 5 more information.). $\Delta\delta^{13}C$ measurements for the ten cores in the Eastern Equatorial Pacific are from Kim et al., 2023. Carbon and oxygen isotopes were analyzed on the benthic foraminifera *Globobulimina spp.* for both the Late Holocene and LGM section of the cores. $\delta^{18}O$ and $\delta^{13}C$ measurements were conducted using a Thermo MAT253 Stable Isotope Mass Spectrometer coupled to a Kiel IV Carbonate Device at the Georgia Institute of Technology. *Globobulimina spp.* and *C. wuellerstorfi* from the >250 μM size fraction were individually measured. $\delta^{18}O$ and $\delta^{13}C$ measurements were converted to PDB using an in-house standard, NBS-18, and NBS-19. The in-house standard demonstrated a reproducibility of less than 0.1‰ for $\delta^{18}O$ and less than 0.05‰ for $\delta^{13}C$ (1-sigma). For the South Indo-Pacific cores, we used previously published carbon isotopes from Lynch-Stieglitz et al., 1994. Using the $\delta^{18}O$ of benthic foraminifera, Lynch-Stieglitz et al., 1994 determined the corresponding core depths for the LGM and late Holocene time slices. Similarly, for the Eastern Equatorial Pacific cores, the LGM and late

Holocene section of the cores were determined using Radiocarbon ages on planktonic foraminifera (Koutavas & Lynch-Stieglitz, 2003). Three of the $\Delta\delta^{13}C$ measurements come from previously published work (Hoogakker et al., 2018; Jacobel et al., 2020). The oxygen reconstruction was updated using the new calibration (Equation 7).

2.2.3 Reconstruction of Bottom Water Phosphate

We derive estimates of phosphate concentration (P) by employing previously established published estimates of seawater cadmium levels (Cd_w). The computation of P is executed through a nonlinear relationship established between the Cd_w reconstructed from foraminifera in the core top and the phosphate levels in the overlying seawater from Boyle, 1988, 1992; Boyle et al., 1995 (Figure 1) (Elderfield and Rickaby 2000).

Cd_w reconstructions for the south Indo-Pacific are from Lynch-Stieglitz et al., 1996. Cd_w reconstructions for the Eastern Equatorial Pacific are from Umling et al., 2018. The Cd_w reconstructions are summarized in Table 8.

2.2.4 Reconstruction of Bottom Water Preformed Phosphate

Reconstructions of bottom-water $P_{pre,AOU}$ were performed at all core sites in the South Indo-Pacific and Eastern Equatorial Pacific cores, where there are phosphate reconstructions.

We can estimate preformed phosphate as a function of phosphate (P), oxygen (O_2), temperature (T), salinity (S) (Equation 1), and assuming a P:O_2 stoichiometric ratio of 1:170±10 (Anderson & Sarmiento, 1994).

Estimation of preformed phosphate relies on the oxygen deficit relative to saturation, termed as AOU. As a result of factors like heat loss, sea-ice cover, and the mixing of subsurface waters, surface water oxygen levels are often below saturation during the formation of water masses. This condition has the potential to lead to an overestimation of oxygen loss through respiration (Ito et al., 2004). Since changes in the air-sea disequilibrium on glacial-interglacial timescales are unknown, we defined the notation, $P_{pre,AOU}$, indicating the AOU-based estimate of preformed phosphate and distinguish it from the true P_{pre} (Vollmer et al. 2022).

Oxygen saturation weakly depends on salinity. Here, we approximate salinity change using the global mean salinity increase of 1 g/kg during the LGM (Adkins, 2002). An increase salinity of 1 g/kg causes a decrease of $O_{2,sat}$ of 2-3 μmol/kg. Similarly, temperature changes in the intermediate and deep ocean are relatively small (< 5 deg C) since the LGM (Bereiter et al., 2018). When temperature reconstructions in proximity were unavailable, we attributed a range of credible values (0 – 5 deg C) for the computations and error assessments.

2.3 Results and Discussion

2.3.1 *Updated $\Delta\delta^{13}C$ – Paleo oxygen Calibration*

We demonstrated a linear correlation between $\Delta\delta^{13}C$ values of *C. wuellerstorfi* or *P. ariminensis* and *Globobulimina spp*. with bottom water oxygen concentrations within the range of 103 to 293 µmol/kg (equation 7, Figure 16, Table 5, Table 6, Table 7) with an R^2 of 0.64 and a standard error of 30 µmol/kg (1- sigma).

$$O_2^{bot}[\mu M] = (\Delta\delta^{13}C - 0.44)/0.008 \tag{7}$$

The $\Delta\delta^{13}C$ – O_2 calibration from Hoogakker et al., 2015 found that in oxygenated conditions greater than 235 µmol/kg, there was no relationship between $\Delta\delta^{13}C$ and O_2. However, this data was from pore and bottom water $\delta^{13}C$ estimates and not $\delta^{13}C$ from *C. wuellerstorfi* and *Globobulimina spp.* There could have been a potential error for determining the $\delta^{13}C$ at the anoxic boundary within the sediment. This is why we determined a calibration using only benthic foraminifera and no pore or bottom $\delta^{13}C$ data.

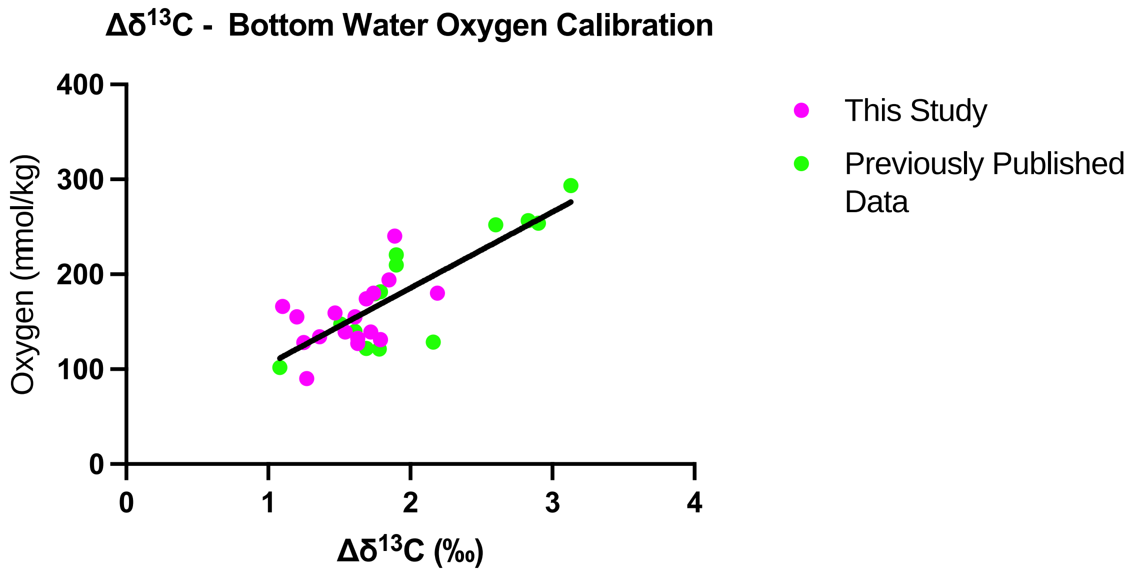

Figure 16 - Relationship between Δδ^{13}C (the difference in δ^{13}C between *C. wuellerstorfi/P. ariminensis* and *Globobulimina spp.*) and bottom-water oxygen estimated from WOA13 (Boyer et al., 2013). The study includes previously published data, shown in green, Hoogakker et al., 2015, 2018; Jacobel et al., 2020; Lu et al., 2023; Mackensen & Licari, 2003; McKay et al., 2016; Schmiedl & Mackensen, 2006; Umling et al., 2018. New data from this study is shown in pink. Results are summarized in Table 5.

The new calibration shown in Figure 16 has a larger error than the calibration found in Hoogakker et al., 2015. This could be due to a lack of *Globobulimina spp.* and *C. wuellerstorfi* measurements at some core locations or the incorporation of isotopically light δ^{13}C in *Globobulimina spp*. There were six cores that only had either one *C. wuellerstorfi*/*P. ariminensis* or one *Globobulimina spp.* that was used to determine the Δδ^{13}C at that core site. Additionally, the maximum Δδ^{13}C standard error (1-sigma) found for any core site was 0.25 ‰ (Table 5). This corresponds to an oxygen error of 20 μmol/kg (1-sigma). This highlights the importance of having multiple (>5) measurements for both

C. wuellerstorfi/P. ariminensis and *Globobulimina spp*. Additionally, there could be an incorporation of isotopically light $\delta^{13}C$ in *Globobulimina spp.* through sulfate reduction or *Globobulimina spp.* denitrifying (Jacobel et al., 2020; McCorkle & Emerson, 1988). If there are specific regions where sulfate reduction or *Globobulimina spp.* denitrifying, this will artificially inflate any oxygen reconstructions. However, there is not any significant basin specific or depth specific differences in our calibration. This suggests that an expansion of the calibration is needed to better understand regions where this proxy could potentially not work.

2.3.2 Glacial-Interglacial Changes in Oxygenation

In general, there is an increase in oxygenation at shallow/intermediate depths (<1000 meters) and a decrease in oxygenation for deep depths (>1500 meters) during the LGM compared to modern (Figure 17). Jaccard & Galbraith, 2012 compiled qualitative changes in oxygenation from the LGM and Holocene, revealing similar findings. The increase in oxygenation for shallow/intermediate depths is partly due to an increase in oxygen solubility due to ocean waters being cooler during the LGM (Bereiter et al., 2018). A decrease of ocean temperatures by 0 - 5 degrees Celsius would lead in an increase in oxygen saturation by of up to 40 μmol/kg. This increase of oxygen saturation can explain a significant amount of oxygen increase observed at the shallow/intermediate depths sites. The decrease in oxygenation for deep depths is most likely due to an increase in deep ocean carbon storage through an increase in the biological pump efficiency. This is further explored in sections 2.3.2.1 and 2.3.2.2.

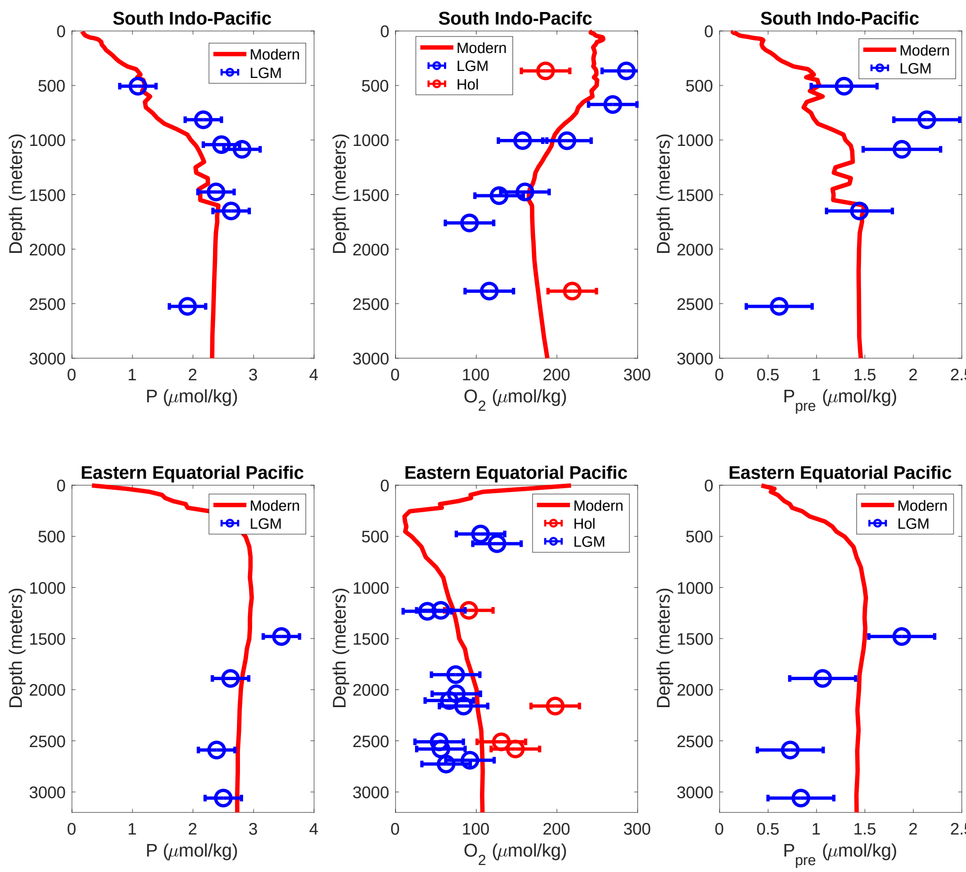

Figure 17 - Phosphate (left), oxygen (middle), and preformed phosphate (right) reconstructions for the south Indo-Pacific (top) and Eastern Equatorial Pacific (bottom) (cores summarized in Table 6, Table 7, Table 8). The preformed phosphate estimates for the eastern equatorial pacific cores use a depth-weighted linear interpolation of nearby oxygen reconstructions. The LGM reconstructions are shown in blue. The late Holocene reconstructions are shown in red. The modern climatology from WOA13 is shown in black (Boyer et al., 2013).

2.3.2.1 South Indo-Pacific Oxygen Reconstructions

Since most of the cores lacked paired *C. wuellerstorfi* and *Globobulimina spp.*, only two late Holocene reconstructions were performed. Overall, these late Holocene reconstructions agree with climatology (WOA13) within 2-sigma error (Figure 17).

LGM oxygen reconstructions show higher oxygenation compared to modern in cores located in SAMW, most likely due to an increase in oxygen saturation (Figure 17). There are currently no temperature estimates for the SAMW during the LGM. However, the deeper AAIW likely cooled by about 3 degrees Celsius (Elmore et al., 2015). A cooling of 3 degrees Celsius leads to an increase of oxygen saturation of 25 μmol/kg. This is similar to the observed increase in oxygenation of ~40 μmol/kg. However, LGM oxygen reconstructions show lower oxygenation compared to modern in cores located in AAIW and CDW (Figure 17). Kohfeld et al., 2005, compiled productivity changes from the last glacial maximum to present using fluxes of specific biogenic components, radionuclides, and from degradation productions and found an increase in productivity near our South Indo-Pacific core sites. Authigenic Uranium (aU) reconstructions were performed nearby at intermediate depths (800 to 1500 meters) and saw an increase in aU (Durand et al., 2018). This increase in aU indicates a decrease in oxygenation during the LGM for AAIW, in agreement with our findings. One explanation for the decreases in oxygenation for our cores located in CDW and AAIW are most likely due to an increase in the biological pump efficiency. This is further explored in section .3.3. This is in agreement with other deep ocean oxygen reconstructions (Gottschalk, Skinner, et al., 2016; Hoogakker et al., 2018; Jacobel et al., 2020; Umling et al., 2018).

2.3.2.2 Eastern Equatorial Pacific Oxygen Reconstructions

Due to the lack of a *C. wuellerstorfi* during the late Holocene, late Holocene oxygen reconstructions were performed at one core site: V19-28 (depth = 2720 meters) (Kim et al., 2023). Most Late Holocene oxygen reconstructions are in agreement with modern climatology (within 2-sigma standard error), except for ODP-1242 (Jacobel et al., 2020). Disagreement between the Late Holocene reconstructions and climatology could be because *G. affinis* has the potential to live beneath the anoxic boundary within the sediment. This could allow G. *affinis* to incorporate isotopically light $\delta^{13}C$ through anaerobic processes, such as sulfate reduction (Jacobel et al., 2020; McCorkle & Emerson, 1988). More isotopically light $\delta^{13}C$ will artificially inflate $\Delta\delta^{13}C$, causing an overestimation of oxygen.

Overall, we observe a decrease in oxygenation during the Last Glacial Maximum in deep waters (>1500 meters), in agreement with qualitative and quantitative oxygen proxies in the region (Figure 17) (Bradtmiller et al., 2010; Hoogakker et al., 2018; Jacobel et al., 2020). Additionally, we observe a strong increase in oxygenation during the Last Glacial Maximum in intermediate waters (<1000 meters) (Figure 17). This is in agreement with qualitative oxygen reconstructions from nitrogen isotopes in the region (Dubois et al., 2011; Robinson et al., 2009). Similarly, aU reconstructions in the EEP also show a qualitative decrease in oxygenation in deep waters (Bradtmiller et al., 2010).

2.3.3 Glacial-Interglacial Changes in Preformed Phosphate and Implications to Atmospheric CO_2 drawdown

The preformed phosphate reconstructions show an increase in intermediate (<1500 meters) core sites for both the Eastern Equatorial Pacific and the south Indo-Pacific during the LGM compared to modern (Figure 17, Table 9). The preformed phosphate in intermediate core sites for both the Eastern Equatorial Pacific and the south Indo-Pacific agree. This means that the biological pump efficiency was reduced during the LGM for the Subantarctic mode water and Antarctic intermediate waters, where these cores are sourced from. Productivity reconstructions in the subantarctic zone, where the subantarctic mode waters and Antarctic intermediate waters are formed show an increase in productivity (Kohfeld et al., 2013). This should reduce the preformed phosphate of these water masses. However, if the supply of nutrients to this region increased to a greater extent than the amount of productivity increased, this would cause an increase of the preformed phosphate signature. An increase of supply of nutrients to the surface can be due to enhanced Southern Ocean westerlies and corresponding upwelling during the LGM (e.g., Chen & Wang, 2021).

The preformed phosphate reconstructions show a strong decrease in deep waters (>2500 meters) core sites for both the EEP and south Indo-Pacific. This means that the biological pump efficiency was increased during the LGM for the Circumpolar Deep waters (CDW). This agrees with other deep water preformed phosphate reconstructions globally (Vollmer et al., 2022).

We can determine atmospheric pCO_2 drawdown due to an increase in the biological pump efficiency using $P_{pre,AOU}$ reconstructions (Vollmer et al., 2022). There is a theoretical relationship between atmospheric pCO_2 and preformed phosphate of 121 ppm:1 μmol/kg (Ito and Follows 2004). Vollmer et al., 2022 found that changes in the deep Indo-Pacific $P_{pre,AOU}$ is similar to changes in global $P_{pre,AOU}$. Using the deep (>2000 meters) Indo-Pacific $P_{pre,AOU}$ reconstructions in this study, we find an average decrease of $P_{pre,AOU}$ of 0.63 ± 0.24 μmol/kg (2-sigma) during the LGM with respect to modern. This corresponds to a pCO_2 drawdown of 76 ± 29 ppm (2-sigma), corresponding to the majority of the observed atmospheric pCO_2 drawdown. This is similar to the pCO_2 drawdown of 64 ± 29 ppm (2-sigma) determined in Chapter 1 using the average preformed phosphate change from 3 deep cores in the South-Indo Pacific.

2.3.4 Implications for South Pacific Circulation and Productivity during the LGM

Compared to modern, the gradient for AOU and P between the deep South Indo-Pacific and deep EEP, and the South Indo-Pacific and deep Arabian Sea, had relatively little change (Figure 18). AOU and P estimates for the EEP and south Indo-Pacific were determined by taking an average of all core-sites (>2000 meters) in that region. AOU and P estimates for the Arabian Sea were determined by taking an average of all core-sites

(>2000 meters) in that region (Boyle et al., 1995; Lu et al., 2023). The modern AOU and P gradient between the deep South Indo-Pacific and deep EEP is 63 ± 42 μmol/kg and 0.63 ± 0.4 μmol/kg, respectively. The reconstructed LGM AOU and P gradient between the deep South Indo-Pacific and deep EEP is 53 ± 42 μmol/kg and 0.51 ± 0.4 μmol/kg. Additionally, the modern AOU and P gradient between the deep South Indo-Pacific and deep Arabian Sea is 49 ± 42 μmol/kg and 0.37 ± 0.4 μmol/kg, respectively. The reconstructed LGM AOU and P gradient between the deep South Indo-Pacific and deep Arabian Sea is 44 ± 42 μmol/kg and 0.42 ± 0.4 μmol/kg .

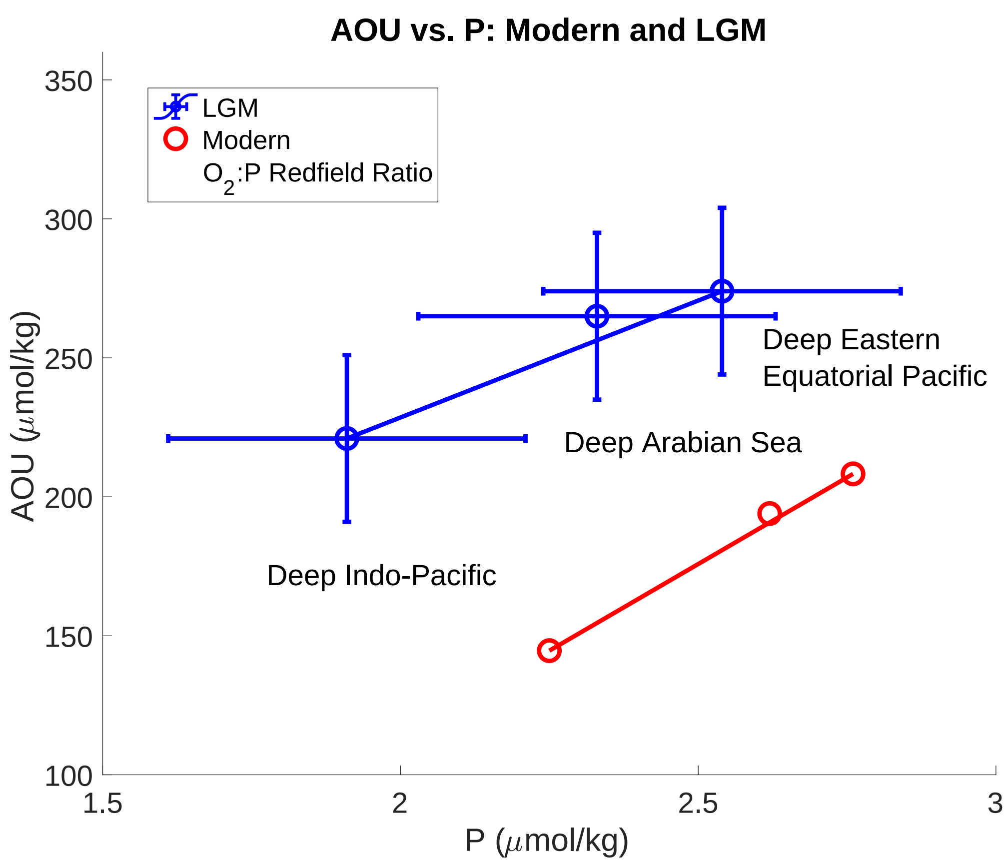

Figure 18 - Relationship between Apparent Oxygen Utilization (AOU) and Phosphate (P) for the deep south Indo-Pacific, the deep Arabian Sea, and the Deep Eastern Equatorial Pacific (EEP). AOU and P reconstructions for the deep south Indo-Pacific and deep EEP are from an average of cores >2000 meters from this study. AOU and P reconstructions (cores > 2000 meters) for the deep Arabian Sea are from Boyle, 1992; Lu et al., 2023. Error bars are the 1-sigma calibration error for both AOU and P. LGM reconstructions are shown in blue. Modern estimates from WOA13 are shown in red (Boyer et al., 2013). The Redfield ratio between Oxygen and Phosphate of 170:1 is shown in gray.

There are three potential mechanisms for changes in oxygenation and phosphate during the LGM in the deep Indo-Pacific: (1) changes in overall pattern of export productivity, (2) changes in ocean circulation, or (3) changes in the preformed component of oxygen or phosphate. If there was an increase in productivity within the South Pacific along the circulation route, there would be an increase in the gradient of AOU and P. Our reconstructions do not show this (Figure 18). If there was a change in the source of deep-water formation (i.e. pacific deep water formation), the AOU and P reconstructions would not follow the P:O_2 Redfield ratio of 1:170. Some studies show evidence of deep-water formation during the LGM in the North Pacific (e.g. Okazaki et al. 2010, Rae et al. 2014, Yu et al. 2020). However, our reconstructions do not show a high oxygen source of deep water during the LGM (Figure 18). If there was a slowdown in deep-sea overturning circulation, there would be an increase in ventilation ages along the circulation route and an increase in the gradient of AOU and P. Our reconstructions do not support this (Figure 18). However, if there was a change in the preformed component of oxygen or phosphate, the phosphate and oxygen content where the deep-water formed (i.e. Southern Ocean), there would be no change in the oxygen or phosphate gradient. This is a possible scenario based on our reconstructions (Figure 18).

Overall, the patterns of productivity along the pathway of deep water in the South Indo-Pacific are uncertain. There are no clear signals of productivity changes in the western Arabian Sea or Eastern Equatorial Pacific during the Last Glacial Maximum. Productivity reconstructions show a reduction in the Western Arabian Sea during the Last glacial period (Anderson & Prell, 1993; Gupta et al., 2011; Ivanochko et al., 2005; Jung et al., 2002; Naidu & Malmgren, 1996; Singh et al., 2011). However, primary productivity estimates during the Last Glacial using percent of *F. profunda* show an increase in productivity (Zhou et al., 2022). Kohfeld et al., 2013 found increased export production in the subantarctic zone and decreased export production in the Antarctic zone. Kohfeld et al., 2013 found mixed signals on productivity changes in the EEP during the LGM. Authigenic uranium paired with oxygenation reconstruction show a lower export production during the LGM in the Eastern Equatorial Pacific (Umling et al., 2018). Additionally, $^{231}Pa/^{230}Th$ show a reduction in productivity during the LGM (Costa et al., 2017).

There were older ventilation ages in the deep Indian and Pacific Ocean during the LGM (Rafter et al., 2022). This allows for more accumulation of nutrients and oxygen utilization, causing an increase in the AOU and phosphate gradient. However, the difference between the ventilation age of the S.O. at 40 degrees south where our deep Indo-Pacific oxygen and phosphate reconstructions are and the EEP had little change during the

LGM with respect to the modern (Rafter et al., 2022). This would cause little change in the AOU and P gradient.

Overall, our oxygen and phosphate reconstructions coupled with no conclusive evidence on surface productivity changes along the route of circulation and no significant change in the difference of ventilation age between the South Indo-Pacific and Eastern Equatorial Pacific cores points to no significant changes in ocean circulation or productivity in the South Indo-Pacific, excluding the Southern Ocean. There is no evidence for other sources of other deep water formation sites. The reconstructions reinforce the idea that the Southern Ocean had a pivotal role in reducing atmospheric CO_2, potentially through greater nutrient utilization, resulting in a noticeable decline in oxygen and phosphate levels in the deep South Indo-Pacific and Eastern Equatorial Pacific regions. However, more ventilation age reconstructions and productivity reconstructions are needed to fully understand the dynamics of the South Indo-Pacific.

2.3.5 Implications for Global Deep Ocean Circulation during the LGM

Combining our LGM AOU and P reconstructions from the South Indo-Pacific and Eastern Equatorial Pacific with previous published reconstructions of AOU and P from all ocean basins (Chapter 1), we can investigate changes in the global deep ocean circulation. The phosphate and AOU reconstructions for all core-sites follow the Redfield ratio between O_2 and P, unlike the modern AOU and P configuration, supporting the idea that there was a single origin of deep-water formation with contact to the atmosphere during the LGM in the North Atlantic (Figure 19). In our modern climate state, there are two regions of deep-water formation, the North Atlantic and Southern Ocean. The north Atlantic forms North Atlantic deep water (NADW), where it flows through the interior of the Atlantic Ocean and upwells in the Southern Ocean. The Southern Ocean forms Antarctic Bottom Water (AABW) where it flows in the Pacific Ocean and mixes with NADW and other intermediate waters to form Circumpolar deep water (CDW). During the LGM, sea-ice expanded, potentially creating a lid for the upwelled North Atlantic sourced deep water that prevents outgassing to the atmosphere (Lund et al., 2021; Sigman et al., 2010). If this deep water cannot equilibrate with the atmosphere, it would maintain its high carbon/low oxygen and preformed phosphate characteristics before it forms AABW and CDW. This points towards the North Atlantic as a single source of deep-water origin with contact to the atmosphere during the LGM, where the water flows southward and encounters a sea-ice lid and consequently fills the deep ocean interior. However more oxygen, phosphate, and preformed phosphate reconstructions are needed to better constrain this.

There are two different AOU reconstructions shown in the deep S. Atlantic core, one uses the $\delta^{13}C$ from benthic foraminifera *C. wuellestorfi* and the other from *C. kullenbergi* (Gottschalk et al., 2016a; Gottschalk et al., 2016b). It is thought that *C. wuellerstorfi* better represent bottom-water conditions than *C. kullenbergi* due to its more epifaunal habitat. More reconstructions in the deep South Atlantic can better constrain the AOU and P estimates in this region.

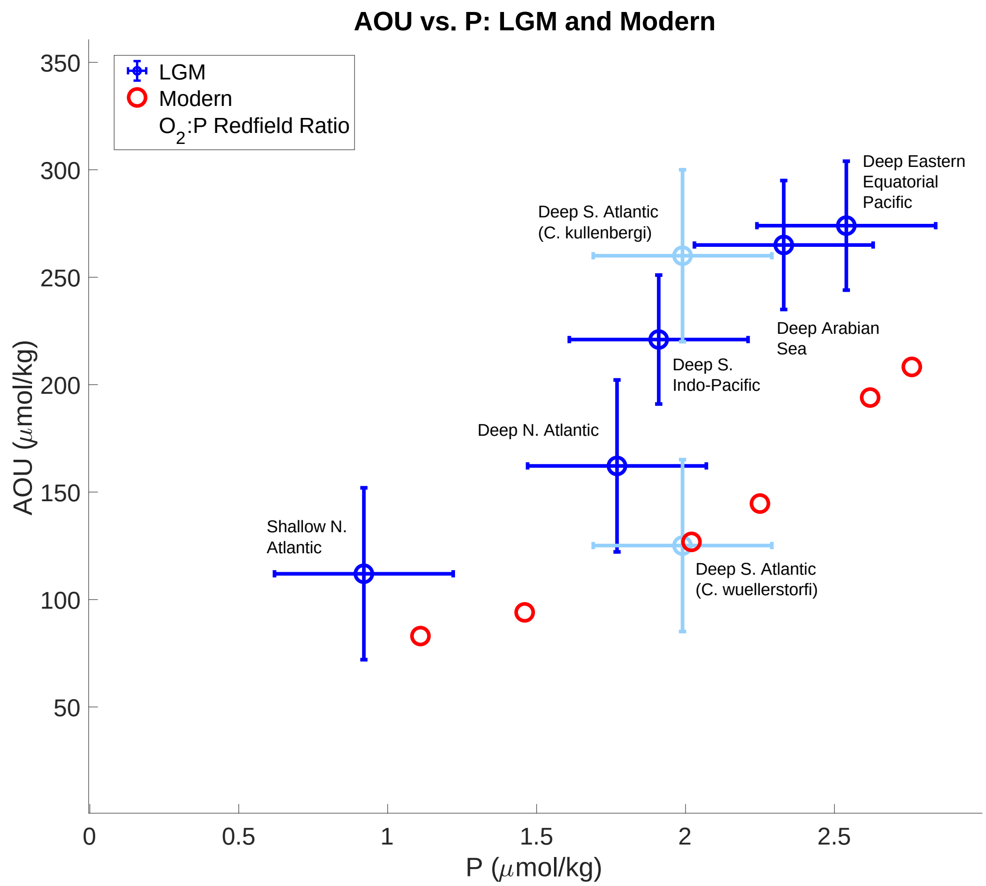

Figure 19 - Relationship between Apparent Oxygen Utilization (AOU) and Phosphate (P). AOU and P reconstructions for the deep south Indo-Pacific and deep EEP are from an average of cores >2000 meters from this study. AOU and P reconstructions for the deep Arabian Sea, deep S. Atlantic, deep N. Atlantic, and shallow N. Atlantic are from Boyle, 1992; Boyle et al., 1995; Gottschalk et al., 2016; Gottschalk et al., 2016; Hoogakker et al., 2015, 2018; Lu et al., 2023; Marchitto & Broecker, 2006; Martin et al., 2005; McKay et al., 2016; Mojtahid et al., 2017; Roberts et al., 2016; Rosenthal et al., 1997; Schmiedl & Mackensen, 2006; Skinner et al., 2003; Umling et al., 2018. AOU and P error bars are the 1-sigma calibration error for both AOU and P. LGM reconstructions are shown in blue. Modern estimates from WOA13 are shown in red (Boyer et al., 2013). The Redfield ratio between Oxygen and Phosphate of 170:1 is shown in gray.

2.4 Conclusions

The deep Indo-Pacific has been thought as a prime region of increased respired carbon storage during the LGM allowing for a reduction of atmospheric CO_2 during the Last Glacial Maximum (Allen et al., 2020; Bradtmiller et al., 2010; Hoogakker et al., 2018; Jacobel et al., 2020; Umling et al., 2018). However, the cause of this increased respired carbon storage is not fully constrained. Here, we updated the $\Delta\delta^{13}C$ paleo-oxygen proxy to 31 cores. Using this updated $\Delta\delta^{13}C$ paleo-oxygen proxy, we present for the first time a LGM O_2, P, and $P_{pre,AOU}$ depth profile in the South Indo-Pacific and Eastern Equatorial Pacific. Our paired phosphate and oxygen reconstructions show little to no changes in the gradient of AOU and P between the deep Eastern Equatorial Pacific and deep South Indo-Pacific, indicating that the observed changes in oxygen and phosphate are most likely caused from changes in the Southern Ocean. Lastly, our deep Indo-Pacific and deep Eastern Equatorial Pacific LGM preformed phosphate reconstructions suggest that the enhanced efficiency of the biological pump in areas where deep water is formed accounts for the majority of the reduced levels of glacial CO_2.

CHAPTER 3. CHANGES IN THE SOUTHEAST ATLANTIC OXYGEN MINIMUM ZONE DURING THE LAST GLACIAL MAXIMUM

3.1 Introduction

Oxygen minimum zones (OMZ) hold critical significance in the study of marine ecosystems and global biogeochemical cycles. These zones are characterized by low levels of dissolved oxygen and play a pivotal role in shaping the distribution and behavior of marine life. Understanding the changes in OMZs is vital for sustainable fisheries management, as they often coincide with regions of high biological activity (Long et al., 2021). Under a warming climate, oxygen minimum zones are predicted to expand (Stramma et al., 2008). Understanding the changes in the OMZs during the Last Glacial Maximum (LGM) will provide insight on how oxygen minimum zones might change in the future.

In the modern ocean, the Southeast Atlantic has an OMZ along the Benguela Current. The Benguela Current is a cold ocean current that courses along the southwestern coast of Africa in the Atlantic Ocean. It is a constituent of the South Atlantic Gyre, which is a combination of ocean currents that rotate around the South Atlantic Ocean (Garzoli & Gordon, 1996). Due to the waters being on the Eastern margin of the ocean basin, they have been out of contact with the atmosphere longer, so they will have more of the original oxygen depleted from the regeneration of organic matter. Additionally, the Benguela Upwelling System is instigated by wind-induced coastal upwelling and offshore Ekman transport. The coastal upwelling results in the upwelling of cold nutrient-laden deep waters to the surface. The upwelling of these deep waters gives rise to the emergence of an oxygen minimum zone. In general, the OMZ in the Benguela Upwelling System is situated from about 100 meters to 600 meters. The Benguela Upwelling System traverse the latitudinal range of 10 deg S to 35 deg S, demarcated by the Angola-Benguela Frontal Zone and Agulhas retroflection (Shannon & Nelson, 1996).

The main water masses of the Benguela Current are: South Atlantic Central Water, Antarctic Intermediate Water (AAIW), and North Atlantic Deep Water (NADW). South Atlantic Central Water is found up to around 600 meters and include a mixture of other central and mode waters (Lamont et al., 2015; Stramma & England, 1999). The OMZ is located within this water mass, with oxygenation values under 50 μmol/kg. AAIW is found to depths around 1000 meters and is characterized by relatively lower temperature and salinity compared to South Atlantic Central Waters, but higher levels of oxygenation (~100 – 150 μmol/kg). It originates in the Southern Ocean and enters the Benguela Current via the Alguhas current system (Stramma & England, 1999). Lastly, the North Atlantic Deep Water originates from the North Atlantic is found at depths below 1000 meters in this region (Stramma & England, 1999). It is characterized by relatively high levels of oxygen, low temperatures, and high salinity.

The LGM occurred around 20,000 years ago when ice sheets were at their greatest extent across Earth's surface in recent history. In this period, atmospheric CO_2 was 80 – 100 ppm lower than pre-industrial levels (EPICA community members, 2004). This lowering of atmospheric CO_2 was accompanied with a decrease in ocean temperatures of about three degrees (Bereiter et al., 2018). There are three ways oxygen concentration can change in the past: (1) changes in oxygen saturation, through changes in ocean temperature and salinity, (2) changes in surface productivity, and/or (3) changes in ocean circulation. Due to ocean temperatures being cooler during the LGM, oxygen saturation is expected to increase, potentially shrinking oxygen minimum zones. However, changes in surface productivity LGM is still debated. Mollenhauer et al., 2002 found using total organic carbon mass accumulation rates enhanced productivity during the LGM along the Benguela Upwelling System. Lu et al., 2020 compiled authigenic Uranium reconsturctions (aU) to investigate changes in productivity. Along the Benguela Upwelling System, aU reconstructions mostly found an increase in productivity during the LGM. Lastly, a more sluggish circulation during the LGM would cause a decrease in oxygenation, due to an increase time for organic matter remineralization. Though there are no reconstructions of the South Atlantic Central Waters strength during the LGM, AMOC strength reconstructions are ambiguous. Some reconstructions shown an a more vigorous circulation (Bradtmiller et al., 2014; Lippold et al., 2012). Other reconstructions show a weakened circulation (Freeman et al., 2016; Skinner et al., 2017).

Jaccard and Galbraith aggregated qualitative LGM oxygen reconstructions, which indicated reduced oxygenation in the deep ocean (>1000 meters) due to heightened carbon storage from respiration, and decreased oxygenation in the shallow/intermediate ocean (<1000 meters) owing to increased oxygen saturation. While there have been two quantitative oxygen reconstructions in the Peruvian and Arabian Sea OMZs, this study represents the first quantitative oxygen reconstruction in the Southeast Atlantic OMZ within the Benguela Upwelling System.

Here, we apply the updated $\Delta\delta^{13}C - O_2$ paleo-oxygen calibration from Chapter 2 to reconstruct oxygen for 3 cores found within or near the Benguela Upwelling System to understand changes in the OMZ during the LGM.

3.2 Material and Methods

3.2.1 Foraminiferal Carbon Isotope Data

The cores used in this analysis were sourced from the Southeast Atlantic (Lynch-Stieglitz et al., 2006). *C. wuellerstorfi* and *P. ariminensis* $\delta^{13}C$ data come from (Lynch-Stieglitz et al., 2006). We supplement this with newly generated carbon isotope data for *Globobulimina spp.* from the Last Glacial Maximum and Late Holocene. We use previously published Holocene and LGM time slices, which were chosen based on the benthic and planktonic isotope stratigraphy (Lynch-Stieglitz et al., 2006). $\delta^{18}O$ and $\delta^{13}C$ measurements were conducted on a Thermo MAT253 Stable Istope Mass Spectrometer coupled to a Kiel IV Carbonate Device at the Georgia Institute of Technology. *Globobulimina spp.* was picked from the >250 uM size fraction and measured individually. $\delta^{18}O$ and $\delta^{13}C$ measurements were converted to PDB using an in-house standard, NBS-18, and NBS-19. Reproducibility of the in-house standard was less than 0.1‰ for $\delta^{18}O$ and less than 0.05‰ for $\delta^{13}C$ (1-sigma). The data is shown in Table 10, Table 11, Table 12.

3.2.2 Reconstruction of Bottom-Water Oxygen

We use the carbon isotope gradient ($\Delta\delta^{13}C$) between epifaunal foraminifera (*Cibicoides wuellerstorfi and Planulina ariminensis*) and deep infaunal benthic foraminifera species (*Globobulimina spp.)* bottom water oxygen calibration to reconstruct oxygen in the Southeast Atlantic, shown in chapter 2 (Equation 7). *C. wuellerstorfi* and *P. ariminensis* lives in the on top of the sediment in the bottom water. *Globobulimina spp.* migrates within the sediment column where the anoxic boundary occurs. Consequently, $\delta^{13}C$ of *C. wuellerstorfi* and *P. ariminensis* represents bottom-water $\delta^{13}C$. $\delta^{13}C$ of *Globobulimina spp.* represents the anoxic pore-water $\delta^{13}C$. Increase levels of oxygen at the sediment-water interface leads to a greater release of isotopically light $\delta^{13}C$ into pore-waters, thereby amplifying the $\delta^{13}C$ gradient between bottom waters and the anoxic pore waters. There is a strong linear relationship between $\Delta\delta^{13}C$ and bottom water oxygen up to 293 μmol/kg (Equation 7). The standard error of the associated linear regression is 30 μmol/kg (1-sigma).

3.3 Results and Discussion

3.3.1 Glacial-Interglacial Changes in the Southeast Atlantic

Late Holocene and LGM oxygen reconstructions were determined for all three core-sites (V29-140, V19-258, V19-259). Figure 20 shows the location of the three core sites. V19-258 and V19-259 are directly in the Benguela Upwelling System. However, V29-140 is slightly north of the Benguela Upwelling System. However, the oxygen profiles at V29-140 and V19-258/V19-259 are similar (Boyer et al. 2013). Figure 21 (left) shows the down-core record of the $\delta^{13}C$ *P. ariminensis/C. wuellerstorfi* and *Globobulimina spp.* As the difference in $\delta^{13}C$ of *P. ariminensis/C. wuellerstorfi* and *Globobulimina spp.* decreases, bottom-water oxygen increases. The scatter in the $\delta^{13}C$ of *Globobulimina spp.* at all core-sites highlights the importance of multiple measurements at each depth to obtain a reliable oxygenation estimate.

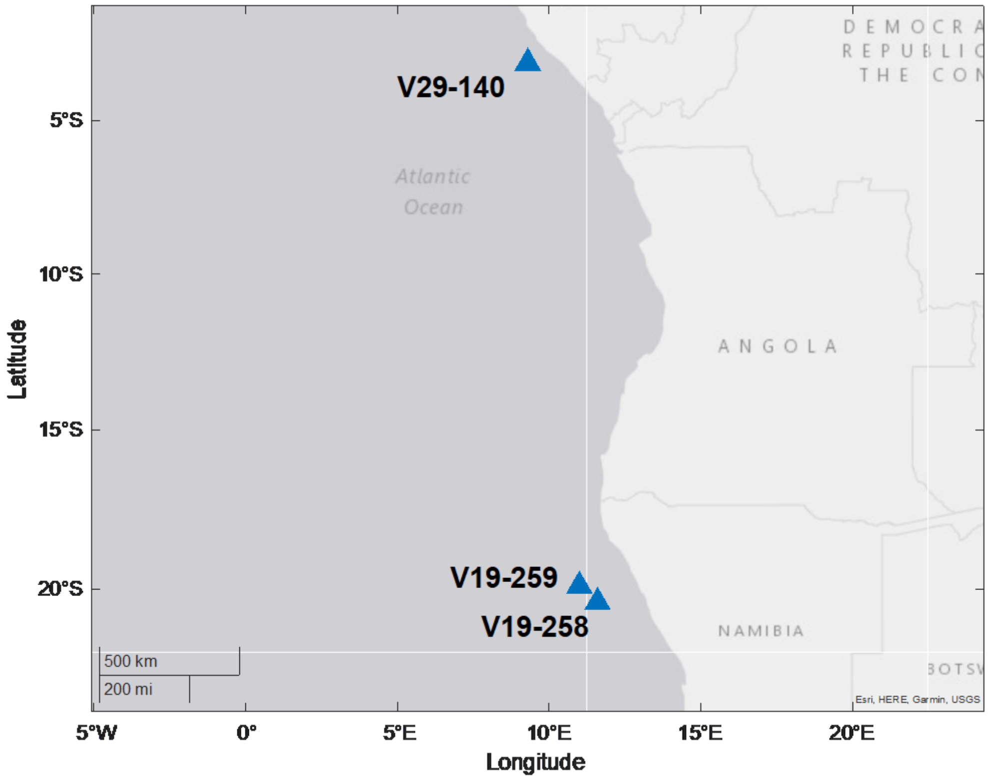

Figure 20 - Location of core-sites. V29-140 is labeled as 1. V19-258 is labeled as 2. V19-258 is labeled as 3.

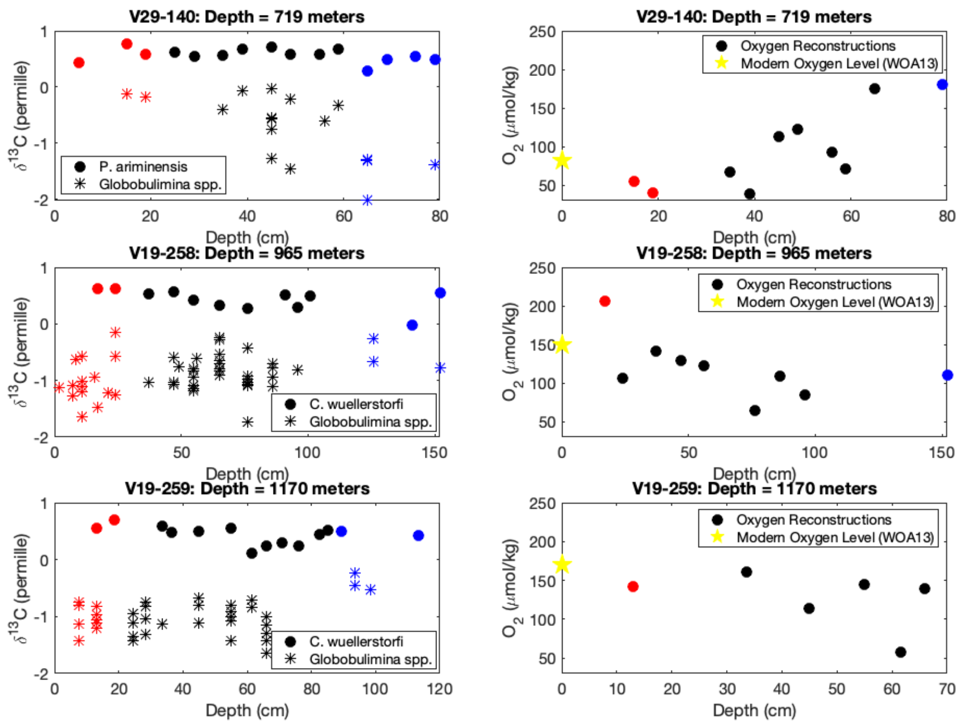

Figure 21 - (left) δ¹³C record of *C. wuellerstorfi* and *Globobulimina spp*. for each core. (right) Oxygen reconstruction for each core using the updated calibration from equation 7. Red represents late Holocene time slice. Blue represents LGM time slice. The yellow star represents modern oxygenation based on World Ocean Atlas 2013 (Boyer et al. 2013).

The oxygen reconstructions in Figure 21 are based on late Holocene and LGM depths with both δ¹³C values of *Globobulimina spp.* and *P. ariminensis/C. wuellerstorfi*. In Figure 22, oxygen reconstructions are averaged across all late Holocene or LGM depths, irrespective of species being found at the same depth within a core. Overall, late Holocene oxygen reconstructions for V19-258 (depth = 965 m) and V19-259 (depth = 1170 m), the two deepest cores, agree with modern oxygen estimates from World Ocean Atlas 2013

(Figure 21 (right), Figure 22, Table 4). However, late Holocene oxygen reconstruction for V29-140 (depth = 712 m) slightly underestimate the modern oxygen estimates. For this core, late Holocene $\delta^{13}C$ values of *Globobulimina spp.* are derived from only 2 depths. At a single depth within a core, the $\delta^{13}C$ for *Globobulimina spp.* can have a range that exceeds 1‰. This limited late Holocene data may contribute to the slight underestimation.

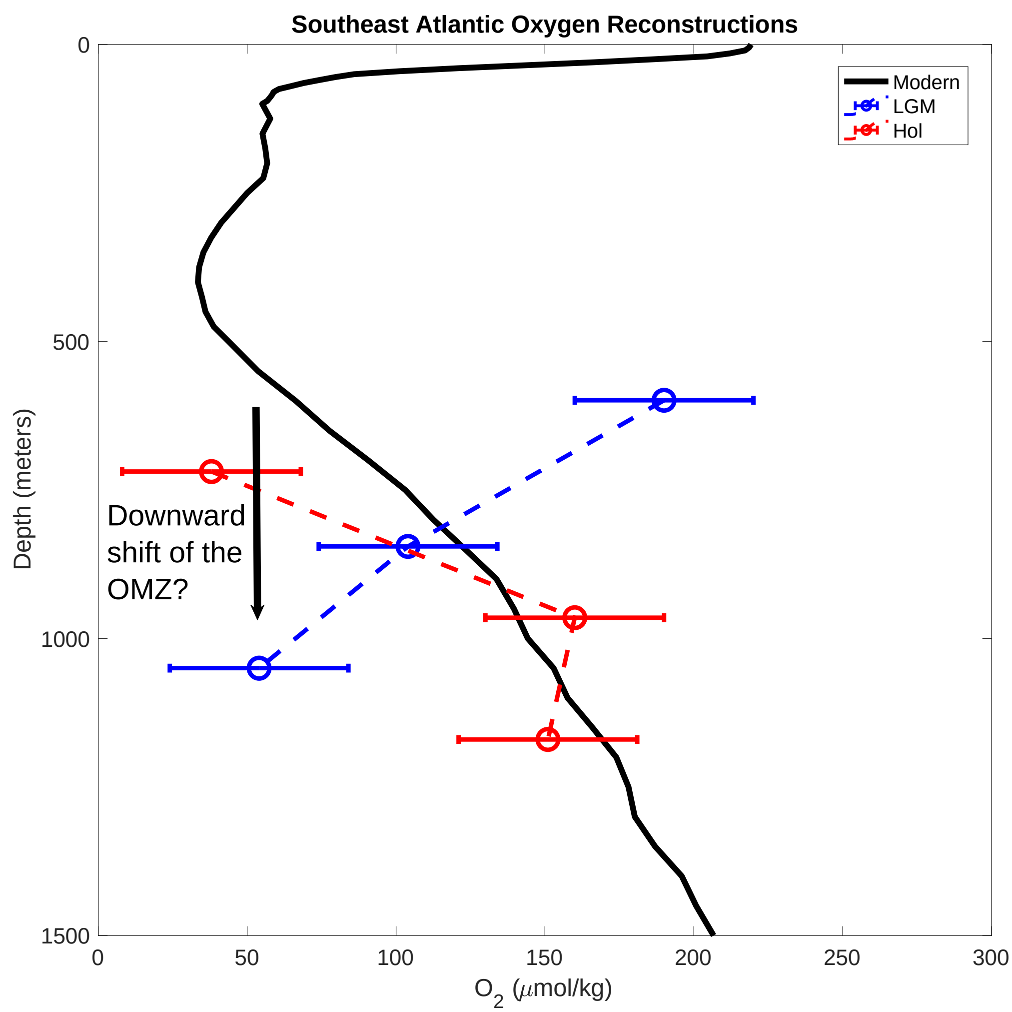

Figure 22 - Late Holocene and LGM oxygen reconstructions for V29-140, V19-258, V19-259. The LGM oxygen reconstructions for each core-site are shown at a depth 120 meters less than the modern depth due to lower sea level during the LGM (Clark & Mix, 2002). The errors shown are the RMSE from the calibration. Modern O_2 profile is from WOA13 at latitude: 19.5 degrees south and longitude: 10.5 degrees .

Table 4 - Summary of oxygen reconstructions for the LGM and late Holocene for V29-140, V19-258, and V19-259.

				Globobulimina spp. $\delta^{13}C$ (per mille)		*C. wuellerstorfi/P. ariminensis* $\delta^{13}C$ (per mille)		O_2 (µmol/kg)		
Core	Lat.	Long.	Depth (m)	Late Hol.	LGM	late Hol.	LGM	Modern	Late Hol.	LGM
V29-140	-3.1	9.3	719	-0.15	-1.51	0.59	0.45	82	38	190
V19-258	-20.4	11.6	965	-1.10	-0.87	0.62	0.40	150	160	104
V19-259	-19.9	11	1170	-1.03	-0.41	0.63	0.47	170	151	54

The shallowest core (V29-140) is located within the South Atlantic Central Waters. South Atlantic Central Waters originate from the subduction of subtropical mode waters (Y. Chen et al., 2022). Overall, we found an increase in oxygenation in the South Atlantic Central Waters. One potential factor for this increase in oxygenation is an increase in oxygen solubility during the LGM due to cooler ocean temperatures. There are currently no temperature estimates at this depth in the Southeast Atlantic. However, the deeper AAIW likely cooled by about 3 degrees Celsius (Elmore et al., 2015). A cooling of 3 degrees Celsius leads to an increase of oxygen saturation of only around 25 μmol/kg. This is minor in comparison to the ~130 μmol/kg increase in oxygenation observed at V29-140. This suggests that alterations in ocean circulation or surface productivity are the primary drivers of the observed change. The next deepest core (V19-258) is located within the Antarctic Intermediate Waters. There is little to no change in oxygenation compared to modern at this location. The deepest core (V19-259) is located with the NADW. We see a significant decrease in oxygenation of ~100 μmol/kg in agreement with other deep ocean oxygen reconstructions (Gottschalk, Skinner, et al., 2016; Hoogakker et al., 2015, 2018; Vollmer et al., 2022).

Lu et al., 2020 reconstructed changes in oxygen at a core-site (1997 meters deep) in the Benguela Upwelling System using I/Ca and found no time period with anoxic oxygen levels over the last 240,000 years. This agrees with our oxygen reconstructions. Additionally, nitrogen isotope reconstructions in this region show higher oxygenation during the LGM, in agreement with our shallow (V29-140) quantitative oxygen reconstruction (Jaccard & Galbraith, 2012).

Quantitative oxygen reconstructions have been conducted in the Arabian Sea and Peruvian margin oxygen minimum zones (OMZs) (Glock et al., 2022; Lu et al., 2023). In the Arabian Sea, OMZ levels remained consistently low (<50 μmol/kg) based on aU and I/Ca reconstructions, suggesting no expansion or shift during the Last Glacial Maximum (LGM). However, $\Delta\delta^{13}C$ reconstructions show an increase in oxygenation within the OMZ during the LGM of around 75 μmol/kg (Lu et al., 2023). This magnitude of change is similar to the oxygen increase of ~135 μmol/kg found at core V29-140, also located within an OMZ.

Glock et al., 2022 reconstructed oxygen off the coast of Peru using the pore-density of epibenthic foraminifera. They observed higher oxygenation within the OMZ during the LGM compared to the late Holocene, consistent with other quantitative proxies (Erdem et al., 2020; Scholz et al., 2014) and qualitative proxies (Jaccard & Galbraith, 2012). However, unlike our reconstruction, they did not identify any structural shift in the OMZ.

3.3.2 Potential Mechanisms for the Shift in the OMZ

We observed a downward shift of the OMZ during the LGM for the Southeast Atlantic (Figure 22). Changes in oxygen saturation could not explain the significant change in oxygenation at all the core-sites. A compilation of paleo-productivity suggests generally higher productivity in the southeast Atlantic during the LGM relative to the late Holocene (Mollenhaur et al. 2002, Lu et al. 2020). This would have led to increased oxygen consumption in the water column, leading to a reduction in oxygen concentrations and ultimately reinforcing the OMZ. This is contrary to the observed increase of oxygenation found at the shallowest core site (Figure 22). Consequently, an increase oxygen supply to depths of 600 meters through improved ventilation is required to explain this increase in oxygenation. Little no change in oxygenation for V19-258, core within the AAIW, is observed in other cores sampling AAIW in the South Indo-Pacific (Chapter 2). A decrease in oxygenation for V19-259 agrees with other deep ocean (> 1000 meters) oxygen reconstructions, most likely due to an increase in deep ocean storage of respired carbon through an increase in the biological pump efficiency. Overall, the observed shift in the OMZ can be explained by an increase of oxygenation for in the upper water column (0 – 600 meters) through an increase in ventilation and a decrease in oxygenation for the deep ocean (>1000 meters) through an increase in deep ocean respire carbon storage through an increased biological pump efficiency.

3.4 Conclusions

Applying the updated oxygen calibration discussed in Chapter 2, we conducted three additional oxygen reconstructions in the Southeast Atlantic near the Benguela Upwelling System. Our findings indicate a deepening of the OMZ during the LGM, characterized by heightened oxygen levels at the shallowest site (V29-140) and reduced oxygenation at the deepest site (V19-259). These results align qualitatively with existing oxygen reconstructions in the area (Jaccard et al 2012). However, the extent of oxygenation increase at the shallowest site (V29-140) cannot be fully explained by an increase of oxygen saturation or a decrease in productivity. Additional LGM oxygen reconstructions at shallower depths (<600 meters) and LGM ventilation age assessments would offer more precise insights into the dynamic shifts in the OMZ in the Southeast Atlantic.

CHAPTER 4. SUGGESTION ON FUTURE WORK

The reconstruction of oxygen and nutrient levels in the past ocean is crucial for understanding past environmental conditions. By examining the variations in oceanic oxygen and nutrients concentrations during the past, we developed further understanding on climate dynamics, ocean circulation patterns, and biogeochemical processes. Such reconstructions provide a valuable context for interpreting present-day changes and predicting future trends. This thesis has developed a new method to reconstruct preformed phosphate in the past using a combination of quantitative oxygen, phosphate, and temperature reconstructions. The number of preformed phosphate reconstructions were limited due to the limit on quantitative oxygen estimates.

Chapter 1 describe a method of reconstructing preformed phosphate during the LGM using a combination of quantitative oxygen, phosphate, and temperature reconstructions. The number of preformed phosphate reconstructions were limited on the amount of paired oxygen and phosphate reconstructions. We used only 3 preformed phosphate reconstructions in the deep Indo-Pacific to evaluate the amount of pCO_2 decrease due to an increase in the biological pump efficiency. Increase preformed phosphate reconstruction in regions of deep-water formations can help better constrain this estimate. Additionally, there is a higher resolution core found off the coast of New Zealand (RR0503-87) where we can reconstruct preformed phosphate to help investigate temporal changes in the biological pump efficiency since the Last Glacial Maximum for southern sourced intermediate waters.

Additionally, in chapter 1, I reconstructed preformed $\delta^{13}C$ using oxygen and temperature estimates in the past. Using a combination of preformed $\delta^{13}C$ reconstructions and $\delta^{13}C_{as}$ (method laid out in Lynch-Stiegltiz et al 1996) can help us better understand air-sea exchanges in the past.

Chapter 2 updated the $\Delta\delta^{13}C - O_2$ paleo-oxygen proxy from six cores (Hoogakker et al., 2015) to 31 cores, globally. However, the mechanism for the imperfect relationship is still not fully understood. While initial models have been used to investigate this relationship (McCorkle & Emerson, 1988), using a more complex marine sedimentary carbonate diagenesis model (e.g. Kanzaki et al., 2021) can help explore the different mechanisms control the distribution of $\delta^{13}C$ with the sediment and the $\delta^{13}C$ signature of *Globobulimina spp.* More specifically, it would be interesting to evaluate the role of carbon export flux on $\Delta\delta^{13}C$.

Chapter 3 reconstructed oxygen in the Southeast Atlantic at three core-sites near or within the Benguela Upwelling System OMZ. Many cores within this region do not have paired infaunal *Globobulimina spp.* and epifaunl *C. wuellerstorfi.* This means that we cannot reconstruct oxygen using the $\Delta\delta^{13}C - O_2$ paleo-oxygen proxy. However, recently there have been new ways to quantify oxygen in the past using the pore-area on benthic foraminifera (Rathburn et al., 2018). More oxygen reconstructions in this area can better constrain the changes in the OMZ during the LGM. Additionally, there is a lack of phosphate reconstructions in this area. A combination of phosphate and oxygen reconstructions can help reconstruct preformed phosphate in the past for this region to better constrain the role of the biological pump efficiency during the LGM for each water mass.

APPENDIX A. SUPPLEMENTARY INFORMATION TO "PROXY-BASED PREFORMED PHOSPHATE ESTIMATES POINT TO INCREASED BIOLOGICAL PUMP EFFICIENCY AS PRIMARY CAUSE OF LAST GLACIAL MAXIMUM CO_2 DRAWDOWN

A.1 Introduction

Here we show a summarization of the data contributing to the estimates of preformed phosphate and preformed $\delta^{13}C$ (Section A.2) and how the errors for these estimations were determined (Section A.3).

A.2 Core Data Summary

Below we summarize the data contributing to the estimates of preformed PO_4 and $\delta^{13}C$ at each site where pore water oxygen reconstructions are available. All data has been previously published in studies by other authors, and the original sources are indicated.

For all site locations, current estimates of phosphate, oxygen, temperature, and salinity are taken from World Ocean Atlas 2013 (WOA13) as a linear interpolations at the latitude, longitude, and depth where the oxygen reconstructions are located (Boyer et al., 2013). For all core-sites, Late Holocene bottom-water temperature and salinity are taken as the WOA13 estimate.

For all core-sites, LGM salinity is assumed to be 1 PSU larger than the current WOA13 salinity respective estimates(Boyer et al., 2013). We assume that LGM bottom-water temperatures were 0 - 5 ◦C lower than modern WOA13 values at the core sites, GeoB3004-1, MD99-2328, and ODP-1242, where there are no LGM temperature reconstructions, incorporating this large range into our error estimates. While there are few published estimates of intermediate water temperature in the far North Atlantic, Antarctic Intermediate Water likely cooled by about 3°C (Elmore et al., 2015), and the whole ocean volume is estimated to have cooled by 2.57±.24°C (Bereiter et al., 2018).

Core: MD07-3076Q:

Last Glacial Maximum (LGM) *C. wuellerstrofi* $\delta^{13}C$ is an average of 6 measurements at down-core depths from 1.355 to 1.445 meters (19.223 ka BP - 20.374 ka BP) (Gottschalk et al., 2016). LGM *G. affinis* $\delta^{13}C$ is an average of 14 measurements at depths from 1.345 to 1.605 meters (19.132 ka BP - 22.733 ka BP)(Gottschalk et al., 2016). LGM Temperature is from *Uvigerina spp. Mg/Ca* and is an average of 8 measurements at depths from 1.365 to 1.625 (19.268 ka BP - 21.4745 ka BP) (Roberts et al., 2016). LGM sea-water cadmium (Cd_w) is estimated to be the average of LGM values at nearby core-sites: RC12-292, RC12-267, and RC12-294 (Boyle, 1992; Marchitto & Broecker, 2006; Rosenthal et al., 1997).

Core MD95-2042:

LGM *C. wuellerstorfi* $\delta^{13}C$ is an average of 6 measurements at down-core depths from 6.12 to 7.12 meters (19.087 ka BP - 21. 65 ka BP) (Hoogakker et al., 2015). LGM *G. affinis* $\delta^{13}C$ is an average of 33 measurements at depths from 6.12 to 7.64 meters (19.087 ka - 22.983 ka) (Hoogakker et al., 2015). LGM Temperature is from *G. affinis* Mg/Ca and is an average of 18 down-core depths from a nearby core-site, MD99-2334K: 19.079 ka BP to 22.966 ka BP (Skinner et al., 2003). LGM Cd_w is estimated to be the average of LGM values at nearby core-sites V30-97, CHN82-4, CHN82-11, and IOS82-PC-SO1(Boyle, 1992; Marchitto et al., 2002; Marchitto & Broecker, 2006).

Core GeoB3004-1:

Late Holocene *C. wuellerstorfi* $\delta^{13}C$ is an average of six measurements at down-core depths from 0.03 to 0.28 meters (0.6 ka BP - 5.4 ka BP) (Schmiedl & Mackensen, 2006). Late Holocene *G. affinis* $\delta^{13}C$ is an average of six measurements at depths from 0.03 to 0.28 meters (0.6 ka BP - 5.4 ka BP) (Schmiedl & Mackensen, 2006). Late Holocene Cd_w is taken as the average of nine values from a nearby core-site, MD76-135, at depths from 0 to 70 cm (0 ka BP - 5.74 ka BP) (Boyle et al., 1995).

LGM *C. wuellerstorfi* $\delta^{13}C$ is an average of seven measurements at down-core depths from 1.03 to 1.33 meters (19.2 ka BP - 22.8 ka BP) (Schmiedl & Mackensen, 2006). LGM *G. affinis* $\delta^{13}C$ is an average of 6 measurements at depths from 1.03 to 1.33 meters (19.2 ka BP - 22.8 ka BP) (Schmiedl & Mackensen, 2006). LGM Cd_w is taken as the average of nine values from a nearby core-site, MD76-135, at depths from 220 - 232 cm (19.77 ka BP - 23.54 ka BP) (Boyle et al., 1995).

Core MD99-2328:

LGM *C. wuellerstorfi* $\delta^{13}C$ is an average of 22 measurements at down-core depths from 1.03 to 1.33 meters (19.2 ka BP - 22.8 ka BP) (Mojtahid et al., 2017). LGM *G. affinis* $\delta^{13}C$ is an average of three measurements at depths from 11.2 to 19.6 meters (19.18 ka BP - 21.43 ka BP) (Mojtahid et al., 2017). LGM Cd_w is interpolated from the LGM compilation in Marchitto & Broecker (2006).

Core TR163-23:

LGM *C. wuellerstorfi* $\delta^{13}C$ is an average of two measurements at down-core depths from 184.5 to 189.5 cm (22.7 ka BP - 22.8 ka BP) (Umling et al., 2018). LGM *G. affinis* $\delta^{13}C$ is the measurement at depth 174.5 cm (21.1 ka BP) (Umling et al., 2018). LGM temperature is from *C. wuellerstorfi Mg/Ca,* and is an average of six measurements from a nearby core-site, TR163-20B, at depths from 99 - 124 cm (Martin et al., 2005). LGM Cd_w is an average of three values at depths from 179.5 to 189.5 cm (21.7 ka BP - 22.8 ka BP) (Umling et al., 2018).

Core TR163-25:

Late Holocene *C. wuellerstorfi* $\delta^{13}C$ is an average of five measurements at down-core depths from 0.005 to 0.2 meters (3.8 ka BP - 5.7 ka BP) (Hoogakker et al., 2018). Late Holocene *G. affinis* $\delta^{13}C$ is an average of four measurements at depths from 0.005 to 0.05 meters (3.757 ka BP - 4.204 ka BP) (Hoogakker et al., 2018). Late Holocene Cd_w is estimated to be an average of Late Holocene values of nearby core-sites, TR163-23, V19-29, V19-30, TR163-31B, KNR73-3JPC and KNR73-4JPC (Boyle, 1992; Umling et al., 2018).

LGM *C. wuellerstorfi* $\delta^{13}C$ is an average of six measurements at down-core depths from 1.03 to 1.605 meters (21.1 ka BP - 22.7 ka BP) (Hoogakker et al., 2018). LGM *G. affinis* $\delta^{13}C$ is an average of 14 measurements at depths from 1.03 to 1.605 meters (19.2 ka BP - 22.8 ka BP) (Hoogakker et al., 2018). LGM temperature is from *C. wuellerstorfi Mg/Ca* and is an average of six measurements from a nearby core-site, TR163-20B, at depths from 99 - 124 cm(P. Martin et al., 2005). LGM Cd_w is estimated to be an average of LGM values of nearby core-sites, TR163-23, V19-29, V19-30, TR163-31B, KNR73-3JPC and KNR73-4JPC (Boyle, 1992).

A down-core record for Cd_w exists for core TR163-25 (Umling et al., 2018). However, the LGM Cd_w at this site is 2 standard deviations outside the mean of the nearby cores. Because of this, we excluded this data point in our estimates for TR162-35 LGM and Late Holocene Cd_w.

Core ODP-1242:

Late Holocene *C. wuellerstorfi* $\delta^{13}C$ is an average of 17 measurements at down-core depths from 0.05 to 1.05 meters (0.285 ka BP - 5.985 ka BP) (Hoogakker et al., 2018). Late Holocene *G. affinis* $\delta^{13}C$ is an average of 17 measurements at depths from 0.01 to 5.985 meters (0.057 ka BP - 5.985 ka BP) (Hoogakker et al., 2018). Late Holocene Cd_{sw} is the average of four values from a nearby core-site, V19-27, at depths from 6 to 49 cm (Boyle, 1992).

LGM *C. wuellerstorfi* $\delta^{13}C$ is an average of five measurements at down-core depths from 1.03 to 1.605 meters (21.1 ka BP - 22.7 ka BP) (Hoogakker et al., 2018). LGM *G. affinis* $\delta^{13}C$ is an average of seven measurements at depths from 1.03 to 1.605 meters (19.2 ka BP - 22.8 ka BP) (Hoogakker et al., 2018). LGM Cd_w is an average of four values from a nearby core site, V19-27, at depths from 108.5 to 127.5 cm (Boyle, 1992).

A.3 Calculation of $P_{pre,AOU}$, Preformed $\delta^{13}C_{pre,AOU}$ Error, and pCO_2 Drawdown Error

The 1-sigma standard error on the estimate for *C. wuellerstorfi* $\delta^{13}C$ and *G. affinis* $\delta^{13}C$ for each location is calculated using the data from the depths that are averaged to determine the average value at each core site for each time horizon. The error associated with the conversion of $\Delta\delta^{13}C$ to O_2 is the root mean squared error (RMSE) associated with the linear fit of the calibration: 0.135 μmol/kg (Figure 3). The error associated with the conversion of *AOU* to P_{reg} is 10 [μM] (Anderson & Sarmiento, 1994). The error associated with the conversion of *AOU* to $\delta^{13}C_{reg}$ is 0.06 [μM^{-1}] (Broecker & Maier-Reimer, 1992).

The error associated with the conversion of Cd_w to P is the RMSE associated with the nonlinear fit of the calibration: 0.3 µmol/kg (Figure 1).

The error on the derived quantities, $P_{pre,AOU}$ and $\delta^{13}C_{pre,AOU}$, are first determined by propagating all of the above errors into the final error estimates. There is an additional source of error when determining global $P_{pre,AOU}$ from the two deep Equatorial Pacific and the deep Arabian sea sites. The first error comes from the scatter of the change in $P_{pre,AOU}$ at these locations: the 2-sigma standard deviation is 0.11 µM. Another source of error is the extrapolation from average $P_{pre,AOU}$ at these three sites to the global change in $P_{pre,AOU}$. Figure 4 shows a potential overestimation of the changes to the global $P_{pre,AOU}$ by 4%. Including this uncertainty, we get a total error of 0.13 µM for the global change in $P_{pre,AOU}$.

For a 0.53$\pm$0.13 µM change of preformed phosphate, this will correspond to an error of 16 ppm to the pCO_2 drawdown, when assuming that $P_{pre,AOU}$ changes completely represent changes in true P_{pre}. Changes in sea-ice extent can decouple $P_{pre,AOU}$ and true P_{pre}. Assuming that the Southern Ocean sea-ice extent did not increase by more than 6 degrees latitude north, this would introduce an additional 12 ppm uncertainty in the pCO_2 drawdown due to an increase in the biological pump efficiency, bringing the total to uncertainty in our pCO_2 drawdown due to the change in the biological pump efficiency to 28 ppm (Figure 14). This 12 ppm uncertainty is also included when converting global $\delta^{13}C_{pre,AOU}$ to atmospheric pCO_2 due to changes in the biological pump efficiency.

APPENDIX B. SUPPLEMENTARY INFORMATION TO "DECREASED OF DEEP OCEAN OXYGEN AND PHOSPHATE IN THE SOUTH PACIFIC DURING THE LAST GLACIAL MAXIMUM"

Table 5 - Summary of *Globobulimina spp.* data used for the updated $\Delta\delta^{13}C - O_2$ paleo-oxygen proxy.

Core Name	latitude (deg N)	longitude (deg E)	Depth (meters)	*Globobulimina spp.* d13C (%.)	*Globobulimina spp.* d13C error (%.)	# of specimen	reference
RS67-GC27	-38.64	141.18	366	-0.30	0.10	4	This study
RS67-GC13	-38.46	140.17	2525	-1.95	0.10	4	This study
V29-140	-3.12	-9.32	719	-0.66	0.24	3	This study
V19-258	-20.40	11.62	965	-1.09	0.18	3	This study
V19-259	-19.87	11.03	1170	-1.07	0.09	3	This study
GeoB9512	15.34	-17.37	795	-0.36	0.07	5	This study
51JPC	24.40	-83.22	198	-0.17	0.07	5	This study
48JPC	24.40	-83.23	247	-0.15	0.06	5	This study
105JPC	24.57	-79.24	304	-0.09	N/A	1	This study
106JPC	24.57	-79.24	354	-0.21	0.12	5	This study
59JPC	22.05	-22.09	358	-0.41	0.17	5	This study
113JPC	24.65	-79.24	402	0.10	N/A	1	This study
135JPC	24.84	-79.22	446	0.10	0.19	5	This study
127JPC	24.77	-79.28	631	0.09	0.02	5	This study
27GCC	24.32	-83.26	598	-0.50	0.06	5	This study
1GGC	24.39	-83.34	446	-0.53	0.13	5	This study
V19-28	2.87	-87.75	2246	-1.50	N/A	1	This study
ODP 846	-3.09	-90.8	3295	-1.75	N/A	N/A	Jacobel et al. 2020
ODP 1240	0.02	-86.5	2921	-1.94	N/A	N/A	Jacobel et al. 2020
TR163-23	0.41	-92.2	2730	-1.62	N/A	N/A	Umling et al. 2018

Table 5 – Continued.

TR163-25	-1.65	-88.5	2650	-1.55	N/A	N/A	Hoogakker et al. 2018
ODP 1242	7.86	-83.6	1364	-0.72	N/A	N/A	Hoogakker et al. 2016
RAPID 11 7B/RAPID 13 9B	62.3	-17.2	2126	-1.84	N/A	N/A	Hoogakker et al. 2016
GeoB3706	-22.7	12.6	1313	-1.15	N/A	N/A	Mackensen and Licari, 2004
GeoB3708	-21.1	11.8	1283	-1.27	N/A	N/A	Mackensen and Licari, 2004
GeoB3725	-23.3	12.4	1980	-1.3	N/A	N/A	Mackensen and Licari, 2004
GeoB3004	14.6	52.9	1803	-1.01	N/A	N/A	Schmiedl and Mackensen, 2006
GeoB3606-1	-25.5	13.1	1785	-1.4	N/A	N/A	Mckay et al. 2016
KNR197-3-41MC	8.38	-53.1	2052	-1.46	N/A	N/A	Lu et al. 2023
KNR197-3-37MC	8.43	-52.8	2440	-1.51	N/A	N/A	Lu et al. 2023
KNR197-3-35MC	8.47	-52.8	3328	-1.66	N/A	N/A	Lu et al. 2023

Table 6 - Summary of *C. wuellerstorfi* or P. ariminensis data used for the updated $\Delta\delta13C$ – O_2 paleo-oxygen proxy

Core Name	latitude (deg N)	longitude (deg E)	Depth (meters)	*C. wuellerstorfi/P. ariminensis* d13C (%.)	d13C error (%.)	# of specimen	Which specimen?	reference
RS67-GC27	-38.64	141.18	366	1.59	0.04	2	*C. wuellerstorfi*	Lynch-Stiegltiz et al. 1994
RS67-GC13	-38.46	140.17	2525	0.24	N/A	1	*C. wuellerstorfi*	Lynch-Stiegltiz et al. 1994
V29-140	-3.12	-9.32	719	0.70	0.07	5	*C. wuellerstorfi and P. ariminensis*	Lynch-Stiegltiz et al. 2006
V19-258	-20.40	11.62	965	0.63	0.01	2	*C. wuellerstorfi*	Lynch-Stiegltiz et al. 2006
V19-259	-19.87	11.03	1170	0.63	0.05	2	*C. wuellerstorfi*	Lynch-Stiegltiz et al. 2006
GeoB9512	15.34	-17.37	795	0.91	0.10	3	*C. wuellerstorfi*	Lynch-Stiegltiz et al. 2006

Table 6 – Continued.

51JPC	24.40	-83.22	198	1.30	0.05	3	*P. ariminensis*	This study
48JPC	24.40	-83.23	247	1.40	0.04	4	*P. ariminensis*	This study
105JPC	24.57	-79.24	304	1.52	0.02	2	*P. ariminensis*	This study
106JPC	24.57	-79.24	354	1.52	0.01	2	*P. ariminensis*	This study
59JPC	22.05	-22.09	358	1.22	N/A	1	*P. ariminensis*	This study
113JPC	24.65	-79.24	402	1.20	0.03	2	*P. ariminensis*	This study
135JPC	24.84	-79.22	446	1.30	0.03	2	*P. ariminensis*	This study
127JPC	24.77	-79.28	631	1.35	0.03	1	*P. ariminensis*	This study
27GCC	24.32	-83.26	598	1.28	N/A	4	*P. ariminensis*	This study
1GGC	24.39	-83.34	446	1.32	0.04	2	*P. ariminensis*	This study
V19-28	2.87	-87.75	2246	0.13	0.02	3	*C. wuellerstorfi*	This study
ODP 846	-3.09	-90.82	3295	-0.14	N/A	N/A	*C. wuellerstorfi*	Jacobel et al. 2020
ODP 1240	0.02	-86.46	2921	0.22	N/A	N/A	*C. wuellerstorfi*	Jacobel et al. 2020
TR163-23	0.41	-92.16	2730	0.16	N/A	N/A	*C. wuellerstorfi*	Umling et al. 2018
TR163-25	-1.65	-88.45	2650	0.14	N/A	N/A	*C. wuellerstorfi*	Hoogakker et al. 2018
ODP 1242	7.86	-83.61	1364	0.36	N/A	N/A	*C. wuellerstorfi*	Hoogakker et al. 2016
RAPID 11 7B/RAPID 13 9B	62.3	-17.15	2126	1.29	N/A	N/A	*C. wuellerstorfi*	Hoogakker et al. 2016
GeoB3706	-22.7	12.6	1313	0.64	N/A	N/A	*C. wuellerstorfi*	Mackensen and Licari, 2004

Table 6 – Continued.

GeoB3708	-21.1	11.8	1283	0.48	N/A	N/A	*C. wuellerstorfi*	Mackensen and Licari, 2004
GeoB3725	-23.3	12.4	1980	0.6	N/A	N/A	*C. wuellerstorfi*	Mackensen and Licari, 2004
GeoB3004	14.6	52.9	1803	0.5	N/A	N/A	*C. wuellerstorfi*	Schmiedl and Mackensen, 2006
GeoB3606-1	-25.47	13.08	1785	0.5	N/A	N/A	*C. wuellerstorfi*	Mckay et al. 2016
KNR197-3-41MC	8.38	-53.05	2052	1.14	N/A	N/A	*C. wuellerstorfi*	Costa et al. 2023
KNR197-3-37MC	8.43	-52.79	2440	1.39	N/A	N/A	*C. wuellerstorfi*	Costa et al. 2023
KNR197-3-35MC	8.47	-52.79	3328	1.17	N/A	N/A	*C. wuellerstorfi*	Costa et al. 2023

Table 7 - Summary of data for the updated Δδ^{13}C – O_2 paleo-oxygen proxy. Δδ^{13}C is the difference in δ^{13}C between *Globobulimina spp.* (Table 5) and *C. wuellerstorfi/P. ariminensis* (Table 6).

Core Name	latitude (deg N)	longitude (deg E)	Depth (meters)	Δd13C (%.)	Δd13C error (%.)	O2 Estimate (umol/kg)	Source of O2 Estimate?
RS67-GC27	-38.64	141.18	366	1.89	0.10	240	WOA13
RS67-GC13	-38.46	140.17	2525	2.19	N/A	180	WOA13
V29-140	-3.12	-9.32	719	1.36	0.25	134	WOA13
V19-258	-20.40	11.62	965	1.72	0.18	139	WOA13
V19-259	-19.87	11.03	1170	1.69	0.11	174	WOA13
GeoB9512	15.34	-17.37	795	1.27	0.12	90	WOA13
51JPC	24.40	-83.22	198	1.47	0.09	159	WOA13
48JPC	24.40	-83.23	247	1.54	0.07	139	WOA13
105JPC	24.57	-79.24	304	1.61	N/A	155	WOA13
106JPC	24.57	-79.24	354	1.74	0.12	180	WOA13
59JPC	22.05	-22.09	358	1.63	N/A	127	WOA13
113JPC	24.65	-79.24	402	1.10	N/A	166	WOA13
135JPC	24.84	-79.22	446	1.20	0.20	155	WOA13
127JPC	24.77	-79.28	631	1.25	0.04	128	WOA13
27GCC	24.32	-83.26	598	1.79	N/A	131	WOA13
1GGC	24.39	-83.34	446	1.85	0.14	194	WOA13
V19-28	2.87	-87.75	2246	1.63	N/A	132.6	WOA13
ODP 846	-3.09	-90.8	3295	1.61	N/A	140	WOA13
ODP 1240	0.02	-86.5	2921	2.16	N/A	128	WOA13
TR163-23	0.41	-92.2	2730	1.78	N/A	121	WOA13
TR163-25	-1.65	-88.5	2650	1.69	N/A	122	WOA13
ODP 1242	7.86	-83.6	1364	1.08	N/A	102	WOA13
RAPID 11 7B/RAPID 13 9B	62.3	-17.2	2126	3.13	N/A	293	WOA13
GeoB3706	-22.7	12.6	1313	1.79	N/A	182	WOA13
GeoB3708	-21.1	11.8	1283	1.75	N/A	180	WOA13
GeoB3725	-23.3	12.4	1980	1.90	N/A	221	WOA13
GeoB3004	14.6	52.9	1803	1.51	N/A	147	WOA13
GeoB3606-1	-25.5	13.1	1785	1.90	N/A	210	WOA13

Table 7 – Continued.

KNR197-3-41MC	8.38	-53.1	2052	2.60	N/A	252	WOA13
KNR197-3-37MC	8.43	-52.8	2440	2.90	N/A	254	WOA13
KNR197-3-35MC	8.47	-52.8	3328	2.83	N/A	257	WOA13

Table 8 - Summary of oxygen reconstruction in the South Indo-Pacific. "H" represent late Holocene. "LGM" represents the Last Glacial Maximum. "n" represents the number of specimens for a given Holocene or LGM estimate. "delta_d13C" represents $\Delta\delta^{13}C$. Modern O_2 estimates are from WOA13.

		C. wuellerstorfi					
Core	Depth	H_avg	H_stderr	H_n	LGM_avg	LGM_stderr	LGM_n
RS67-GC27	506	1.61	0.02	6	1.91	0.01	3
RS78-GC18	814	N/A	N/A	N/A	1.25	0.00	2
SO36-7	1225	N/A	N/A	N/A	0.66	N/A	1
RS67-GC52	1145	N/A	N/A	N/A	0.63	N/A	1
RS67-GC3	1476	N/A	N/A	N/A	0.49	N/A	1
RS67-GC16	1650	N/A	N/A	N/A	0.21	N/A	1
V18-222	1900	N/A	N/A	N/A	-0.39	0.09	5
RS67-GC13	2525	0.16	0.12	2	-0.22	0.03	4
		G. affinis					
Core	Depth	H_avg	H_stderr	H_n	LGM_avg	LGM_stderr	LGM_n
RS67-GC27	506	-0.32	0.04	5	-0.81	0.24	4
RS78-GC18	814	N/A	N/A	N/A	-1.35	0.05	4
SO36-7	1225	N/A	N/A	N/A	-1.04	0.03	2
RS67-GC52	1145	N/A	N/A	N/A	-1.51	0.05	5
RS67-GC3	1476	N/A	N/A	N/A	-1.23	0.03	3
RS67-GC16	1650	N/A	N/A	N/A	-1.25	0.10	10

Table 8 – Continued.

V18-222	1900	N/A	N/A	N/A	-1.56	0.08	16
RS67-GC13	2525	-2.03	0.10	2	-1.59	0.07	9

		delta_d13C			
Core	Depth	H	H_stderr	LGM	LGM_stderr
RS67-GC27	506	1.61	0.02	1.91	0.01
RS78-GC18	814	N/A	N/A	1.25	0.00
SO36-7	1225	N/A	N/A	0.66	N/A
RS67-GC52	1145	N/A	N/A	0.63	N/A
RS67-GC3	1476	N/A	N/A	0.49	N/A
RS67-GC16	1650	N/A	N/A	0.21	N/A
V18-222	1900	N/A	N/A	0.39	0.09
RS67-GC13	2525	0.16	0.12	0.22	0.03

Core	Depth	Modern_O2 (umol/kg)	H_Recon_O2 (umol/kg)	LGM_Reconstructed_O2 (umol/kg)
RS67-GC27	506	240.00	146.19	184.21
RS78-GC18	814	207.83	N/A	100.94
SO36-7	1225	193.45	N/A	27.50
RS67-GC52	1145	190.40	N/A	24.24
RS67-GC3	1476	173.41	N/A	6.25
RS67-GC16	1650	160.77	N/A	-28.50
V18-222	1900	159.47	N/A	-6.16
RS67-GC13	2525	178.64	-35.31	-27.50

Table 9 - Summary of LGM preformed phosphate reconstructions in EEP and South Indo-Pacific. "O2_recon" are the LGM oxygen reconstructions. "Temp" is temperature estimates from WOA13 subtracted by 2.5 deg C to address a plausible decrease in temperature for the LGM (Bereiter et al., 2018). "Sal" is salinity estimates from WOA13 added by 1 g/kg to address plausible increase in salinity for the LGM (Adkins, 2002). "O2,sat" is the oxygen saturation determined from the temperature and salinity estimates. "Cd_sw" is the Cadmium of seawater estimates from their respective sources. "P" is the phosphate estimate from the "Cd_sw". "P_pre_AOU" is the preformed phosphate estimate. "err" represents the variables respective 1-sigma error.

	Depth	O2_recon	O2_recon error
South Indo-Pacific			
RS67-GC27	506	285.89	30
RS67-GC18	814	269.13	30
SO36-SL7	1085	157.44	30
RS67-GC16	1650	128.31	30
RS67-GC13	2525	116.15	30
Eastern Equatorial Pacific			
TR163-2	1620	56.21	30
TR163-18	2030	702	30
TR163-25	2650	55	30
TR163-20B	3200	55	30

	Depth	Temp	Temp Error	Temp Source
South Indo-Pacific				
RS67-GC27	506	11.2	2.5	WOA13
RS67-GC18	814	9.54	2.5	WOA13
SO36-SL7	1085	3.52	2.5	WOA13
RS67-GC16	1650	1.78	2.5	WOA13
RS67-GC13	2525	0.83	2.5	WOA13
Eastern Equatorial Pacific				
TR163-2	1620	0.29	2.5	WOA13
TR163-18	2030	-0.22	2.5	WOA13

Table 9 – Continued.

TR163-25	2650	-0.50	2.5	WOA13
TR163-20B	3200	-1.00	2.5	WOA13
	Depth	Sal	Sal error	Sal Source
South Indo-Pacific				
RS67-GC27	506	37.1	0.6	WOA13
RS67-GC18	814	36.3	0.6	WOA13
SO36-SL7	1085	36.1	0.6	WOA13
RS67-GC16	1650	36.0	0.6	WOA13
RS67-GC13	2525	36.0	0.6	WOA13
Eastern Equatorial Pacific				
TR163-2	1620	35.6	0.6	WOA13
TR163-18	2030	35.6	0.6	WOA13
TR163-25	2650	35.7	0.6	WOA13
TR163-20B	3200	35.7	0.6	WOA13

	Depth	O2,sat
South Indo-Pacific		
RS67-GC27	506	253.1
RS67-GC18	814	274.8
SO36-SL7	1085	316.1
RS67-GC16	1650	330.4
RS67-GC13	2525	335.7
Eastern Equatorial Pacific		
TR163-2	1620	325.6
TR163-18	2030	344.7
TR163-25	2650	351.3
TR163-20B	3200	355.0

Table 9 – Continued.

	Depth	Cd_sw	Cd source	P	P_err
South Indo-Pacific					
RS67-GC27	506	0.2	Lynch-Stieglitz et al. 1996	1.09	0.3
RS67-GC18	814	0.6	Lynch-Stieglitz et al. 1996	2.17	0.3
SO36-SL7	1085	0.9	Lynch-Stieglitz et al. 1996	2.81	0.3
RS67-GC16	1650	0.8	Lynch-Stieglitz et al. 1996	2.63	0.3
RS67-GC13	2525	0.5	Lynch-Stieglitz et al. 1996	1.91	0.3
Eastern Equatorial Pacific					
TR163-2	1620	1.3	Umling et al. 2018	3.46	0.3
TR163-18	2030	0.8	Umling et al. 2018	2.62	0.3
TR163-25	2650	0.7	Umling et al. 2018	2.39	0.3
TR163-20B	3200	0.7	Umling et al. 2018	2.50	0.3

	Depth	P_pre_AOU	P_pre_AOU_err
South Indo-Pacific			
RS67-GC27	506	2.60	0.34
RS67-GC18	814	2.14	0.34
SO36-SL7	1085	1.88	0.34
RS67-GC16	1650	1.44	0.34
RS67-GC13	2525	0.61	0.34
Eastern Equatorial Pacific			
TR163-2	1620	1.88	0.34
TR163-18	2030	4.72	0.34
TR163-25	2650	0.64	0.34
TR163-20B	3200	0.73	0.34

APPENDIX C. SUPPLEMENTARY INFORMATION TO "LAST GLACIAL MAXIMUM CHANGES IN THE SOUTHEAST ATLANTIC OXYGEN MINIMUM ZONE"

Table 10 - Summary of oxygen reconstruction for V29-140.

Core: V29-140	*Globobulimina spp.*			*P. ariminensis*				
Depth (cm)	# of foram.	δ ^{18}O (permille)	δ ^{13}C (permille)	# of foram.	δ ^{18}O (permille)	δ ^{13}C (permille)	Δ δ 13C (permille)	O_2 (μmol/kg)
5	0	N/A	N/A	5	2.91	0.44	N/A	N/A
15	1	2.86	-0.12	5	2.83	0.76	0.88	54.69
19	1	4.12	-0.18	3	2.36	0.58	0.76	39.69
25	0	N/A	N/A	5	3.16	0.62	N/A	N/A
29	0	N/A	N/A	3	3.1	0.55	N/A	N/A

Table 10 – Continued.

35	1	3.05	-0.41	5	2.87	0.57	0.98	67.19
39	1	3.66	-0.07	3	2.88	0.68	0.75	38.45
45	5	3.60	-0.62	5	3	0.72	1.34	112.64
49	2	4.32	-0.84	3	3.18	0.58	1.42	121.95
56	1	3.91	-0.60	5	2.97	0.58	1.18	93.06
59	1	3.43	-0.32	3	3.01	0.68	1.00	70.58
65	3	4.14	-1.55	2	3.2	0.29	1.84	174.42
69	0	N/A	N/A	2	3	0.48	N/A	N/A
75	0	N/A	N/A	5	3.03	0.55	N/A	N/A
79	1	4.40	-1.39	4	3.12	0.49	1.88	180.28
99	0	N/A	N/A	1	3.07	0.63	N/A	N/A

Table 11 - Summary of oxygen reconstruction for V19-258.

Core: V19-258	*Globobulimina spp.*			*C. wuellerstorfi*				
Depth (cm)	# of foram.	$\delta^{18}O$ (permille)	$\delta^{13}C$ (permille)	# of foram.	$\delta^{18}O$ (permille)	$\delta^{13}C$ (permille)	$\Delta\delta^{13}C$ (permille)	O_2 (μmol/kg)
2	1	2.95	-1.12	0	N/A	N/A	N/A	N/A
7	3	3.26	-1.15	0	N/A	N/A	N/A	N/A
8.5	1	3.22	0.64	0	N/A	N/A	N/A	N/A
11	5	3.16	-1.11	0	N/A	N/A	N/A	N/A
16	1	3.16	-0.95	0	N/A	N/A	N/A	N/A
17	1	3.00	-1.47	3	2.46	0.62	2.09	205.96
21	1	3.12	-1.22	0	N/A	N/A	N/A	N/A
24	3	3.01	-0.65	2	2.15	0.63	1.28	105.62
37	1	3.29	-1.04	3	2.36	0.53	1.57	141.33
47	3	3.23	-0.90	2	2.22	0.57	1.47	128.58
49	1	2.91	0.76	0	N/A	N/A	N/A	N/A
55	6	3.47	-1.00	3	2.37	0.42	1.42	122.55
56	1	3.56	-0.61	0	N/A	N/A	N/A	N/A
65	8	3.72	-0.62	2	2.86	0.33	0.95	63.88

Table 11 – Continued.

76	7	3.99	-1.04	2	2.81	0.28	1.32	109.53
86	4	4.17	-0.89	0	N/A	N/A	N/A	N/A
91	0	N/A	N/A	2	2.77	0.51	N/A	N/A
96	1	3.45	-0.82	2	2.51	0.29	1.11	84.00
101	0	N/A	N/A	3	3.42	0.50	N/A	N/A
126	2	4.54	-0.46	0	N/A	N/A	N/A	N/A
132	0	N/A	N/A	1	3.40	0.57	N/A	N/A
141	0	N/A	N/A	1	3.00	-0.02	N/A	N/A
152	1	4.35	-0.77	2	3.42	0.55	1.32	110.45
211	0	N/A	N/A	1	3.33	0.61	N/A	N/A
221	0	N/A	N/A	1	3.17	0.33	N/A	N/A

Table 12 -Summary of oxygen reconstruction for V19-259.

Core: V19-259	*Globobulimina spp.*			*C. wuellerstorfi*				
Depth (cm)	# of foram.	$\delta^{18}O$ (permille)	$\delta^{13}C$ (permille)	# of foram.	$\delta^{18}O$ (permille)	$\delta^{13}C$ (permille)	$\Delta\delta^{13}C$ (permille)	O_2 (μmol/kg)
7.5	4	3.26	-1.02	0	N/A	N/A	N/A	N/A
13	5	3.24	-1.03	2	2.43	0.55	1.58	142.48
18.5	0	N/A	N/A	1	2.54	0.7	N/A	N/A
24.5	4	3.13	-1.21	0	N/A	N/A	N/A	N/A
28.5	5	3.80	-0.95	0	N/A	N/A	N/A	N/A
33.5	1	3.33	-1.14	3	2.73	0.59	1.73	161.23
36.5	0	N/A	N/A	3	3.01	0.47	N/A	N/A
45	3	3.77	-0.86	2	2.54	0.49	1.35	114.31
55	5	3.72	-1.04	2	2.53	0.56	1.60	145.10

Table 12 – Continued.

61.5	2	4.31	-0.78	3	3.05	0.12	0.90	57.10
66	5	4.19	-1.31	1	3.23	0.25	1.56	139.58
71	0	N/A	N/A	2	3.25	0.3	N/A	N/A
76	0	N/A	N/A	2	3.25	0.25	N/A	N/A
82.5	0	N/A	N/A	2	3.4	0.44	N/A	N/A
85	0	N/A	N/A	3	3.36	0.51	N/A	N/A
89.5	0	N/A	N/A	2	3.31	0.5	N/A	N/A
93.5	2	4.92	-0.34	0	N/A	N/A	N/A	N/A
98.5	1	4.41	-0.53	0	N/A	N/A	N/A	N/A
113.5	0	N/A	N/A	3	3.61	0.43	N/A	N/A

REFERENCES

Adkins, J. F. (2002). The Salinity, Temperature, and delta 18O of the Glacial Deep Ocean. *Science*, *298*(5599), 1769–1773. https://doi.org/10.1126/science.1076252

Ai, X. E., Studer, A. S., Sigman, D. M., Martínez-García, A., Fripiat, F., Thöle, L. M., Michel, E., Gottschalk, J., Arnold, L., Moretti, S., Schmitt, M., Oleynik, S., Jaccard, S. L., & Haug, G. H. (2020). Southern Ocean upwelling, Earth's obliquity, and glacial-interglacial atmospheric CO_2 change. *Science*, *370*(6522), 1348–1352. https://doi.org/10.1126/science.abd2115

Allen, C. S., Pike, J., & Pudsey, C. J. (2011). Last glacial–interglacial sea-ice cover in the SW Atlantic and its potential role in global deglaciation. *Quaternary Science Reviews*, *30*(19), 2446–2458. https://doi.org/10.1016/j.quascirev.2011.04.002

Allen, K. A., Sikes, E. L., Anderson, R. F., & Rosenthal, Y. (2020). Rapid Loss of CO_2 From the South Pacific Ocean During the Last Glacial Termination. *Paleoceanography and Paleoclimatology*, *35*(2), e2019PA003766. https://doi.org/10.1029/2019PA003766

Anderson, D. M., & Prell, W. L. (1993). A 300 KYR Record of Upwelling Off Oman during the Late Quaternary: Evidence of the Asian Southwest Monsoon. *Paleoceanography*, *8*(2), 193–208. https://doi.org/10.1029/93PA00256

Anderson, L. A., & Sarmiento, J. L. (1994). Redfield ratios of remineralization determined by nutrient data analysis. *Global Biogeochemical Cycles*, *8*(1), 65–80. https://doi.org/10.1029/93GB03318

Anderson, R. F., Sachs, J. P., Fleisher, M. Q., Allen, K. A., Yu, J., Koutavas, A., & Jaccard, S. L. (2019). Deep-Sea Oxygen Depletion and Ocean Carbon Sequestration During the Last Ice Age. *Global Biogeochemical Cycles*, *33*(3), 301–317. https://doi.org/10.1029/2018GB006049

Archer, D. E., Eshel, G., Winguth, A., Broecker, W., Pierrehumbert, R., Tobis, M., & Jacob, R. (2000). Atmospheric *p* CO_2 sensitivity to the biological pump in the ocean. *Global Biogeochemical Cycles*, *14*(4), 1219–1230. https://doi.org/10.1029/1999GB001216

Archer, D., Winguth, A., Lea, D., & Mahowald, N. (2000). What caused the glacial/interglacial atmospheric *p* CO_2 cycles? *Reviews of Geophysics*, *38*(2), 159–189. https://doi.org/10.1029/1999RG000066

Bereiter, B., Shackleton, S., Baggenstos, D., Kawamura, K., & Severinghaus, J. (2018). Mean global ocean temperatures during the last glacial transition. *Nature*, *553*(7686), 39–44. https://doi.org/10.1038/nature25152

Boyer, T. P., Antonov, J. I., Baranova, O. K., Garcia, H. E., Johnson, D. R., Mishonov, A. V., O'Brien, T. D., Seidov, D., I. (Igor), S., Zweng, M. M., Paver, C. R., Locarnini,

R. A., Reagan, J. R., Coleman, C., & Grodsky, A. (2013). *World ocean database 2013*. https://doi.org/10.7289/v5nz85mt

Boyle, E. A. (1988). Cadmium: Chemical tracer of deepwater paleoceanography. *Paleoceanography*, *3*(4), 471–489. https://doi.org/10.1029/PA003i004p00471

Boyle, E. A. (1992). Cadmium and delta13C Paleochemical Ocean Distributions During the Stage 2 Glacial Maximum. *Annual Review of Earth and Planetary Sciences*, *20*(1), 245–287. https://doi.org/10.1146/annurev.ea.20.050192.001333

Boyle, E. A., & Keigwin, L. (1987). North Atlantic thermohaline circulation during the past 20,000 years linked to high-latitude surface temperature. *Nature*, *330*(6143), 35–40. https://doi.org/10.1038/330035a0

Boyle, E. A., Labeyrie, L., & Duplessly, J.-C. (1995). Calcitic foraminiferal data confirmed by cadmium in aragonitic *Hoeglundina*: Application to the Last Glacial Maximum in the northern Indian Ocean. *Paleoceanography*, *10*(5), 881–900. https://doi.org/10.1029/95PA01625

Bradtmiller, L. I., Anderson, R. F., Sachs, J. P., & Fleisher, M. Q. (2010). A deeper respired carbon pool in the glacial equatorial Pacific Ocean. *Earth and Planetary Science Letters*, *299*(3–4), 417–425. https://doi.org/10.1016/j.epsl.2010.09.022

Bradtmiller, L. I., McManus, J. F., & Robinson, L. F. (2014). 231Pa/230Th evidence for a weakened but persistent Atlantic meridional overturning circulation during Heinrich Stadial 1. *Nature Communications*, *5*(1), 5817. https://doi.org/10.1038/ncomms6817

Broecker, W. S., & Maier-Reimer, E. (1992). The influence of air and sea exchange on the carbon isotope distribution in the sea. *Global Biogeochemical Cycles*, *6*(3), 315–320. https://doi.org/10.1029/92GB01672

Burckle, L. H., Robinson, D., & Cooke, D. (1982). Reappraisal of sea-ice distribution in Atlantic and Pacific sectors of the Southern Ocean at 18,000 yr BP. *Nature*, *299*(5882), Article 5882. https://doi.org/10.1038/299435a0

Chavaillaz, Y., Codron, F., & Kageyama, M. (2013). Southern westerlies in LGM and future (RCP4.5) climates. *Climate of the Past*, *9*(2), 517–524. https://doi.org/10.5194/cp-9-517-2013

Chen, C., & Wang, G. (2021). Simulated Southern Ocean Upwelling at the Last Glacial Maximum and Early Deglaciation: The Role of Eddy-Induced Overturning Circulation. *Geophysical Research Letters*, *48*(9), e2021GL092880. https://doi.org/10.1029/2021GL092880

Chen, Y., Speich, S., & Laxenaire, R. (2022). Formation and Transport of the South Atlantic Subtropical Mode Water in Eddy-Permitting Observations. *Journal of*

Geophysical Research: Oceans, *127*(1), e2021JC017767. https://doi.org/10.1029/2021JC017767

Ciais, P., Tagliabue, A., Cuntz, M., Bopp, L., Scholze, M., Hoffmann, G., Lourantou, A., Harrison, S. P., Prentice, I. C., Kelley, D. I., Koven, C., & Piao, S. L. (2012). Large inert carbon pool in the terrestrial biosphere during the Last Glacial Maximum. *Nature Geoscience*, *5*(1), 74–79. https://doi.org/10.1038/ngeo1324

Clark, P. U., & Mix, A. C. (2002). Ice sheets and sea level of the Last Glacial Maximum. *Quaternary Science Reviews*, *21*(1–3), 1–7. https://doi.org/10.1016/S0277-3791(01)00118-4

Cliff, E., Khatiwala, S., & Schmittner, A. (2021). Glacial deep ocean deoxygenation driven by biologically mediated air–sea disequilibrium. *Nature Geoscience*, *14*(1), 43–50. https://doi.org/10.1038/s41561-020-00667-z

CLIMAP PROJECT MEMBERS. (1976). The Surface of the Ice-Age Earth. *Science*, *191*(4232), 1131–1137. https://doi.org/10.1126/science.191.4232.1131

Costa, K. M., Jacobel, A. W., McManus, J. F., Anderson, R. F., Winckler, G., & Thiagarajan, N. (2017). Productivity patterns in the equatorial Pacific over the last 30,000 years. *Global Biogeochemical Cycles*, *31*(5), 850–865. https://doi.org/10.1002/2016GB005579

Crosta, X., Pichon, J.-J., & Burckle, L. H. (1998). Application of modern analog technique to marine Antarctic diatoms: Reconstruction of maximum sea-ice extent at the Last Glacial Maximum. *Paleoceanography*, *13*(3), 284–297. https://doi.org/10.1029/98PA00339

De Baar, H. J. W., Boyd, P. W., Coale, K. H., Landry, M. R., Tsuda, A., Assmy, P., Bakker, D. C. E., Bozec, Y., Barber, R. T., Brzezinski, M. A., Buesseler, K. O., Boyé, M., Croot, P. L., Gervais, F., Gorbunov, M. Y., Harrison, P. J., Hiscock, W. T., Laan, P., Lancelot, C., … Wong, C. (2005). Synthesis of iron fertilization experiments: From the Iron Age in the Age of Enlightenment. *Journal of Geophysical Research: Oceans*, *110*(C9), 2004JC002601. https://doi.org/10.1029/2004JC002601

Dubois, N., Kienast, M., Kienast, S., Normandeau, C., Calvert, S. E., Herbert, T. D., & Mix, A. (2011). Millennial-scale variations in hydrography and biogeochemistry in the Eastern Equatorial Pacific over the last 100 kyr. *Quaternary Science Reviews*, *30*(1–2), 210–223. https://doi.org/10.1016/j.quascirev.2010.10.012

Durand, A., Chase, Z., Noble, T. L., Bostock, H., Jaccard, S. L., Townsend, A. T., Bindoff, N. L., Neil, H., & Jacobsen, G. (2018). Reduced oxygenation at intermediate depths of the southwest Pacific during the last glacial maximum. *Earth and Planetary Science Letters*, *491*, 48–57. https://doi.org/10.1016/j.epsl.2018.03.036

Dutkiewicz, S., Follows, M. J., Heimbach, P., & Marshall, J. (2006). Controls on ocean productivity and air-sea carbon flux: An adjoint model sensitivity study. *Geophysical Research Letters*, *33*(2), L02603. https://doi.org/10.1029/2005GL024987

Elderfield, H., & Rickaby, R. E. M. (2000). Oceanic Cd/P ratio and nutrient utilization in the glacial Southern Ocean. *Nature*, *405*(6784), 305–310. https://doi.org/10.1038/35012507

Elmore, A. C., McClymont, E. L., Elderfield, H., Kender, S., Cook, M. R., Leng, M. J., Greaves, M., & Misra, S. (2015). Antarctic Intermediate Water properties since 400 ka recorded in infaunal (Uvigerina peregrina) and epifaunal (Planulina wuellerstorfi) benthic foraminifera. *Earth and Planetary Science Letters*, *428*, 193–203. https://doi.org/10.1016/j.epsl.2015.07.013

EPICA community members. (2004). Eight glacial cycles from an Antarctic ice core. *Nature*, *429*(6992), 623–628. https://doi.org/10.1038/nature02599

Erdem, Z., Schönfeld, J., Rathburn, A. E., Pérez, M.-E., Cardich, J., & Glock, N. (2020). Bottom-water deoxygenation at the Peruvian margin during the last deglaciation recorded by benthic foraminifera. *Biogeosciences*, *17*(12), 3165–3182. https://doi.org/10.5194/bg-17-3165-2020

Fairbanks, R. G. (1989). A 17,000-year glacio-eustatic sea level record: Influence of glacial melting rates on the Younger Dryas event and deep-ocean circulation. *Nature*, *342*(6250), 637–642. https://doi.org/10.1038/342637a0

Ferreira, D., Marshall, J., Ito, T., & McGee, D. (2018). Linking Glacial-Interglacial States to Multiple Equilibria of Climate. *Geophysical Research Letters*, *45*(17), 9160–9170. https://doi.org/10.1029/2018GL077019

Franois, R., Altabet, M. A., Yu, E.-F., Sigman, D. M., Bacon, M. P., Frank, M., Bohrmann, G., Bareille, G., & Labeyrie, L. D. (1997). Contribution of Southern Ocean surface-water stratification to low atmospheric CO2 concentrations during the last glacial period. *Nature*, *389*(6654), 929–935. https://doi.org/10.1038/40073

Freeman, E., Skinner, L. C., Waelbroeck, C., & Hodell, D. (2016). Radiocarbon evidence for enhanced respired carbon storage in the Atlantic at the Last Glacial Maximum. *Nature Communications*, *7*(1), 11998. https://doi.org/10.1038/ncomms11998

Ganopolski, A., & Brovkin, V. (2017). Simulation of climate, ice sheets and CO2; evolution during the last four glacial cycles with an Earth system model of intermediate complexity. *Climate of the Past*, *13*(12), 1695–1716. https://doi.org/10.5194/cp-13-1695-2017

Garzoli, S. L., & Gordon, A. L. (1996). Origins and variability of the Benguela Current. *Journal of Geophysical Research: Oceans*, *101*(C1), 897–906. https://doi.org/10.1029/95JC03221

Gebbie, G. (2014). How much did Glacial North Atlantic Water shoal? *Paleoceanography*, *29*(3), 190–209. https://doi.org/10.1002/2013PA002557

Gebbie, G., Peterson, C. D., Lisiecki, L. E., & Spero, H. J. (2015). Global-mean marine δ13C and its uncertainty in a glacial state estimate. *Quaternary Science Reviews*, *125*, 144–159. https://doi.org/10.1016/j.quascirev.2015.08.010

Gersonde, R., Abelmann, A., Brathauer, U., Becquey, S., Bianchi, C., Cortese, G., Grobe, H., Kuhn, G., Niebler, H.-S., Segl, M., Sieger, R., Zielinski, U., & Fütterer, D. K. (2003). Last glacial sea surface temperatures and sea-ice extent in the Southern Ocean (Atlantic-Indian sector): A multiproxy approach. *Paleoceanography, 18*(3). https://doi.org/10.1029/2002PA000809

Glock, N., Erdem, Z., & Schönfeld, J. (2022). The Peruvian oxygen minimum zone was similar in extent but weaker during the Last Glacial Maximum than Late Holocene. *Communications Earth & Environment*, *3*(1), 307. https://doi.org/10.1038/s43247-022-00635-y

Glock, N., Liebetrau, V., & Eisenhauer, A. (2014). I/Ca ratios in benthic foraminifera from the Peruvian oxygen minimum zone: Analytical methodology and evaluation as a proxy for redox conditions. *Biogeosciences*, *11*(23), 7077–7095. https://doi.org/10.5194/bg-11-7077-2014

Gottschalk, J., Skinner, L. C., Lippold, J., Vogel, H., Frank, N., Jaccard, S. L., & Waelbroeck, C. (2016). Biological and physical controls in the Southern Ocean on past millennial-scale atmospheric CO2 changes. *Nature Communications*, *7*(1), 11539. https://doi.org/10.1038/ncomms11539

Gottschalk, J., Vázquez Riveiros, N., Waelbroeck, C., Skinner, L. C., Michel, E., Duplessy, J.-C., Hodell, D., & Mackensen, A. (2016). Carbon isotope offsets between benthic foraminifer species of the genus *Cibicides* (*Cibicidoides*) in the glacial sub-Antarctic. *Paleoceanography*, *31*(12), 1583–1602. https://doi.org/10.1002/2016PA003029

Gupta, A. K., Mohan, K., Sarkar, S., Clemens, S. C., Ravindra, R., & Uttam, R. K. (2011). East–West similarities and differences in the surface and deep northern Arabian Sea records during the past 21Kyr. *Palaeogeography, Palaeoclimatology, Palaeoecology*, *301*(1–4), 75–85. https://doi.org/10.1016/j.palaeo.2010.12.027

Hain, M. P., Sigman, D. M., & Haug, G. H. (2010). Carbon dioxide effects of Antarctic stratification, North Atlantic Intermediate Water formation, and subantarctic nutrient drawdown during the last ice age: Diagnosis and synthesis in a geochemical box model. *Global Biogeochemical Cycles*, *24*(4), n/a-n/a. https://doi.org/10.1029/2010GB003790

Hays, J. D., Lozano, J. A., Shackleton, N., & Irving, G. (1976). *Reconstruction of the Atlantic and Western Indian Ocean Sectors of the 18,000 B.P. Antarctic Ocean*. https://doi.org/10.1130/MEM145-p337

Headly, M. A., & Severinghaus, J. P. (2007). A method to measure Kr/N_2 ratios in air bubbles trapped in ice cores and its application in reconstructing past mean ocean temperature. *Journal of Geophysical Research*, *112*(D19), D19105. https://doi.org/10.1029/2006JD008317

Hoogakker, B. A. A., Elderfield, H., Schmiedl, G., McCave, I. N., & Rickaby, R. E. M. (2015). Glacial–interglacial changes in bottom-water oxygen content on the Portuguese margin. *Nature Geoscience*, *8*(1), 40–43. https://doi.org/10.1038/ngeo2317

Hoogakker, B. A. A., Lu, Z., Umling, N., Jones, L., Zhou, X., Rickaby, R. E. M., Thunell, R., Cartapanis, O., & Galbraith, E. (2018). Glacial expansion of oxygen-depleted seawater in the eastern tropical Pacific. *Nature*, *562*(7727), 410–413. https://doi.org/10.1038/s41586-018-0589-x

Ito, T., & Follows, M. J. (2005). Preformed phosphate, soft tissue pump and atmospheric CO2. *Journal of Marine Research*, *63*(4), 813–839. https://doi.org/10.1357/0022240054663231

Ito, T., & Follows, M. J. (2013). Air-sea disequilibrium of carbon dioxide enhances the biological carbon sequestration in the Southern Ocean. *Global Biogeochemical Cycles*, *27*(4), 1129–1138. https://doi.org/10.1002/2013GB004682

Ito, T., Follows, M. J., & Boyle, E. A. (2004). Is AOU a good measure of respiration in the oceans?. *Geophysical Research Letters*, *31*(17), n/a-n/a. https://doi.org/10.1029/2004GL020900

Ivanochko, T., Ganeshram, R., Brummer, G., Ganssen, G., Jung, S., Moreton, S., & Kroon, D. (2005). Variations in tropical convection as an amplifier of global climate change at the millennial scale. *Earth and Planetary Science Letters*, *235*(1–2), 302–314. https://doi.org/10.1016/j.epsl.2005.04.002

Jaccard, S. L., & Galbraith, E. D. (2012). Large climate-driven changes of oceanic oxygen concentrations during the last deglaciation. *Nature Geoscience*, *5*(2), 151–156. https://doi.org/10.1038/ngeo1352

Jaccard, S. L., Galbraith, E. D., Martínez-García, A., & Anderson, R. F. (2016). Covariation of deep Southern Ocean oxygenation and atmospheric CO2 through the last ice age. *Nature*, *530*(7589), 207–210. https://doi.org/10.1038/nature16514

Jacobel, A. W., Anderson, R. F., Jaccard, S. L., McManus, J. F., Pavia, F. J., & Winckler, G. (2020). Deep Pacific storage of respired carbon during the last ice age: Perspectives from bottom water oxygen reconstructions. *Quaternary Science Reviews*, *230*, 106065. https://doi.org/10.1016/j.quascirev.2019.106065

Jorissen, F. J., Fontanier, C., & Thomas, E. (2007). Chapter Seven Paleoceanographical Proxies Based on Deep-Sea Benthic Foraminiferal Assemblage Characteristics. In *Developments in Marine Geology* (Vol. 1, pp. 263–325). Elsevier. https://doi.org/10.1016/S1572-5480(07)01012-3

Jorissen, F. J., Wittling, I., Peypouquet, J. P., Rabouille, C., & Relexans, J. C. (1998). Live benthic foraminiferal faunas off Cape Blanc, NW-Africa: Community structure and microhabitats. *Deep Sea Research Part I: Oceanographic Research Papers*, *45*(12), 2157–2188. https://doi.org/10.1016/S0967-0637(98)00056-9

Jung, S. J. A., Davies, G. R., Ganssen, G., & Kroon, D. (2002). Decadal-centennial scale monsoon variations in the Arabian Sea during the Early Holocene. *Geochemistry, Geophysics, Geosystems*, *3*(10), 1–10. https://doi.org/10.1029/2002GC000348

Kaiho, K. (1994). Benthic foraminiferal dissolved-oxygen index and dissolved-oxygen levels in the modern ocean. *Geology*, *22*(8), 719. https://doi.org/10.1130/0091-7613(1994)022<0719:BFDOIA>2.3.CO;2

Kanzaki, Y., Hülse, D., Kirtland Turner, S., & Ridgwell, A. (2021). A model for marine sedimentary carbonate diagenesis and paleoclimate proxy signal tracking: IMP v1.0. *Geoscientific Model Development*, *14*(10), 5999–6023. https://doi.org/10.5194/gmd-14-5999-2021

Keir, R. S. (1988). On the Late Pleistocene ocean geochemistry and circulation. *Paleoceanography, 3*(4), 413–445. https://doi.org/10.1029/PA003i004p00413

Kemeny, P. C., Kast, E. R., Hain, M. P., Fawcett, S. E., Fripiat, F., Studer, A. S., Martínez-García, A., Haug, G. H., & Sigman, D. M. (2018). A Seasonal Model of Nitrogen Isotopes in the Ice Age Antarctic Zone: Support for Weakening of the Southern Ocean Upper Overturning Cell. *Paleoceanography and Paleoclimatology*, *33*(12), 1453–1471. https://doi.org/10.1029/2018PA003478

Khatiwala, S., Schmittner, A., & Muglia, J. (2019). Air-sea disequilibrium enhances ocean carbon storage during glacial periods. *Science Advances*, *5*(6). https://doi.org/10.1126/sciadv.aaw4981

Kim, G. Y., Lynch-Stieglitz, J., Ito, T., Reinhard, C.T. (2023). *Decreased dissolved oxygen content of the Pacific Deep Water during the Last Glacial Maximum (Master's Thesis). Georgia Institute of Technology, Atlanta, Georgia.*

Knox, F., & McElroy, M. B. (1984). Changes in atmospheric CO2: Influence of the marine biota at high latitude. *Journal of Geophysical Research*, *89*(D3), 4629. https://doi.org/10.1029/JD089iD03p04629

Kohfeld, K. E., Graham, R. M., de Boer, A. M., Sime, L. C., Wolff, E. W., Le Quéré, C., & Bopp, L. (2013). Southern Hemisphere westerly wind changes during the Last Glacial Maximum: Paleo-data synthesis. *Quaternary Science Reviews*, *68*, 76–95. https://doi.org/10.1016/j.quascirev.2013.01.017

Kohfeld Karen E., Quéré Corinne Le, Harrison Sandy P., & Anderson Robert F. (2005). Role of Marine Biology in Glacial-Interglacial CO2 Cycles. *Science*, *308*(5718), 74–78. https://doi.org/10.1126/science.1105375

Koutavas, A., & Lynch-Stieglitz, J. (2003). Glacial-interglacial dynamics of the eastern equatorial Pacific cold tongue-Intertropical Convergence Zone system reconstructed from oxygen isotope records. *Paleoceanography*, *18*(4), 2003PA000894. https://doi.org/10.1029/2003PA000894

Kumar, N., Anderson, R. F., Mortlock, R. A., Froelich, P. N., Kubik, P., Dittrich-Hannen, B., & Suter, M. (1995). Increased biological productivity and export production in the glacial Southern Ocean. *Nature*, *378*(6558), 675–680. https://doi.org/10.1038/378675a0

Lamont, T., Hutchings, L., Van Den Berg, M. A., Goschen, W. S., & Barlow, R. G. (2015). Hydrographic variability in the S t. Helena Bay region of the southern Benguela ecosystem. *Journal of Geophysical Research: Oceans*, *120*(4), 2920–2944. https://doi.org/10.1002/2014JC010619

Lippold, J., Luo, Y., Francois, R., Allen, S. E., Gherardi, J., Pichat, S., Hickey, B., & Schulz, H. (2012). Strength and geometry of the glacial Atlantic Meridional Overturning Circulation. *Nature Geoscience*, *5*(11), 813–816. https://doi.org/10.1038/ngeo1608

Long, A. M., Jurgensen, S. K., Petchel, A. R., Savoie, E. R., & Brum, J. R. (2021). Microbial Ecology of Oxygen Minimum Zones Amidst Ocean Deoxygenation. *Frontiers in Microbiology*, *12*, 748961. https://doi.org/10.3389/fmicb.2021.748961

Lu, W., Barbosa, C. F., Rathburn, A. E., Xavier, P. D. M., Cruz, A. P. S., Thomas, E., Rickaby, R. E. M., Zhang, Y. G., & Lu, Z. (2021). Proxies for paleo-oxygenation: A downcore comparison between benthic foraminiferal surface porosity and I/Ca. *Palaeogeography, Palaeoclimatology, Palaeoecology*, *579*, 110588. https://doi.org/10.1016/j.palaeo.2021.110588

Lu, W., Costa, K. M., & Oppo, D. W. (2023). Reconstructing the Oxygen Depth Profile in the Arabian Sea During the Last Glacial Period. *Paleoceanography and Paleoclimatology*, *38*(6), e2023PA004632. https://doi.org/10.1029/2023PA004632

Lu, W., Dickson, A. J., Thomas, E., Rickaby, R. E. M., Chapman, P., & Lu, Z. (2020). Refining the planktic foraminiferal I/Ca proxy: Results from the Southeast Atlantic Ocean. *Geochimica et Cosmochimica Acta*, *287*, 318–327. https://doi.org/10.1016/j.gca.2019.10.025

Lu, W., Rickaby, R. E., Hoogakker, B. A., Rathburn, A. E., Burkett, A. M., Dickson, A. J., Martínez-Méndez, G., Hillenbrand, C.-D., Zhou, X., & Thomas, E. (2020). I/Ca in epifaunal benthic foraminifera: A semi-quantitative proxy for bottom water oxygen in a multi-proxy compilation for glacial ocean deoxygenation. *Earth and Planetary Science Letters*, *533*, 116055.

Lu, W., Wang, Y., Oppo, D. W., Nielsen, S. G., & Costa, K. M. (2022). Comparing paleo-oxygenation proxies (benthic foraminiferal surface porosity, I/Ca, authigenic uranium) on modern sediments and the glacial Arabian Sea. *Geochimica et Cosmochimica Acta*, *331*, 69–85. https://doi.org/10.1016/j.gca.2022.06.001

Lund, D. C., Chase, Z., Kohfeld, K. E., & Wilson, E. A. (2021). Tracking Southern Ocean Sea Ice Extent With Winter Water: A New Method Based on the Oxygen Isotopic Signature of Foraminifera. *Paleoceanography and Paleoclimatology*, *36*(6), e2020PA004095. https://doi.org/10.1029/2020PA004095

Lynch-Stieglitz, J., Adkins, J. F., Curry, W. B., Dokken, T., Hall, I. R., Herguera, J. C., Hirschi, J. J.-M., Ivanova, E. V., Kissel, C., Marchal, O., Marchitto, T. M., McCave,

I. N., McManus, J. F., Mulitza, S., Ninnemann, U., Peeters, F., Yu, E.-F., & Zahn, R. (2007). Atlantic Meridional Overturning Circulation During the Last Glacial Maximum. *Science, 316*(5821), 66–69. https://doi.org/10.1126/science.1137127

Lynch-Stieglitz, J., Curry, W. B., Oppo, D. W., Ninneman, U. S., Charles, C. D., & Munson, J. (2006). Meridional overturning circulation in the South Atlantic at the last glacial maximum. *Geochemistry, Geophysics, Geosystems*, *7*(10), 2005GC001226. https://doi.org/10.1029/2005GC001226

Lynch-Stieglitz, J., Fairbanks, R. G., & Charles, C. D. (1994). Glacial-interglacial history of Antarctic Intermediate Water: Relative strengths of Antarctic versus Indian Ocean sources. *Paleoceanography*, *9*(1), 7–29. https://doi.org/10.1029/93PA02446

Lynch-Stieglitz, J., Van Geen, A., & Fairbanks, R. G. (1996). Interocean exchange of glacial North Atlantic Intermediate Water: Evidence from subantarctic Cd/Ca and carbon isotope measurements. *Paleoceanography*, *11*(2), 191–201. https://doi.org/10.1029/95PA03772

Mackensen, A., & Licari, L. (2003). Carbon Isotopes of Live Benthic Foraminifera from the South Atlantic: Sensitivity to Bottom Water Carbonate Saturation State and Organic Matter Rain Rates. In G. Wefer, S. Mulitza, & V. Ratmeyer (Eds.), *The South Atlantic in the Late Quaternary* (pp. 623–644). Springer Berlin Heidelberg. https://doi.org/10.1007/978-3-642-18917-3_27

Marchitto, T. M., & Broecker, W. S. (2006). Deep water mass geometry in the glacial Atlantic Ocean: A review of constraints from the paleonutrient proxy Cd/Ca. *Geochemistry, Geophysics, Geosystems*, *7*(12), n/a-n/a. https://doi.org/10.1029/2006GC001323

Marchitto, T. M., Oppo, D. W., & Curry, W. B. (2002). Paired benthic foraminiferal Cd/Ca and Zn/Ca evidence for a greatly increased presence of Southern Ocean Water in the glacial North Atlantic. *Paleoceanography*, *17*(3), 10-1-10–18. https://doi.org/10.1029/2000PA000598

Marinov, I., Gnanadesikan, A., Sarmiento, J. L., Toggweiler, J. R., Follows, M., & Mignone, B. K. (2008). Impact of oceanic circulation on biological carbon storage in the ocean and atmospheric pCO2. *Global Biogeochemical Cycles*, *22*(3). https://doi.org/10.1029/2007GB002958

Marshall, J., Adcroft, A., Hill, C., Perelman, L., & Heisey, C. (1997). A finite-volume, incompressible Navier Stokes model for studies of the ocean on parallel computers. *Journal of Geophysical Research: Oceans*, *102*(C3), 5753–5766. https://doi.org/10.1029/96JC02775

Marshall, J., Hill, C., Perelman, L., & Adcroft, A. (1997). Hydrostatic, quasi-hydrostatic, and nonhydrostatic ocean modeling. *Journal of Geophysical Research: Oceans*, *102*(C3), 5733–5752. https://doi.org/10.1029/96JC02776

Martin, J. H. (1990). Glacial-interglacial CO_2 change: The Iron Hypothesis. *Paleoceanography*, *5*(1), 1–13. https://doi.org/10.1029/PA005i001p00001

Martin, J. H., Fitzwater, S. E., & Gordon, R. M. (1990). Iron deficiency limits phytoplankton growth in Antarctic waters. *Global Biogeochemical Cycles*, *4*(1), 5–12. https://doi.org/10.1029/GB004i001p00005

Martin, J. H., Knauer, G. A., Karl, D. M., & Broenkow, W. W. (1987). VERTEX: Carbon cycling in the northeast Pacific. *Deep Sea Research Part A. Oceanographic Research Papers*, *34*(2), 267–285. https://doi.org/10.1016/0198-0149(87)90086-0

Martin, P., Archer, D., & Lea, D. W. (2005). Role of deep sea temperature in the carbon cycle during the last glacial: TEMPERATURE AND GLACIAL CO_2. *Paleoceanography*, *20*(2), n/a-n/a. https://doi.org/10.1029/2003PA000914

Martínez-García, A., Sigman, D. M., Ren, H., Anderson, R. F., Straub, M., Hodell, D. A., Jaccard, S. L., Eglinton, T. I., & Haug, G. H. (2014). Iron Fertilization of the Subantarctic Ocean During the Last Ice Age. *Science*, *343*(6177), 1347–1350. https://doi.org/10.1126/science.1246848

Marzocchi, A., & Jansen, M. F. (2019). Global cooling linked to increased glacial carbon storage via changes in Antarctic sea ice. *Nature Geoscience*, *12*(12), 1001–1005. https://doi.org/10.1038/s41561-019-0466-8

Matsumoto, K., Oba, T., Lynch-Stieglitz, J., & Yamamoto, H. (2002). Interior hydrography and circulation of the glacial Pacific Ocean. *Quaternary Science Reviews*, *21*(14–15), 1693–1704. https://doi.org/10.1016/S0277-3791(01)00142-1

McCorkle, D. C., & Emerson, S. R. (1988). The relationship between pore water carbon isotopic composition and bottom water oxygen concentration. *Geochimica et Cosmochimica Acta*, *52*(5), 1169–1178. https://doi.org/10.1016/0016-7037(88)90270-0

McCorkle, D. C., Keigwin, L. D., Corliss, B. H., & Emerson, S. R. (1990). The influence of microhabitats on the carbon isotopic composition of deep-sea benthic foraminifera. *Paleoceanography*, *5*(2), 161–185. https://doi.org/10.1029/PA005i002p00161

Mojtahid, M., Toucanne, S., Fentimen, R., Barras, C., Le Houedec, S., Soulet, G., Bourillet, J.-F., & Michel, E. (2017). Changes in northeast Atlantic hydrology during Termination 1: Insights from Celtic margin's benthic foraminifera. *Quaternary Science Reviews*, *175*, 45–59. https://doi.org/10.1016/j.quascirev.2017.09.003

Mollenhauer, G., Schneider, R. R., Müller, P. J., Spieß, V., & Wefer, G. (2002). Glacial/interglacial variablity in the Benguela upwelling system: Spatial distribution and budgets of organic carbon accumulation. *Global Biogeochemical Cycles*, *16*(4). https://doi.org/10.1029/2001GB001488

Mortlock, R. A., Charles, C. D., Froelich, P. N., Zibello, M. A., Saltzman, J., Hays, J. D., & Burckle, L. H. (1991). Evidence for lower productivity in the Antarctic Ocean during the last glaciation. *Nature*, *351*(6323), 220–223. https://doi.org/10.1038/351220a0

Naidu, P. D., & Malmgren, B. A. (1996). A High-resolution record of Late Quaternary upwelling along the Oman Margin, Arabian Sea based on planktonic foraminifera. *Paleoceanography*, *11*(1), 129–140. https://doi.org/10.1029/95PA03198

Ohkushi, K., Kennett, J. P., Zeleski, C. M., Moffitt, S. E., Hill, T. M., Robert, C., Beaufort, L., & Behl, R. J. (2013). Quantified intermediate water oxygenation history of the NE Pacific: A new benthic foraminiferal record from Santa Barbara basin. *Paleoceanography*, *28*(3), 453–467. https://doi.org/10.1002/palo.20043

Oppo, D. W., Gebbie, G., Huang, K.-F., Curry, W. B., Marchitto, T. M., & Pietro, K. R. (2018). Data Constraints on Glacial Atlantic Water Mass Geometry and Properties. *Paleoceanography and Paleoclimatology*, *33*(9), 1013–1034. https://doi.org/10.1029/2018PA003408

Oppo, D. W., & Lehman, S. J. (1993). Mid-Depth Circulation of the Subpolar North Atlantic During the Last Glacial Maximum. *Science*, *259*(5098), 1148–1152. https://doi.org/10.1126/science.259.5098.1148

Peterson, C. D., Lisiecki, L. E., & Stern, J. V. (2014). Deglacial whole-ocean δ13C change estimated from 480 benthic foraminiferal records. *Paleoceanography*, *29*(6), 549–563. https://doi.org/10.1002/2013PA002552

Petit, J. R., Jouzel, J., Raynaud, D., Barkov, N. I., Barnola, J.-M., Basile, I., Bender, M., Chappellaz, J., Davis, M., Delaygue, G., Delmotte, M., Kotlyakov, V. M., Legrand, M., Lipenkov, V. Y., Lorius, C., PÉpin, L., Ritz, C., Saltzman, E., & Stievenard, M. (1999). Climate and atmospheric history of the past 420,000 years from the Vostok ice core, Antarctica. *Nature*, *399*(6735), 429–436. https://doi.org/10.1038/20859

Rae, J. W. B., Sarnthein, M., Foster, G. L., Ridgwell, A., Grootes, P. M., & Elliott, T. (2014). Deep water formation in the North Pacific and deglacial CO_2 rise: N Pacific deep water and deglacial CO2. *Paleoceanography*, *29*(6), 645–667. https://doi.org/10.1002/2013PA002570

Rafter, P. A., Gray, W. R., Hines, S. K. V., Burke, A., Costa, K. M., Gottschalk, J., Hain, M. P., Rae, J. W. B., Southon, J. R., Walczak, M. H., Yu, J., Adkins, J. F., & DeVries, T. (2022). Global reorganization of deep-sea circulation and carbon storage after the last ice age. *Science Advances*, *8*(46), eabq5434. https://doi.org/10.1126/sciadv.abq5434

Rathburn, A. E., Willingham, J., Ziebis, W., Burkett, A. M., & Corliss, B. H. (2018). A New biological proxy for deep-sea paleo-oxygen: Pores of epifaunal benthic foraminifera. *Scientific Reports*, *8*(1), 1–8.

Ridgwell, A. J., & Watson, A. J. (2002). Feedback between aeolian dust, climate, and atmospheric CO $_2$ in glacial time. *Paleoceanography*, *17*(4), 11-1-11–11. https://doi.org/10.1029/2001PA000729

Roberts, J., Gottschalk, J., Skinner, L. C., Peck, V. L., Kender, S., Elderfield, H., Waelbroeck, C., Vázquez Riveiros, N., & Hodell, D. A. (2016). Evolution of South Atlantic density and chemical stratification across the last deglaciation. *Proceedings of the National Academy of Sciences*, *113*(3), 514–519. https://doi.org/10.1073/pnas.1511252113

Robinson, R. S., Martinez, P., Pena, L. D., & Cacho, I. (2009). Nitrogen isotopic evidence for deglacial changes in nutrient supply in the eastern equatorial Pacific. *Paleoceanography*, *24*(4), 2008PA001702. https://doi.org/10.1029/2008PA001702

Robinson, R. S., Sigman, D. M., DiFiore, P. J., Rohde, M. M., Mashiotta, T. A., & Lea, D. W. (2005). Diatom-bound $^{15}N/^{14}N$: New support for enhanced nutrient consumption in the ice age subantarctic. *Paleoceanography*, *20*(3), n/a-n/a. https://doi.org/10.1029/2004PA001114

Rosenthal, Y., Boyle, E. A., & Slowey, N. (1997). Temperature control on the incorporation of magnesium, strontium, fluorine, and cadmium into benthic foraminiferal shells from Little Bahama Bank: Prospects for thermocline paleoceanography. *Geochimica et Cosmochimica Acta*, *61*(17), 3633–3643. https://doi.org/10.1016/S0016-7037(97)00181-6

Sarmiento, J. L., & Gruber, N. (2006). *Ocean biogeochemical dynamics*. Princeton University Press.

Sarmiento, J. L., & Toggweiler, J. R. (1984). A new model for the role of the oceans in determining atmospheric P CO2. *Nature*, *308*(5960), 621–624. https://doi.org/10.1038/308621a0

Schmiedl, G., & Mackensen, A. (2006). Multispecies stable isotopes of benthic foraminifers reveal past changes of organic matter decomposition and deepwater oxygenation in the Arabian Sea. *Paleoceanography*, *21*(4). https://doi.org/10.1029/2006PA001284

Scholz, F., McManus, J., Mix, A. C., Hensen, C., & Schneider, R. R. (2014). The impact of ocean deoxygenation on iron release from continental margin sediments. *Nature Geoscience*, *7*(6), 433–437. https://doi.org/10.1038/ngeo2162

Shannon, L. V., & Nelson, G. (1996). The Benguela: Large Scale Features and Processes and System Variability. In G. Wefer, W. H. Berger, G. Siedler, & D. J. Webb, *The*

South Atlantic (pp. 163–210). Springer Berlin Heidelberg. https://doi.org/10.1007/978-3-642-80353-6_9

Siegenthaler, U., & Wenk, Th. (1984). Rapid atmospheric CO2 variations and ocean circulation. *Nature*, *308*(5960), 624–626. https://doi.org/10.1038/308624a0

Sigman, D. M., & Boyle, E. A. (2000). Glacial/interglacial variations in atmospheric carbon dioxide. *Nature*, *407*(6806), 859–869. https://doi.org/10.1038/35038000

Sigman, D. M., Hain, M. P., & Haug, G. H. (2010). The polar ocean and glacial cycles in atmospheric CO2 concentration. *Nature*, *466*(7302), 47–55. https://doi.org/10.1038/nature09149

Singh, A. D., Jung, S. J. A., Darling, K., Ganeshram, R., Ivanochko, T., & Kroon, D. (2011). Productivity collapses in the Arabian Sea during glacial cold phases: MILLENNIAL-SCALE MONSOON VARIATIONS. *Paleoceanography*, *26*(3), n/a-n/a. https://doi.org/10.1029/2009PA001923

Skinner, L. C., Primeau, F., Freeman, E., De La Fuente, M., Goodwin, P. A., Gottschalk, J., Huang, E., McCave, I. N., Noble, T. L., & Scrivner, A. E. (2017). Radiocarbon constraints on the glacial ocean circulation and its impact on atmospheric CO2. *Nature Communications*, *8*(1), 16010. https://doi.org/10.1038/ncomms16010

Skinner, L. C., Shackleton, N. J., & Elderfield, H. (2003). Millennial-scale variability of deep-water temperature and $\delta^{18}O_{dw}$ indicating deep-water source variations in the Northeast Atlantic, 0-34 cal. ka BP. *Geochemistry, Geophysics, Geosystems*, *4*(12). https://doi.org/10.1029/2003GC000585

Stephens, B. B., & Keeling, R. F. (2000). The influence of Antarctic sea ice on glacial–interglacial CO2 variations. *Nature*, *404*(6774), 171–174. https://doi.org/10.1038/35004556

Stramma, L., & England, M. (1999). On the water masses and mean circulation of the South Atlantic Ocean. *Journal of Geophysical Research: Oceans*, *104*(C9), 20863–20883. https://doi.org/10.1029/1999JC900139

Stramma, L., Johnson, G. C., Sprintall, J., & Mohrholz, V. (2008). Expanding Oxygen-Minimum Zones in the Tropical Oceans. *Science*, *320*(5876), 655–658. https://doi.org/10.1126/science.1153847

Studer, A. S., Sigman, D. M., Martínez-García, A., Benz, V., Winckler, G., Kuhn, G., Esper, O., Lamy, F., Jaccard, S. L., Wacker, L., Oleynik, S., Gersonde, R., & Haug, G. H. (2015). Antarctic Zone nutrient conditions during the last two glacial cycles. *Paleoceanography*, *30*(7), 845–862. https://doi.org/10.1002/2014PA002745

Tagliabue, A., Bopp, L., Roche, D. M., Bouttes, N., Dutay, J.-C., Alkama, R., Kageyama, M., Michel, E., & Paillard, D. (2009). Quantifying the roles of ocean circulation and biogeochemistry in governing ocean carbon-13 and atmospheric carbon dioxide at the last glacial maximum. *Climate of the Past*, *5*(4), 695–706. https://doi.org/10.5194/cp-5-695-2009

Tetard, M., Licari, L., & Beaufort, L. (2017). Oxygen history off Baja California over the last 80 kyr: A new foraminiferal-based record: Oxygen History in the California Margin. *Paleoceanography*, *32*(3), 246–264. https://doi.org/10.1002/2016PA003034

Tetard, M., Licari, L., Ovsepyan, E., Tachikawa, K., & Beaufort, L. (2021). Toward a global calibration for quantifying past oxygenation in oxygen minimum zones using benthic Foraminifera. *Biogeosciences*, *18*(9), 2827–2841. https://doi.org/10.5194/bg-18-2827-2021

Toggweiler, J. R., Gnanadesikan, A., Carson, S., Murnane, R., & Sarmiento, J. L. (2003). Representation of the carbon cycle in box models and GCMs: 1. Solubility pump. *Global Biogeochemical Cycles*, *17*(1). https://doi.org/10.1029/2001GB001401

Umling, N. E., Thunell, R. C., & Bizimis, M. (2018). Deepwater Expansion and Enhanced Remineralization in the Eastern Equatorial Pacific During the Last Glacial Maximum. *Paleoceanography and Paleoclimatology*, *33*(6), 563–578. https://doi.org/10.1029/2017PA003221

Volk, T., & Hoffert, M. I. (1985). Ocean Carbon Pumps: Analysis of Relative Strengths and Efficiencies in Ocean-Driven Atmospheric CO2 Changes. In *The Carbon Cycle and Atmospheric CO2: Natural Variations Archean to Present* (pp. 99–110). American Geophysical Union (AGU). https://doi.org/10.1029/GM032p0099

Vollmer, T. D., Ito, T., & Lynch-Stieglitz, J. (2022). Proxy-Based Preformed Phosphate Estimates Point to Increased Biological Pump Efficiency as Primary Cause of Last Glacial Maximum CO_2 Drawdown. *Paleoceanography and Paleoclimatology*, *37*(11), e2021PA004339. https://doi.org/10.1029/2021PA004339

Wang, X. T., Sigman, D. M., Prokopenko, M. G., Adkins, J. F., Robinson, L. F., Hines, S. K., Chai, J., Studer, A. S., Martínez-García, A., Chen, T., & Haug, G. H. (2017). Deep-sea coral evidence for lower Southern Ocean surface nitrate concentrations during the last ice age. *Proceedings of the National Academy of Sciences*, *114*(13), 3352–3357. https://doi.org/10.1073/pnas.1615718114

Wanninkhof, R. (1992). Relationship between wind speed and gas exchange over the ocean. *Journal of Geophysical Research*, *97*(C5), 7373. https://doi.org/10.1029/92JC00188

Yu, J., Menviel, L., Jin, Z. D., Thornalley, D. J., Foster, G. L., Rohling, E. J., McCave, I. N., McManus, J. F., Dai, Y., & Ren, H. (2019). More efficient North Atlantic carbon pump during the Last Glacial Maximum. *Nature Communications*, *10*(1), 1–11.

Zhou, X., Duchamp-Alphonse, S., Kageyama, M., Bassinot, F., Doressoundiram, F., & Kissel, C. (2022). Variations of Primary Productivity in the Northwestern Arabian Sea During the Last 23,000 Years and Their Paleoclimatological Implications. *Paleoceanography and Paleoclimatology*, *37*(10), e2022PA004453. https://doi.org/10.1029/2022PA004453